ISSN 1000-9620

Marine Science Bulletin

海洋通报

Volume 8 • Number 2 2006

ISSN 1000-9620
02>
9 771000 962001

NATIONAL MARINE DATA AND
INFORMATION SERVICE OF CHINA

MARINE SCIENCE BULLETIN

Vol.8 No.2 Oct., 2006

CONTENTS

An Analysis of Observed Ocean Currents Data and Numerical Simulation in the Offshore Area of Jiaonan ····· LIU Weifeng (刘伟峰) et al. (1)

Characteristics of Semi-diurnal Internal Tides in the Western Equatorial Pacific Ocean Around 1°45′S, 156°E ····· BAO Xianwen (鲍献文) et al. (12)

A Fuzzy Probabilistic Influence Diagram Method to Assess Marine Configuration Risk ····· KANG Haigui (康海贵) et al. (21)

Physical and Mechanical Properties of Coral Sand in the Nansha Islands ····· YU Hongbing (于红兵) et al. (31)

Characteristics of Gas Hydrate Stability Zone and Resource Evaluation in Okinawa Trough ····· TANG Yong (唐 勇) et al. (40)

Mechanism of Nutrient Silicon and Water Temperature Influences on Phytoplankton Growth ····· YANG Dongfang (杨东方) et al. (49)

Forecast of Red Tide in the South China Sea by Using the Variation Trend of Hydrological and Meteorological Factors ····· ZHANG Junfeng (张俊峰) et al. (60)

Some Trials of Typical Typhoon Tracks Using the Adjoint Method ····· CAI Qifa (蔡其发) et al. (75)

The Catch Distribution of *Ommastrephes batramii* in Squid Jigging Fishery and the Relationship between Fishing Ground and SST in the North Pacific Ocean in 2004 ····· CHEN Xinjun (陈新军) et al. (83)

Metabolites of Marine-derived Mangrove Endophytic Fungus #2492 from the South China Sea ····· ZHU Feng (朱 峰) et al. (92)

LIBRARY
Pacific Islands Fisheries Scien
NOAA Fisheries
Honolulu, Hawaii

An Analysis of Observed Ocean Currents Data and Numerical Simulation in the Offshore Area of Jiaonan

LIU Weifeng (刘伟峰), SUN Yinglan (孙英兰), ZHANG Xueqing (张学庆)
School of Environmental Science and Engineering, Ocean University of China, Qingdao 266003, *China*

Abstract: Based on the diurnal consecutively observed data in the offshore area of Jiaonan in 2005, the paper tries to make a preliminary analysis of the specificity of ocean currents, tidal current property and residual current property in the area in observing dates. Then on the basis of observed data analysis and by employing the split-step method, the paper conducts a numerical simulation of the tidal current field, which can show the M_2 tidal constituent tidal wave system, current ellipse distribution, maximum current velocity distribution and time-dependent current field. The calculated results agree well with the observed data, which can on the one hand reflect the basic specificities of temporal and spatial distribution of the M_2 tidal constituent current field to some extent, and, on the other hand, offer more information about the hydrodynamic condition. So the paper would provide a scientific basis for the making of sea environment protection plans in the offshore area of Jiaonan under certain conditions.

Keywords: ocean currents; observed data; numerical calculation; Jiaonan

The coast of Jiaonan locates in an excellent geographic position, where lots of important aquaculture zones, tourism zones and military areas situate, which plays a significant role in the economical development of Jiaonan. In the near future, more and more marine projects are going to be built here, which will inevitably affect the hydrodynamic environment and ecological environment of the adjacent area. In order to explore and utilize its marine resources and space reasonably, and protect its marine environment scientifically, more information about the hydrodynamics and the physical self-purification capacity of the area need to be known. Based on the analysis of observed data and numerical calculation, the present paper analyzes preliminarily the hydrodynamic specificity in this area, in the hope of providing certain scientific basis for the making of sea environment protection plans in the offshore area of jiaonan.

1 Analysis of the observed field data

The area studied in this paper is from Fenghekou in the north to Langyatai in the south of the offshore area of Jiaonan (see Fig. 1). In order to know the hydrodynamic condition in this area, the

Received on May 26, 2006

Ocean University of China (OUC) set up three observing stations (S1-S3, see Fig. 1) in March 26th-27th, 2005, which is February 17th -18th according to the lunar calendar, a date of spring tides in this area, so it is a fine astronomical date. It is 4-5 scale north wind with a 2 grade sea state in the observing period. The OUC has also observed the currents for 25 hours with a sampling interval of 1 hour using the Intelligent Ocean Current Meter SLC9-1 designed by OUC. The Global Positioning System (GPS) is also used to locate position. The observation is conducted on the surface, in the middle and bottom layers. The surface layer is 1.0 m under the surface, while the bottom layer is 1.0 m above the bottom. Based on the observed field data, the paper attempts to analyze the specificity of ocean currents in this area.

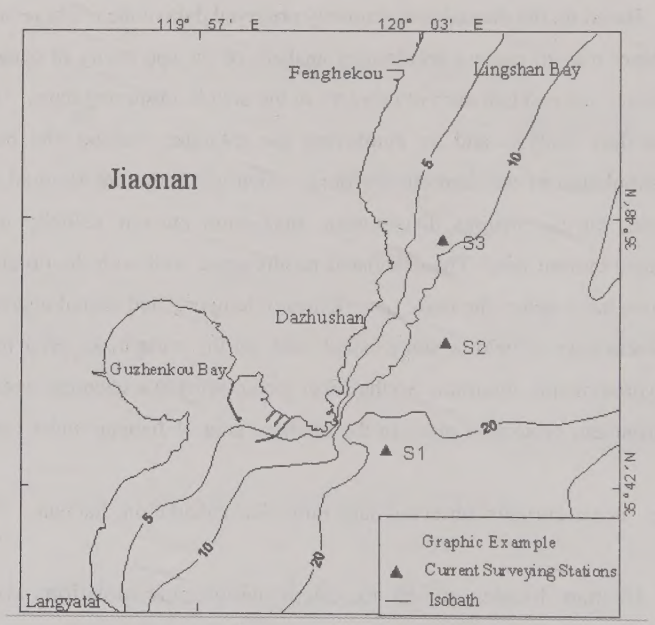

Fig.1 Topography of Jiaonan offshore area

1.1 Specificity of ocean currents

Fig.2 shows the change of observed time-dependent currents in three observing stations in the surface, middle and bottom layers respectively. In the period of currents observation, the ocean currents in the three surveying stations rotate in a counter-clockwise direction. The direction of the main currents in S1 and S2 is southwest-northeast, while S3 is south-north. The velocity of current in the three stations during flood or ebb is relatively fast. The velocity changes obviously in the vertical orientation, whereas the current direction has little change in different depths.

We can know from Tab. 1 that the velocity during flood is faster than that during ebb. The maximum velocity observed during flood is 92 cm/s, and the direction is 252°, which appears in the station S1. The maximum velocity observed during ebb is 84 cm/s, and the direction is 42°, which appears in the station S2. The velocity in the station S3 is the least, where the maximum velocity during

flood is 71 cm/s and the maximum velocity during ebb is 70 cm/s. Because of the topographic influence in the Dazhushan counterfort area, the velocity of S1 changes more sharply than that of the other two stations in the vertical orientation. The surface velocity of S1 during flood is faster than that of S2, while the middle and bottom velocity of S1 during flood is slower than that of S2.

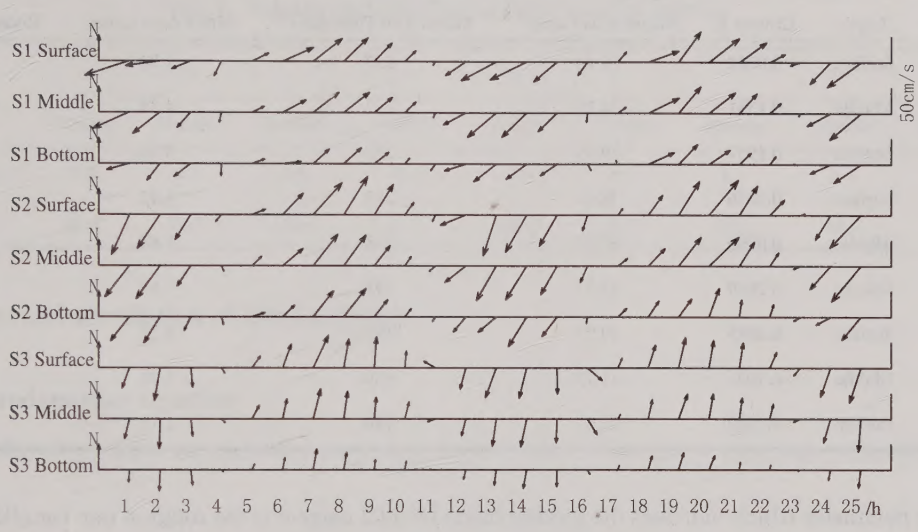

Fig. 2 Observed time-dependent currents

Tab.1 Observed maximum current velocity

Station	Mean Depth / m	Maximum	Surface		Middle		Bottom	
			Velocity / cm·s^{-1}	Direction / °	Velocity / cm·s^{-1}	Direction / °	Velocity / cm·s^{-1}	Direction / °
S1	24	Flood	92	252	78	246	56	232
		Ebb	76	52	68	36	54	40
S2	19	Flood	86	254	80	216	68	212
		Ebb	84	42	78	38	64	38
S3	12	Flood	71	198	64	184	41	182
		Ebb	70	25	60	14	35	17

1.2 Tidal current property

The general criterion of tidal property is the current ellipse macro-axis ratio K ($K = (W_{K_1} + W_{O_1})/W_{M_2}$, W_{k_1}, W_{o_1} and W_{M_2} is the ellipse macro-axis of K_1, O_1 and M_2 tidal constituent). The paper conducts a quasi-harmonic analysis of the observed data of currents by using the least squares technique [1], thus all of the elliptical parameters are calculated (see Tab.2).

The current ellipse macro-axis ratio in the three stations is between 0.078 - 0.265, which is less than

0.5, so the type of tidal current is the normal semi-diurnal tide. The motion mode of M_2 – the main semidiurnal tidal constituent represents the motion mode in the area.

Tab.2 Criterion for tidal current property and the elliptical parameters for M_2 tidal constituent

Station	Layer	Criteria K	Macro Axis / cm·s^{-1}	Macro Axis Direction / °	Minor Axis / cm·s^{-1}	Rotation Rate K'
S1	Surface	0.0782	59.43	237	1.82	0.031
	Middle	0.1381	54.18	232	4.39	0.081
	Bottom	0.1957	39.55	235	5.56	0.141
S2	Surface	0.2076	60.4	215	1.42	0.024
	Middle	0.0796	60.07	218	1.48	0.025
	Bottom	0.2649	43.57	216	5.57	0.128
S3	Surface	0.2085	49.07	193	8.23	0.168
	Middle	0.1927	41.73	189	3.91	0.094
	Bottom	0.2049	26.01	189	2.74	0.105

The parameter which indicates the motion mode of tidal current is the rotation rate (or ellipticity) K', whose value is the ratio of constituent current's ellipse minor axis and macro axis. They can be denoted by "+" and "-". "+" indicates the counter-clockwise rotation of constituent current, while "-" indicates the clockwise rotation.

The elliptical parameters of M_2 tidal constituent current in Tab.2 shows that the K' of M_2 tidal constituent current in S1, S2 and S3 is positive value, that is, the rotation direction of main constituent current is counter-clockwise. The K' of M_2 tidal constituent current is not large: S1 is 0.031 - 0.141, S2 is 0.024 - 0.128, and S3 is 0.094 - 0.168. Those values indicate that the rotation property of tidal current in the three stations is weak; and the tidal current is mainly the alternating current.

1.3 Residual current property

In the tidal bay or coastal waters, the circulatory current is formed by tidal current, wind-driven current, stream flow and the interaction among them. The non-periodical part, which is the net motion of sea water after a certain tidal period, is called the residual circulatory current (residual current) [2]. Most of the present ocean tide observation principles are based on the Euler Current Field in Fluid Dynamics, namely, getting the time-dependent observed sequence in a fixed spatial point and then conducting low-pass filtering according to the time-dependent sequence of the fixed spatial point, or getting the average value of one period, then the "Euler residual current" [2] is obtained. The velocity and direction of Euler residual current in the three stations are listed in Tab.3.

Tab.3 indicates that the residual current velocity in the three stations is between 2.3 - 8.0 cm/s. The velocity of surface residual current in S1 is the least, which is 2.3 cm/s; while the velocity in S2 is the most, which reaches 8.0 cm/s. The vertical change of residual current is rather obvious in S2 and S3, and the main situation is as follows: surface residual current > middle residual current > bottom residual

current. In the station S1, due to the topographic influence, the surface velocity of S1 is slower than that in the middle layer. To sum up, the direction of residual current is mainly to the east and turns towards the open ocean, which will benefit the transportation of contaminant in the offshore area.

Tab.3 Velocity and direction of Euler residual current

Layer	S1			S2			S3		
	Surface	Middle	Bottom	Surface	Middle	Bottom	Surface	Middle	Bottom
Velocity / cm·s^{-1}	2.3	4.7	2.5	8.0	5.6	2.8	6.1	5.1	3.1
Direction / °	68.4	98.9	134.0	90.4	114.8	80.7	57.1	69.5	79.0

2 Numerical simulation of tidal current

2.1 Hydrodynamics equation

The following tidal wave motion equations of depth mean in a barotropic ocean are adopted here:

$$\frac{\partial \zeta}{\partial t}+\frac{\partial (Hu)}{\partial x}+\frac{\partial (Hv)}{\partial y}=0 \tag{1}$$

$$\frac{\partial u}{\partial t}+u\frac{\partial u}{\partial x}+v\frac{\partial u}{\partial y}+g\frac{\partial \zeta}{\partial x}-fv+\frac{g}{C^2}\frac{\sqrt{u^2+v^2}}{H}u=0 \tag{2}$$

$$\frac{\partial v}{\partial t}+u\frac{\partial v}{\partial x}+v\frac{\partial v}{\partial y}+g\frac{\partial \zeta}{\partial y}+fu+\frac{g}{C^2}\frac{\sqrt{u^2+v^2}}{H}v=0 \tag{3}$$

where u, v correspond to the velocity component of x, y axis respectively, t is the time coordinate, g is the acceleration of gravity, f is the Coriolis parameter ($=2\Omega\sin\varphi$), Ω is the earth turning angle velocity, φ is the geographic latitude, ζ is the water level calculated from standing water surface, h is the water depth calculated form the standing water surface, $H=h+\zeta$, and C is the Chezy coefficient ($\mathrm{cm}^{1/2}/s$).

Fixed boundary: $$u\cos\alpha+v\cos\beta=0 \tag{4}$$

Open boundary: $$\zeta=\zeta' \tag{5}$$

When $$t=0,\ \vec{v}=\vec{v}_0,\ \zeta=\zeta_0 \tag{6}$$

The system of equations from (1) to (6) composes the complete closed finite solution system of equations of two dimensional tidal wave in the epeiric sea.

2.2 Numerical calculation of tidal currents

2.2.1 Numerical method

The calculated area is shown in Fig.1. The result is obtained by employing the split-step method based on irregular triangular grids, which can fit the coastline well. There are totally 2179 grid points with a minimum grid width of 50 m. The main characteristic of the split-step method is to calculate convection operator and diffusion operator in irregular grids by using the split-step technique which is appropriate to them, that is, adopting the characteristic line method in the former half step and the localized mass finite element method in the latter half step to solve equations, which can solve problems of calculated result distortion or pseudo-oscillation resulted from the numerical value dispersion when solving convective-diffusion equations with big Peclet numerals, or viscous flow not being stowed equation with big Reynolds numerals by using the finite difference and finite element method [3].

2.2.2 Water boundary inputting

Because it is hard to get the actual observed tide level on the open boundary of the studied sea area, the open boundary conditions adopt the result calculated by a model which is able to observe the tide level at the coast (from Lingshan Island in Qingdao to Shijiusuo in Rizhao) [4].

The following harmonic equation is adopted to input boundary:

$$\zeta(t) = H_{M2}\cos(\sigma_{M2}t - g_{M2}) \tag{7}$$

Where *u, v* correspond to the velocity component of *x, y* axis respectively, ζ is the water level, t is the time, H_{M2} is the harmonic constant amplitude of M_2 tidal constituent, σ_{M2} is the angular velocity of M_2 tidal constituent, and g_{M_2} is the harmonic constant epoch of M_2 tidal constituent.

2.3 Calculation results of tidal current and analysis

2.3.1 Verification

2.3.1.1 Tidal wave system

The cotidal lines and isoamplitude lines (see Fig.3) of M_2 tidal constituent indicate that the tidal waves in the area spread from northeast to southwest, which belongs to the counter-clockwise system. The cotidal line in Langyatai and Fenghekou differs by 10°, the time of climax delays for 21min. Due to the topographic influence, the amplitude of tidal wave increases gradually after the tidal wave enters this area from the open sea.

The above conclusion is consistent with the data in the Atlas of Bohai Sea, Yellow Sea and Donghai Sea [5] publicized in 1992.

2.3.1.2 Tidal current

By comparing the observed data in S1-S3 with the computed value in its corresponding point, as shown in Fig.4 the observed and computed tidal current roses, the main stream direction, rotation direction and the moment of max-flow in the three points are consistent with the observed values. The

maximum current velocity difference between the computed value in S1, S2 and S3 and the observed value is 4.7 cm/s, 6.1 cm/s and 4.9 cm/s respectively. The difference of main stream direction is 4.8 °, 6 ° and 10.8 °. The result indicates that the computed current agrees well with the observed data and the computed result is believable.

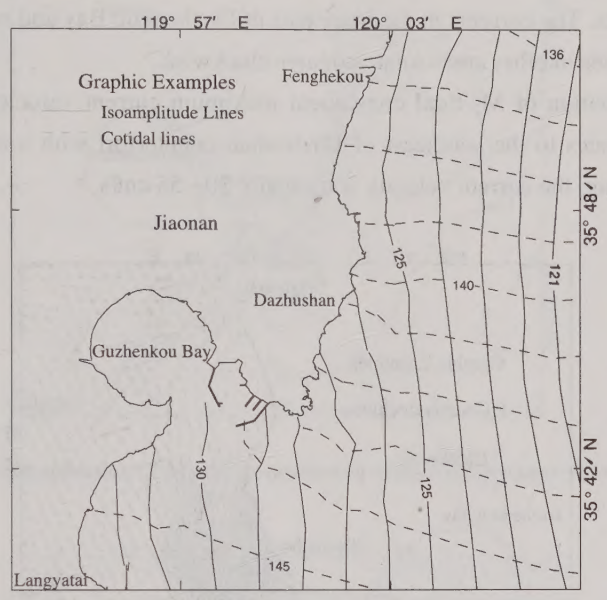

Fig.3 Cotidal lines and isoamplitude Lines of M_2 tidal constituent

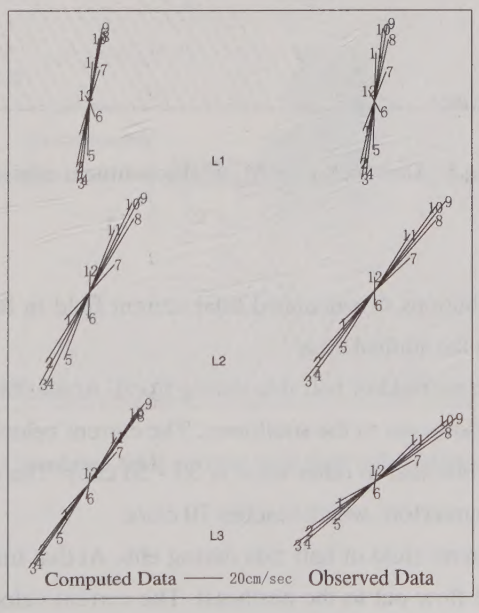

Fig.4 Observed and computed tidal current roses

2.3.2 Analysis of computed results

2.3.2.1 Tidal ellipse and distribution of maximum current velocity

Fig.5 is the distribution of M_2 tidal constituent ellipses, which shows that the currents in the sea area from Fenghekou to Langyatai are basically alternating currents except at a few points where the currents are weak rotary currents. The currents in the inner part of Guzhenkou Bay and near the bay mouth rotate clockwise, while the ones in other areas rotate counter-clockwise.

Fig.6 is the distribution of M_2 tidal constituent maximum current velocity, which shows that the strong current area locates to the southeast of Dazhushan counterfort with a maximum velocity of 70 cm/s. Generally speaking, the current velocity is normally 30 - 55 cm/s.

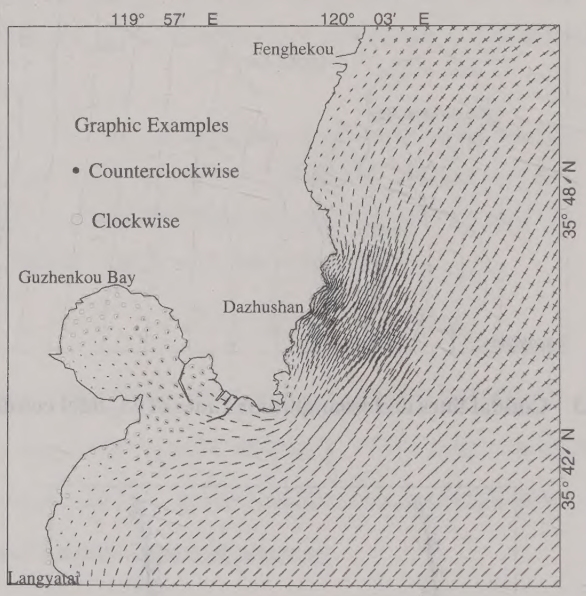

Fig.5 Distribution of M_2 tidal constituent ellipses

2.3.2.2 Current field

Fig.7 and Fig.8 are distributions of calculated tidal current field in half tide during flood and half tide during ebb respectively in the studied area.

Fig.7 is the calculated current field of half tide during flood. At that time the seawater flows in from the northeast of the area, and flows out to the southwest. The current velocity at the Guzhenkou Bay and near the bay mouth is slow, while that in other areas is 30 - 50 cm/s. The maximum velocity appears to the southeast of Dazhushan counterfort, which reaches 70 cm/s.

Fig.8 is the calculated current field of half tide during ebb. At that time the seawater flows in from the southwest of the area, and flow out to the northeast. The current velocity in the Guzhenkou Bay is the slowest, while that in the southeast of Dazhushan counterfort is the fastest, which reaches about 60 cm/s.

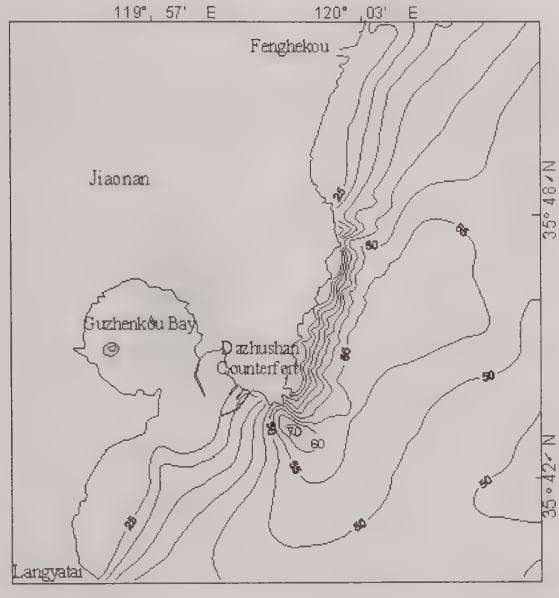

Fig.6 Distribution of M_2 tidal constituent maximum current velocity

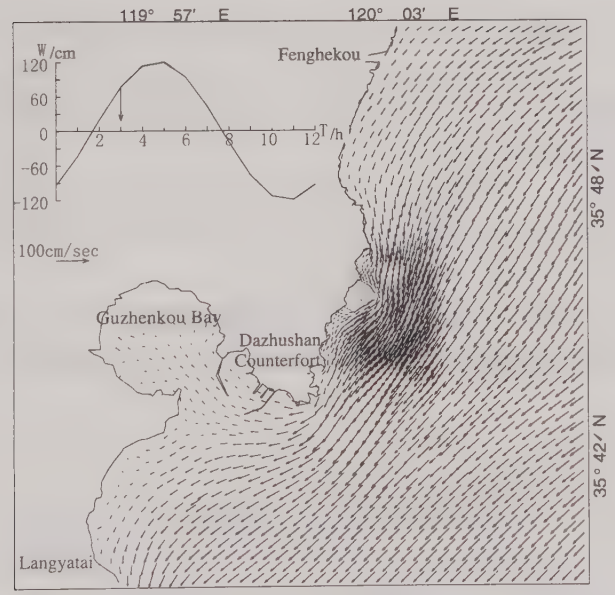

Fig.7 Calculated tidal current field (half tide during flood)

3 Conclusions

Based on the analysis of observed data and the numerical calculation of the tidal current field in the offshore area of Jiaonan, the paper makes a further study of the hydrodynamic condition in the area:

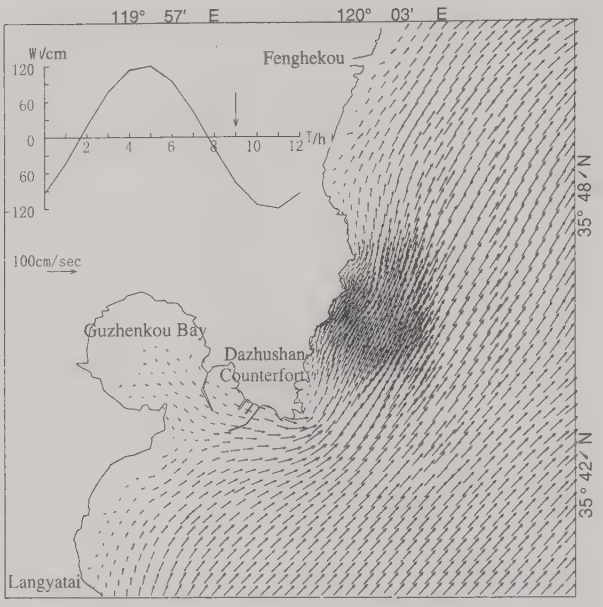

Fig.8 Calculated tidal current field (half tide during ebb)

a) The direction of main ocean current is southwest during flood and northeast during ebb. The current during flood is obviously larger than that during ebb. Because of the topographic influence, a strong current zone appears to the southeast of Dazhushan counterfort sea area. The maximum current velocity in the surface reaches 90 cm/s.

b) The tidal current is a normal semi-diurnal current and mainly the alternating current. The rotationdirection of tidal current is clockwise in the Guzhenkou Bay, while the tidal current in other areas rotates weakly in a counter-clockwise direction.

c) The velocity of residual current is large, and changes obviously in the vertical direction. The direction of residual current is mainly to the east and turn towards the open ocean.

References

[1] Ye Anle, Li Fengqi, et al. Physical Oceanography. Qingdao: Ocean University of Qingdao Press, 1991, 491-514.

[2] Sun Wenxin, Cheng Shijun, et al. Model of Environment Fluid Dynamics. Journal of Shandong Ocean College, 1988, 18 (2): 2-23.

[3] Wu Jianghang, Han Qingshu. Theory, Method and Application of Computational Fluid Dynamics. Beijing: Science Press, 1988, 216-250.

[4] Zhang Xueqing, Sun Yinglan, et al. Three Dimensional Current Field Numerical Simulation in Jiaonan Sea Area. Journal of Ocean University of China, 2005, 35(4): 579-582.

[5] Chen Guozhen, Niu Yinyi, et al. Atlas Maps of Bohai Sea, Yellow Sea and Donghai Sea. Beijing: Ocean

Press, 1992, 46-49.

胶南近岸海域海流实测资料分析及数值模拟计算

刘伟峰，孙英兰，张学庆

（中国海洋大学，环境科学与工程学院，青岛 266003）

摘　要：基于2005年胶南近岸海域海流的周日连续观测资料，对该海域观测日期内的海流特征、潮流性质及余流特点进行了初步分析；进而在实测资料分析的基础上，利用分步杂交法对潮流场进行了数值模拟计算，展现了 M_2 分潮的潮波系统、潮流椭圆分布、最大流速分布及逐时潮流场。数值计算结果与实测资料分析结果相一致，较好地反映出该海域 M_2 分潮潮流场时空分布的基本特征，对该海域的水动力状况有了更进一步了解，为胶南近岸海域的环境保护规划的制定提供了一定条件下的科学依据。

关键词：海流；实测资料；数值计算；胶南

Characteristics of Semi-diurnal Internal Tides in the Western Equatorial Pacific Ocean Around 1°45′S, 156°E

BAO Xianwen (鲍献文)[1], ZHANG Yijun (张义钧)[2], SUN Li (孙丽)[1,3], DU Tao (杜涛)[1], FANG Xinhua (方欣华)[1]

1. *Physical Oceanography Laboratory (a Key Laboratory under National Ministry for Education), Ocean University of China, Qingdao* 266003, *China*

2. *National Marine Data & Information Service, Tianjin* 300171, *China*

3. *Shanghai Flood Risk Information Center, Shanghai,* 200050, *China*

Abstract: The analyses of a data series obtained during TOGA- COARE show the existence of remarkable semi-diurnal internal tides in the western equatorial Pacific Ocean around 1°45′S, 156°E. Some characteristic parameters of the internal tides are vertical wavenumber -1.6×10^{-3} m^{-1}, horizontal wavenumber (wavelength) 3.3×10^{-2} km^{-1} (210 km), vertical propagation speed -3.8 cm/s and horizontal propagation speed 2.0 m/s. The waveforms propagate downwards slantingly, that is, the wave energy transfers upwards slantingly. Depth-distribution of the rotary spectral levels is a saddle-shape. The depths of the trough and the deeper peaks are almost coincident with those of the south boundaries of the South Equatorial Current and the Equatorial Undercurrent, respectively. The mean orientation of the rotary spectral ellipse changes with depth: 30° from north to east at 40 m, and changes into 14° from east to south at 324 m, and generally, it points to northeastward, which indicates that waves come from the southwest.

Keywords: internal waves; internal tides; western equatorial Pacific Ocean; TOGA-COARE

During the period of TOGA-COARE, an extensive international-joint-oceanic observation was carried out in the western equatorial Pacific Ocean and a large amount of valuable data was obtained. The main data used here are those collected from a single mooring instrument array at 1°45′S, 156°E, deployed by WHOI and the CTD data collected by the Chinese R.V. *Xiangyanghong 5.* The observation lasted more than 4 months (from 21st, Oct., 1992 to 4th, Mar., 1993 for the mooring), during which the temperature, salinity, current velocity and direction were recorded at certain fixed depths. The maximum depths for the temperature, salinity and current measurements are 260, 124 and 324 m, respectively; the water depth at the observation site is about 2 000 m. By using these observation data, Fang et al. (2000) [1] analyzed the dispersion relation of internal waves in this area, and the data set was described briefly in their paper.

Feng et al. (1998) [2] used these data with other data to analyze the characteristics of the semi-diurnal tides. Pinkel (2000) [3] analyzed internal solitary waves in this area according to the data obtained from the R.V. *John Vickers* during the same period in the same area. Though the resolution of the mooring data from WHOI is not high enough to discover internal solitary waves, some

Received on April 20, 2006

characteristics of the internal tides in that area can be identified from them.

1 Remarkable semi-diurnal tidal waves

The temperature-frequency spectra and rotary spectra of current velocities, estimated from the temperature time-series and velocity vector time-series at each observation depth, respectively, all show remarkable peaks at the semi-diurnal tidal frequency. For example, Fig. 1 shows the temperature spectra and rotary spectra at some depths. By using a special tide filter (Li et al. 1989; Cartwright and Tayler, 1971) [4, 5], waves of semi-diurnal frequency are selected and are shown in Fig. 2, which reveals more clearly the variation characteristic of semidiurnal tide frequency.

Because the observation-depth range is much smaller than the ocean depth, the barotropic waves and baroclinic waves of the same frequency cannot be separated only by using these data. However, the analysis to be presented later shows that the observed waves of semi-diurnal frequency are mainly internal tides.

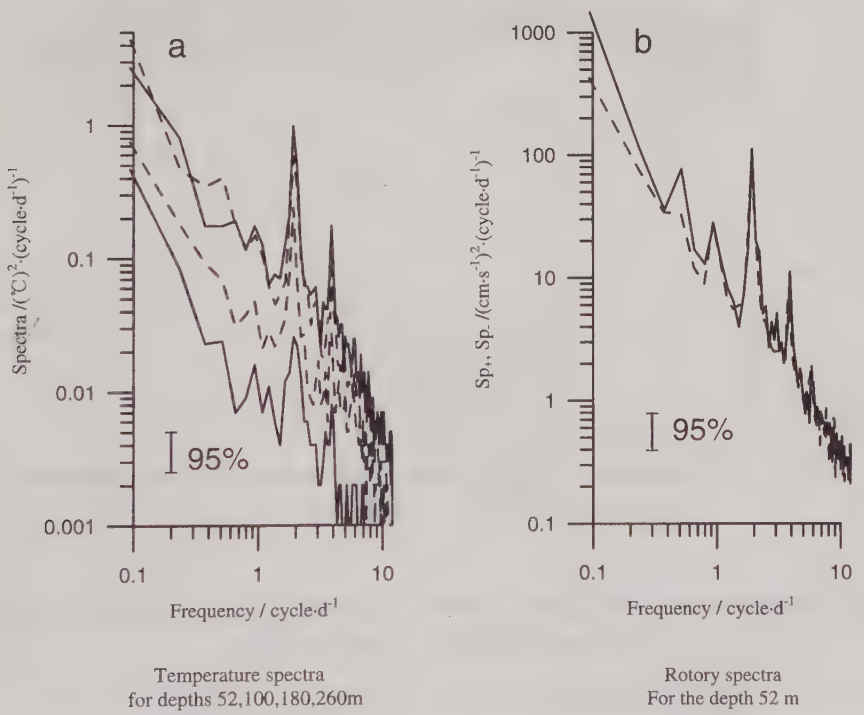

Fig. 1 Examples of frequency spectra of temperatures (a) and rotary spectra of current velocities (b)

2 No remarkable regularity in semi-monthly variations

Generally, tidal phenomena (barotropic tides) should have remarkable semi-monthly variations, but the data used here have no such regularity, which can be seen from the temperature time series shown in

Fig. 3. To reveal this characteristic more clearly, we use the normalized spectra of temperatures shown in Fig. 4.

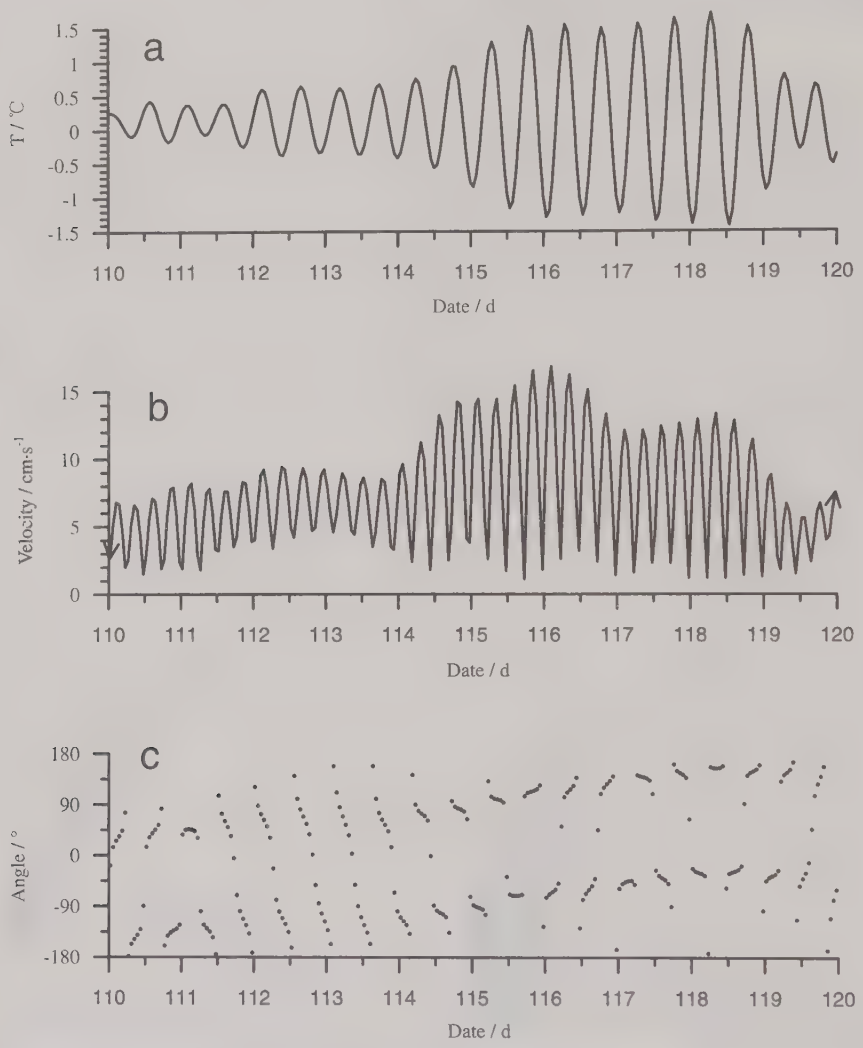

Fig. 2 Some segments of time series of filtered temperatures（a）, current speeds (b) and current directions (c) at the 84 m depth

The normalized spectra of temperature are obtained as follows: Firstly, calculate the raw estimate of the temperature spectra for each layer deeper than the mixed layer. Then, conduct light smoothing in the frequency domain to obtain smoothed spectra of lower degrees of freedom, since heavy smoothing may eliminate some important spectral peaks. Because the magnitudes of the temperature fluctuations at different depths are different, so are the spectral levels calculated, which are higher at shallower layers, and lower at deeper layers. Therefore, they cannot be regarded as the samples belonging to one ensemble, and cannot be ensemble-smoothed. To transform them into samples belonging to one ensemble, the area under each spectral curve should be converted into unity so that the spectral curves at

different depths have the same spectral level and these new spectra could be regarded as samples belonging to one ensemble, and can be ensemble-smoothed. The ensemble-smoothed spectral curve possesses a very high degree of freedom. This spectral curve is called the normalized spectral curve.

The curves in Fig. 4 show a lot of spectral peaks at low frequencies, with their corresponding periods marked. It is obvious that there is no spectral peak of semi-monthly period.

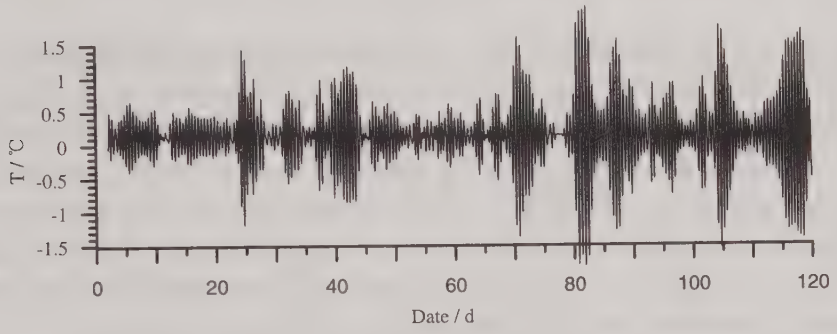

Fig. 3 The temperature time-series at the 84 m depth

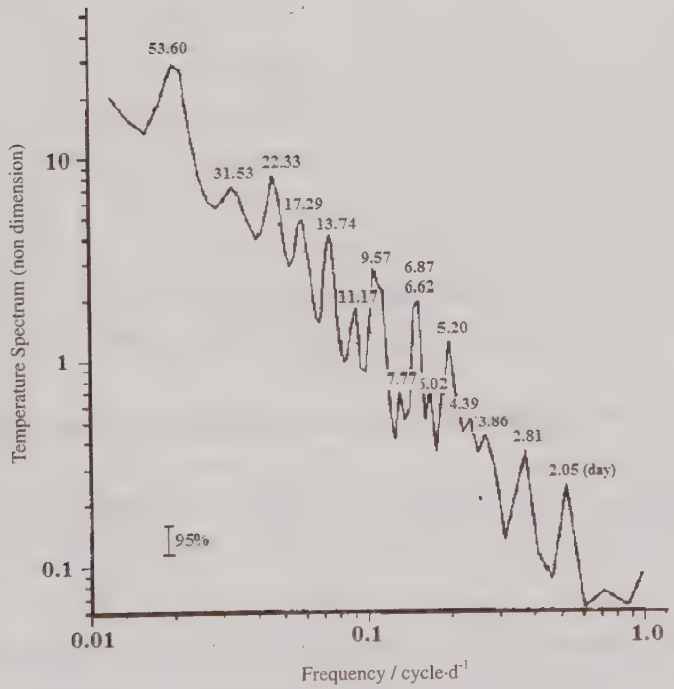

Fig. 4 The normalized temperatures spectra

The frequencies of surface tides shown by temperature series are not liable to be influenced by the background current field, but internal waves and internal tides are far less stable than surface waves. Therefore, they are extremely liable to the disturbance of the background current field and change their

characteristics. The semi-monthly period regularity is likely to be blurred by the variations of the average current field, which is generally called "current-contamination". Therefore, it could be deduced that internal tides might be the main component of waves of semi-diurnal frequency in this area.

3 Slanting propagation of the waves

Through the cross spectrum analysis of the temperature series at two adjacent depths, the phase lag of a wave between the two depths is obtained statistically. Add these phase lags one by one top-down, the depth-distribution of the lags is obtained and shown in Fig. 5. A positive (negative) phase lag indicates the wave phase propagating downwards (upwards). From the figure it could be seen that the phase lag is positive from 72 m to 88 m, and negative from 88 m to 104 m, and positive again from 104 m to 156 m, after which, positive and negative phase lags appear alternately, and the positive values are larger than the negative values. As a whole, in the depth range greater than 104 m, the phase increases with depth, which indicates that the wave-form propagates downwards statistically.

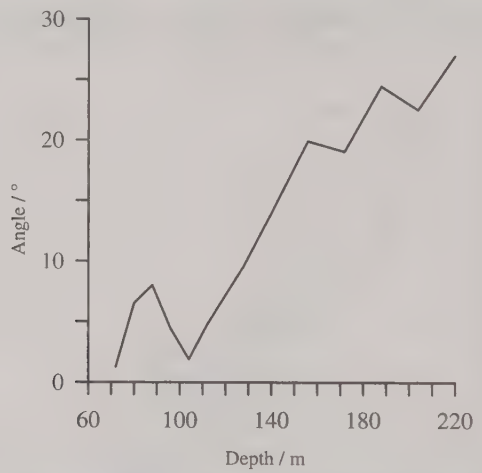

Fig. 5 The phase difference of the temperature cross spectrum at each depth

The time τ spent for a wave to propagate from one depth to another can be obtained from the phase difference (that is, lag) ϕ and the frequency ω (Fang and Wu, 2002) [6]

$$\tau = \phi / \omega$$

Because the phase difference at the depth range shallower than 104 m is not stable, only the data at depths greater than 104 m are used. From the depth 104 m to the depth 220 m, the phase difference $\phi = 25°$ and frequency $\omega = 2\pi/12.4\text{h}$, thus we have $\tau = 0.86\text{h}$. And then the vertical propagation velocity of waves $c_v = -3.75\text{cm/s}$ is obtained.

The results indicate that vertically the wave form propagates downwards and so that the wave energy transfers upwards. There is no vertical phase difference or vertical propagation for barotropic

waves. Waves that vertically propagate can only be baroclinic waves, thus it is further proved that the waves of semi-diurnal tidal frequency observed are mainly semi-diurnal internal tides.

Based upon the basic theory of internal waves, some further properties of the wave can be deduced. For the first mode, the relation between the vertical wavenumber k_v and water depth d is

$$k_v = \pi / d$$

Neglecting the influence of the mean currents, the relation between the horizontal wavenumber k_h and the vertical wavenumber k_v is

$$k_h = k_v \left(\frac{\omega^2 - f^2}{N^2 - \omega^2} \right)^{1/2} \approx \frac{\omega}{N} k_v$$

where N is the buoyancy frequency.

The relation between the horizontal propagation velocity c_h and the vertical propagation velocity c_v is

$$c_h = \frac{N}{\omega} c_v$$

Within the observation depth range in this area, the buoyancy frequency $N = 10^{-2}$ -5×10^{-3} S^{-1}(Fang et al., 2000; Pinkel, 2000) [1, 3] and the ocean depth d = 2 000 m. The calculated values of k_v, k_h, λ (horizontal wavelength), c_v and c_h are listed in Table 1. It can be deduced that the actual values of k_h, λ and c_h should be between the two calculated values. The average of the two should be a reasonable approximation. The propagation velocity of internal solitons obtained by Pinkel (2000) [3] is 2.4-2.8 m/s. The value of c_h of internal tidal waves (not solitons) mentioned here should be less than Pinkel's value, and it supports the rationality of the approximation from another point of view.

Tab. 1 The characteristics of semi-diurnal internal tides

N / s^{-1}	k_v / m^{-1}	k_h / km^{-1}	λ / km	C_v / $cm \cdot s^{-1}$	C_h / $m \cdot s^{-1}$
5×10^{-3}	-1.57×10^{-3}	4.42×10^{-2}	142	-3.75	1.33
10^{-2}	-1.57×10^{-3}	2.21×10^{-2}	284	-3.75	2.66
Approximate values	-1.6×10^{-3}	3.3×10^{-2}	210	-3.8	2.0

4 Polarity variation of current vectors

Generally speaking, in the middle and high latitude areas in the northern (southern) hemisphere, internal tidal currents possess rather obvious negative (positive) rotation characteristics. As the observation location in this paper is very close to the equator, where the geostrophic influence is very weak, the polarity of currents is not stable but changes alternately. This is shown clearly in Fig 2c, where

the velocity vectors rotate negatively during a period before the day 111, rotate positively from the day 111 to the day 116, negatively from the day 116 to the day 117.4, and then positively again after the day 117.4, and so on and so forth.

5 The depth-variation regularity of rotary spectra of current velocities

Within the observation depth range, the depth-profile of the rotary spectra of the semidiurnal tidal waves is saddle-shaped (Fig. 6). Two peaks appear in the upper depth range shallower than 100 m and at the depth 230 m respectively with a trough in between. The trough is just at the depths where the South Equatorial Current is. In the upper depth range, the positive rotary spectra are higher than the negative, while in the lower depth range, on the contrary, the negative rotary spectra are higher than the positive. The depth of the spectral peak in the lower depth range is almost the same as that of the south boundary of the Equatorial Undercurrent (Tomczak and Godfrey, 1994) [7]. It appears that the variation of the spectral levels may be related to the background currents.

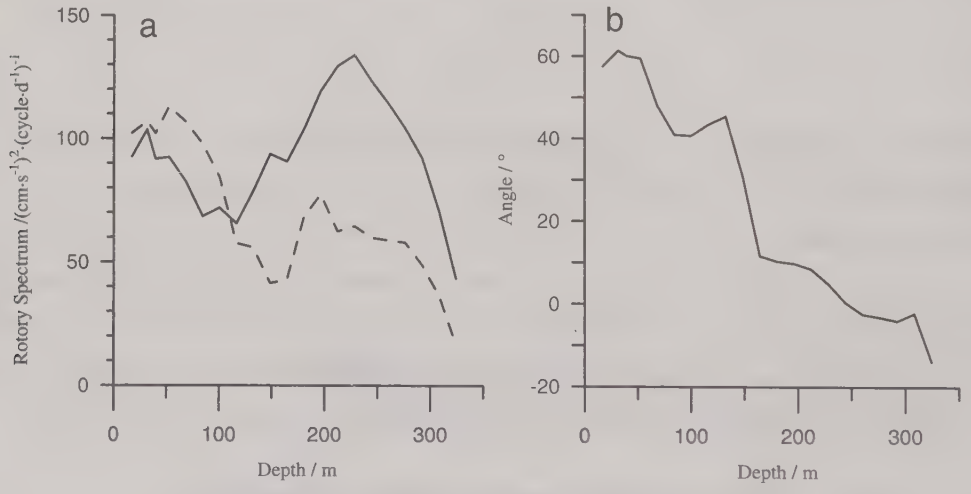

Fig. 6 Depth-variation of rotary spectra

Spectral level (a) and mean orientations of the main rotary axis ϕ (b) .

Generally, the vertical variation of the mean orientations of the main rotary axis ϕ shows remarkable regularity (Fig. 6b), that is, the axis rotates clockwise as the depth increases. ϕ is equal to about 30° from north to east at the depth 40 m and it is equal to 14° from east to south at the depth 324 m. The mean orientation of the main rotary axis ϕ is the same as the wave direction. The reason for such variation in the internal wave propagation direction is not clear yet. Maybe it is related to the mean background currents. The mean current directions (Fig.7) change from westwards (South Equatorial Currents) at shallower depths to eastwards (South Equatorial Undercurrents) at deeper depths (Tomczak and Godfrey, 1994) [7], and this variation may cause the wave propagation direction to change roughly from north to east.

As a whole, the main rotary ellipse orientation points to the northeast (about 30° from east to north), which indicates that waves of semidiurnal frequency come from southwest. To the southwest there is a

large area where the topography changes dramatically, and where islands such as New Ireland, New Britain, the Solomon islands, the Nuguria islands, etc. are located. The propagation directions of barotropic M_2 and S_2 tides are just southwest (Feng et al., 1998) [2]. The interaction between the barotropic tidal currents and the topography generates internal tides. When internal tides are generated in these archipelagos area, they propagate northeast to the observation site.

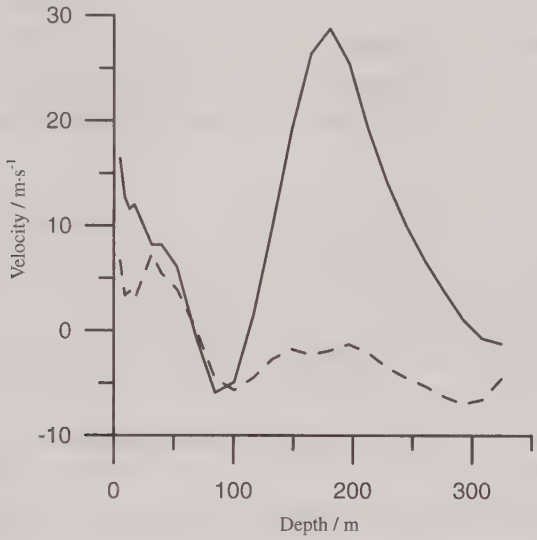

Fig. 7 Depth-variation of the mean currents

6 Conclusions

It is indicated by the above analysis that in the area around 1°45′S, 156°E, semidiurnal waves are mainly internal tides. They do not possess distinct semi-monthly periods. From the spectral analysis it is deduced that some characteristic values of the semidiurnal internal tides in this area are $k_h = 3.32 \times 10^{-2}$ km^{-1}, $k_V = 1.57 \times 10^{-1}$ m^{-1}, $\lambda = 210$ km, $C_h = 2.0$ m/s and $C_V = 3.8$ cm/s approximately. The waveforms propagate downwards slantingly, which implies that the wave energy transfers upwards slantingly.

Depth-distribution of the rotary spectral levels is saddle-shaped and the depths of the trough and the deeper peaks are almost coincident with those of the south boundaries of the South Equatorial Current and the Equatorial Undercurrent respectively.

The mean orientation of the rotary spectral ellipse changes with depth. It is 30° from north to east at a shallower depth (40 m), and changes into 14° from east to south at a deeper depth (324 m), and generally, it appears to point northeastward, which indicates that waves come from the southwest. When barotropic tidal currents pass through the archipelagic area with steep topography to the southwest, internal tides are generated and then propagate northeastward to the observation site (Fang and Du, 2005)[8].

Acknowledgments

The authors would like to thank Prof. HUANG Zuke of Ocean University of China for his great help during the research, and Weller R. and Andersen S. of WHOI for providing the mooring data.

This paper is supported by the National Natural Science Foundation of China (Projects under

contracts No. 49676275, 49976002, 40506007), Microwave Imaging National Key Laboratory Foundation (No. 51442020103JW1002).

References

[1] Fang xinhua, Jiang Mingshun, Du Tao. Dispersion relation of internal waves in the western equatorial Pacific Ocean. Acta Oceanologica Sinica, 2000, 19(4): 37-45.

[2] Feng M, *et al.* Semidiurnal tides observed in the western equatorial Pacific during the Tropical Ocean-global Atmosphere Coupled Ocean-Atmosphere Response Experiment. J. Geophys Res., 1998, 103(c5): 10 253-10 272.

[3] Pinkel R. Internal solitary waves in the warm pool of the western equatorial Pacific. J. Phys.Oceangr., 2000, 30(11): 2906-2926.

[4] Li Hongyan, Huang Zuke, Chen Zongyong. Study of response analysis and nonlinear input functions. Chin. J. Oceanol. Limnol. , 1989, 20(4), 330-337.

[5] Cartwright D E, Tayler R J. New computations of tide-generating potential, Geophys J. R. Astr. Soc, 1971, 23(1): 45-74.

[6] Fang Xinhua, Wu Wei. Analyses of Random Oceanographic Data. Qingdao Ovean University Press, 2002.

[7] Tomczak M, Godfrey J S. Regional Oceanography: An Introduction, Pergamon, London, 1994.

[8] Fang Xinhua, Du Tao. Fundamentals of Oceanic Internal Waves and Internal waves in the China Seas. Qingdao: China Ocean University Press, 2005.

赤道西太平洋 1°45′S，156°E 海区的半日内潮波特性

鲍献文[1]，张义钧[2]，孙丽[1,3]，杜涛[1]，方欣华[1]

（1. 中国海洋大学物理海洋实验室，山东 青岛 266003；2. 国家海洋信息中心，天津 300171；

3. 上海市防汛信息中心，上海 200050）

摘 要：通过对 TOGA-COARE 期间的一组锚系仪器阵列资料的分析得出：在赤道西太平洋 1° 45′ S，156° E。海域存在显著的半日潮频内波，它的水平波数（波长）、垂向波数、水平传播速度和垂向传播速度分别约为：3.3×10^{-2} km^{-1} (210 km)，-1.6×10^{-3} m^{-1}，2.0 m/s，-3.8 cm/s。波形向斜下方传播，亦即波能向斜上方传输。它在观测点西南方生成后，向东北方向传播，到达观测海区。流速矢量旋转谱水平随深度的变化呈马鞍形，低谷及深处的峰所在深度分别与南赤道流及赤道潜流的南边界所在深度大体一致。旋转椭圆主轴方位角随深度变化，在浅层（40 m 处）为北偏东 30°，到深处（324 m）转为东偏南 14°。总体上呈东北方向，表明波来自西南方向。

关键词：内波；内潮；赤道西太平洋；TOGA-COARE

A Fuzzy Probabilistic Influence Diagram Method to Assess Marine Configuration Risk

KANG Haigui (康海贵), YAN Lijun (阎利军), ZHOU Pengfei (周鹏飞)
State Key Lab. of Coastal & Offshore Engineering, Dalian University of Technology, Dalian 116024, Liaoning, China.

Abstract: A risk assessment method for marine configuration based on Fuzzy Probability Influence Diagram (FPID) and Failure Mode and Effect Analysis (FMEA) is established in this paper. Considering the fuzzy characteristic of the two key inputs such as event happening probability and relation probability, the method induces fuzzy probability into the PID risk assessment for marine configuration, where defuzzification is performed using the centroid method to determine the risk at a given grade of a probabilistic item. FMEA as a traditional qualitative analysis method is used to determine the effect factor structure. An application of the presented method for the offshore jacket platform is implemented. The method can be widely applicable although only offshore platform is analyzed here.

Keywords: Risk assessment; maritime configuration; fuzzy probabilistic influence diagram; failure mode and effect analysis.

Introduction

Nowadays, the concept of risk is used to assess and evaluate uncertainties associated with an event. Risk can be defined as the potential for loss as a result of a system failure. It's measured as a pair of the probability of occurrence of an event and the outcomes or consequences associated with the event's occurrence. A kernel element of risk is uncertainty represented by plural outcomes and their future likelihood [1]. The attention of the risk management in the offshore industry is focused on the safety of the crew and the installation, prevention of environment damage and production regularity. Unlike the onshore process industry, the potential for threatening the third party is quite limited for most offshore industry [2]. Risk assessment has been accepted in marine industry in relation to safety aspects - people's life and health as well as environment and property. It's required in order to document the risk level to be within specified acceptance criteria. To some extent, this is believed to have been an important reason for making risk assessments. It has also been put into active service as support for decisions, regarding design, construction as well as operation of marine installations.

Although risk assessments may be based on both qualitative and quantitative methods, the main focus here will be on quantitative assessments. Ref. [2] summarizes the implementation and use of the

Received on May 15, 2006

Quantitative Risk Assessments (QRA) in the offshore industry and reveals that QRA has been widely accepted in the area. In quantitative terms, it is the probability by which the predicted goals cannot be achieved with the available resources and refers to the joint probabilities of an occurrence of an event and its consequences [3]. Probabilistic Influence Diagram (PID) is one of the most important and effective methods among quantitative risk assessment methods, and it has been used in many risk projects including marine configuration.

When a complex risk system involves contributory factors with fuzzy sources and magnitudes, it often cannot be treated with probabilistic rigor during the initial phase of decision-making. For example in most offshore engineering problems, information about the probabilities of various risk terms is vaguely known in terms of linguistic variables like very high, high, very low, low etc. In the present research, the variables are represented with approximate values in the offshore structure risk assessment, which makes the validity and veracity of realistic risk assessment decrease evidently. The term computing with words has been introduced by Zadeh [4] to capture the notion of reasoning linguistically rather than with numerical quantities. This approach has proved very useful in the information technology [5] and in many other applications [6], where reported data are either qualitative or decision-making is performed based on this type of uncertainty (vagueness). In the marine industry, Blair [1] proposes a methodology for fuzzy-stochastic cost and makes risk-based decision analysis of alternative mobile offshore base hull construction concepts.

The objective of the paper is to propose a risk assessment for marine structure based on the fuzzy probability influence diagram. Considering the fuzzy characteristic of the two key inputs such as event happening probability and relation probability, the method induces fuzzy probability into the PID risk assessment for marine configuration, where defuzzification is performed using the centroid method [7] to determine the risk at a given grade of a probabilistic item. FMEA as a traditional qualitative analysis method is used to determine the effect factor structure. The developed methodology is applied to a case study of offshore jacket platform assessment.

1 Fuzzy probabilistic influence method

1.1 PID description

A probabilistic influence diagram is a compact representation of a Bayesian decision problem and consists of two parts. The first is the graphical part, or the "picture", and the second is the numerical part. Both the graphical and the numerical parts are required for a PID to be completed. At the graphical level, a probabilistic influence diagram can be represented by a directed acyclic graph of nodes and links (arcs). Each node in the diagram represents a proposition and each link represents a potential influence. These nodes and arcs tell us how to construct the probability distributions. The arcs signify the existence of direct influences on a proposition by its immediate predecessors. If an arc points to the node A from the node B, then the probability distribution of the node A is conditioned by the value of the node B. A conditional probability represents the strength of this influence. The direction of arc does not represent

indirect causality. The absence of an arc between two nodes does signify that they are conditionally independent. At the numerical level, for each node, we need to specify a set of probability values and a set of conditional probability distribution for it given the values of its predecessors. In this paper, $P(A)$ and $P(\bar{A})$ is a probability that represents the degree of belief in A and $\bar{A}$ (A's negation).

To demonstrate a probabilistic influence diagram graphical representation, consider the following example (Fig.1), where A is the parent of B and C, which are the parents of D. B and C are referred to as the children of A. C is also the parent of E. Proposition A is referred to as the source proposition, and the propositions D and E are referred to as the sink propositions. Predictive or causal inference involves reasoning from evidence about source propositions down through the diagram in the direction of links to sink propositions. It is assumed that all influence is captured in conditional probability relations between a child proposition and its parents. In other words, the child is conditionally independent of all other propositions in the network apart from its parents. If this is the case, then for proposition E,

$$P(E) = P(E \mid C)P(C) + P(E \mid \bar{C})P(\bar{C}) \tag{1}$$

The relationship between C and E is a feature of the structure of the inference problem. For example, C may be a necessary condition for E, in which the case $P(E \mid \bar{C}) = 0$ and $P(E \mid C) \leq 1$, or C may be a sufficient condition for E, in which case $P(E \mid C) = 1$ and $P(E \mid \bar{C}) \leq 1$. Probabilities can be propagated in either direction in the network, provided appropriate conditional probabilities are available.

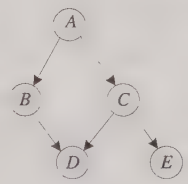

Fig. 1 Typical influence diagram

1.2 Fuzzy evaluation of probability in PID

Some event probability and relation probability that cannot be determined accurately would be reached by probabilistic items of experts, engineers, etc. The terms can be divided into various qualitative or linguistic classes. This qualitative classification system may induce imprecision and bias into the decision-making process, but provides useful insight into the process especially where quantitative information is limited or variables involve subjectivity. The qualitative classification describing the grade (or magnitude) of probability alone is not enough to explain the realistic probability, however, the method provides a reasonable expression by the possibly related information. Generally, triangular (TFN) or trapezoidal (ZFN) fuzzy numbers are used for representing linguistic variables [5], and each fuzzy probabilistic value is designated by TFN in the paper. The accurately probabilistic value could be viewed as a special instance of triangular fuzzy number and is presented as (a, a, a) where "a" is the realistic probabilistic value.

Table 1 describes this qualitative scaling system for grade and importance of risk items. Each qualitative scale N = 1, 2, …, 11 (for both grade and importance of risk) describing the vagueness and fuzziness in the linguistic connotation is expressed by TFNs. These definitions can be changed or modified based on expert panel recommendations or conducting surveys based on the Delphi method. The membership functions of triangular fuzzy numbers for the 11-level qualitative scales are as follows:

$$\mu_{N1}(x)=\begin{cases}1-10x, & 0\le x\le 0.1,\\ 0, & 0.1\le x\le 1,\end{cases}$$

$$\mu_{Nl}(x)=\begin{cases}0, & 0\le x\le \dfrac{l-2}{10},\\ 10x-(l-2), & \dfrac{l-2}{10}\le x\le \dfrac{l-1}{10},\\ l-10x, & \dfrac{l-1}{10}\le x\le \dfrac{l}{10},\\ 0, & 0.1\le x\le 1,\end{cases} \qquad (2)$$

$$\mu_{N11}(x)=\begin{cases}0, & 0\le x\le 0.9,\\ 10x-9, & 0.9\le x\le 1.\end{cases}$$

Consider two fuzzy probabilistic value N_A and $N_{B|A}$ representing probability and conditional probability of event A and B happening with membership values of η_{N_A} and $\eta_{N_{A|B}}$, respectively. The two factors can be multiplied to yield their joint probability:

$$N_{AB}=N_A \times N_{B|A} \qquad (3)$$

Tab. 1 Linguistic classification of grades of probabilistic value and their corresponding TFNs

Ranking level (l)	A qualitative explanation for grade of risk (r)	Triangular fuzzy numbers (TFN)
0	Absolutely low	(0.0, 0.0, 0.1)
1	Extremely low	(0.0, 0.1, 0.2)
2	Quit low	(0.1, 0.2, 0.3)
3	Low	(0.2, 0.3, 0.4)
4	Mildly low	(0.3, 0.4, 0.5)
5	Ok	(0.4, 0.5, 0.6)
6	Mildly high	(0.5, 0.6, 0.7)
7	High	(0.6, 0.7, 0.8)
8	Quit high	(0.7, 0.8, 0.9)
9	Extremely high	(0.8, 0.9, 1.0)
10	Absolutely high	(0.9, 1.0, 1.0)

The product of two TFNs is also a fuzzy number, but is not necessarily a triangle. To simply the calculating influence diagram procedure, the product is also viewed as a triangle fuzzy number, which

can be defined by $(a_1 \times a_2, c_1 \times c_2, b_1 \times b_2)$ where the two TFNs are denoted by (a_1, c_1, b_1) and (a_2, c_2, b_2) respectively. And the simplicity would result in little consequence because the centroid doesn't change.

1.3 Solution procedure

A PID is solved by "one-at-a-time" deleting nodes where the information constraints indicate the deleted consequence. The detecting process continues until only objective nodes remain, just whose probability distributions are concerned.

At times, an arc must be reversed before the detecting process continues. For example in Fig. 1, the node C would be the first node to be detected. Before C can be detected, however, the arc between C and D must be reversed using Bayes' Theorem. Bayes' Theorem is a mathematical formula defining the relationship between posterior and prior probabilities. After an arc has been reserved, both nodes involved inherit each other's direct predecessor nodes and still keep their own direct predecessor nodes (See Fig.2).

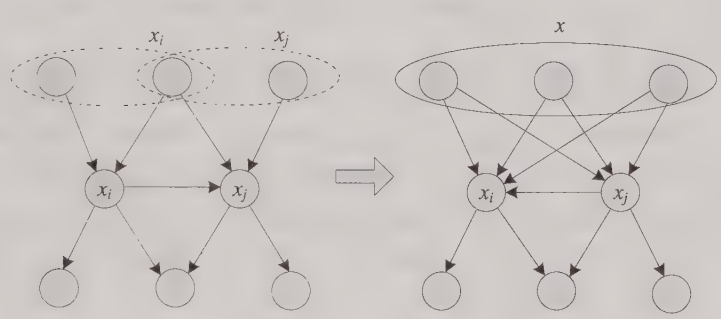

Fig. 2 An example of arc reversion

2 FPID based risk for maritime configuration

The risk assessment could be regarded as the study of the objective event probabilities with their causal events and relational probabilities.

2.1 Objective and scope of risk assessment

Marine configuration risk assessments have been put into active service as support for decisions, regarding design, construction as well as operation of marine installations. The objectives of a QRA may include: (1) Estimating risk levels and assessing their significance. This helps decide whether or not the risks need to be reduced. (2) Identifying the main contributors to the risk. This helps understanding of the nature of the hazards and suggests possible targets for risk reduction measures. (3) Defining design accident scenarios. These can be used as a design basis for fire protection and emergency evacuation equipment, or for emergency planning and training. (4) Comparing design options. Risk issues are taken into account in the selection of a concept design. (5) Evaluating risk reduction measures. QRA can be linked to a cost-benefit analysis, to help choose the most cost-effective ways of reducing the risk. (6) Demonstrating acceptability to regulators and the workforce. (7) Identifying safety-critical procedures

and equipment. These are critical for minimizing risks, and need close attention during operation. (8) Identifying accident precursors, which may be monitored during operation to provide warning of adverse trends in incidents.

There do not exist strictly defined mode and necessity content when assessing marine configuration. Therefore, to begin with, the assessment scope should be determined by its purpose and needful objective event would be identified ahead of risk assessment.

2.2 Construction of graphical part of FPID

The graph of FPID consists of event nodes and their links (arcs), which represent the problem framework relationship. Considering its complexity, the graph would be constructed in virtue of FMEA usually used in risk assessment. Observing the objective direction rule, the construction begins with objective event, analysis event causes and effects one by one, then represents each event mode in the FMEA table with a node in the influence diagram and connects immediately causal nodes by directed arcs, and selects nodes that cannot be estimated and implements continuously FMEA analysis until all of edge nodes can be estimated.

Take the loss risk assessment of an offshore platform for example. In the beginning, the events resulting possibly in the objective event (people loss) should be detected. There mainly are several failure modes (see Table 2) bringing about people loss on interviews and publication [8]. Since these failure modes (nodes) cannot be estimated immediately, they must be divided further. By FMEA, the nodes expand branch step by step. In the end, the graph of FPID becomes Fig. 3.

Tab. 2 Failure modes of people loss

Failure modes	Failure influence
Heat radiation from fire	Killing operators on the spot
Air pressure by blast	Injuring workers near the blast
Gas by blast	Harming people on the spot
Obstruction of survival passage	Withdrawing failure loss
Living room ruin	Endangering the people living and withdrawing there
Invalidation of survival equipment	Survival failure loss

2.3 Event description

In FPID, each event node could be viewed as a state set, which consists of different states that are independent of and exclusive from each other. Since they are all chance nodes, they must be described with probabilities of their states. But in practice, the lack of statistic data and the limitation of measuring means make it difficult to figure out accurately the probabilities of event states and those of their relationships between each other. Hereby, fuzzy probabilities are replaced with accurate probabilities in the FPID method, which would make good use of effective statistic data and expert subjective judgments to help make the rational risk assessment. Table 3 shows an example of node state

description.

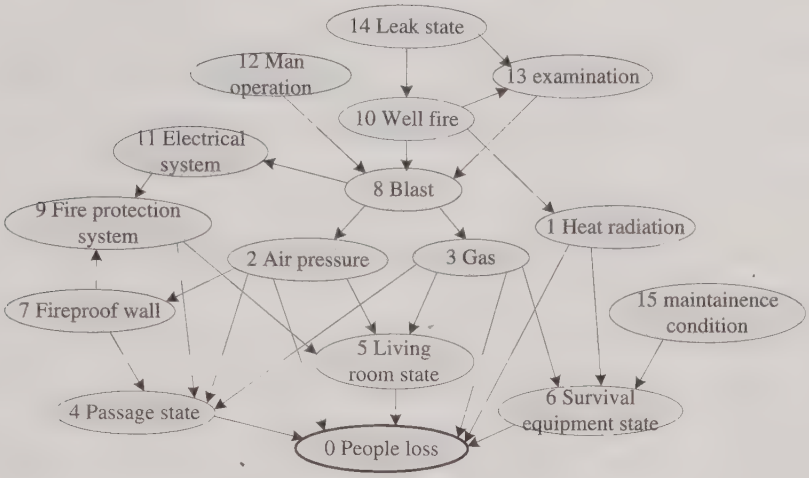

Fig. 3 The graph example of FPID of risk assessment for offshore platform

Tab. 3 Node state description

Node no.	Node name	State no.	State name	State fuzzy probability	Explanation
15	Maintenance condition	2	Good	Mildly high	Its creation is whether on
			Bad	Mildly low	schedule
14	Leak state	3	Large	Absolutely low	Its creation is velocity of leak
			Little	Extremely low	flow
			No	Extremely high	
13	Examination	2	Detected	Quit high	Both gas and fire are detected
			Not Det.	Quit low	
12	Man operation	2	Right	Quit high	Urgency operation
			Wrong	Quit low	

3 An application for offshore platform

People loss risk assessment plays an important role in the offshore industry. Hereby, to illustrate the proposed methodology, an example of people loss risk assessment for an offshore jacket platform is introduced, whose objective event is people injury and death. The objective event state space consists of "No people loss", "1-3 people loss", "4-8 people loss" and "more than 8 people loss". The structure graph of FPID could be developed by FMEA (See Fig. 3) and the fuzzy probabilities of nodes are decided based on either expert panel recommendations or by conducting a survey through telephone interviews or questionnaires. The results (probability grades) of several events selected for this case study are summarized in Table 3. After deciding the grade value for each probability item, the

probability is evaluated from Table 1. The procedure of FPID solution is as follows:

a) Combine node 12 and node 8.

b) Delete node 11, add an arc from node 8 to node 9 and evaluate the conditional probability between nodes 8 and 9, such as quite high probability between large leak event and well fire.

c) Reverse the link between nodes 10 and 13, evaluate the conditional probability between nodes 14 and 13, such as the mildly high probability between large leak and blast with right man operation.

d) Delete the node 13, add a link from the node 14 to the node 8.

e) Delete the node 10, add a link from nodes 14 to 1, evaluate the conditional probability between nodes 14 and 1, and the evaluate one between nodes 14 and 8.

f) Delete the node 1, add a link from nodes 14 to 6 and a link from nodes 14 to 0.

g) Delete the node 8, add three links from nodes 14 to 2, to 3 and to 9, and evaluate their conditional probability.

h) Delete the node 2, add three links from nodes 14 to 4, to 5 and to 7, and evaluate their conditional probability.

i) Delete the node 3, and update related conditional probabilities.

j) Reverse the link between nodes 7 and 9, update the conditional probability of nodes 14 and 7.

k) Delete nodes 9 and 7 and evaluate corresponding conditional probabilities.

l) Further, delete the nodes 4, 5 and 6 one by one. According to node 14 and 15 distribution probability, the conditional probability between 14 and 0, and one between 15 and 0, the distribution probability of node 0 could be reached.

For each conditional probability and joint probability, the membership $\eta_{L_i}(x)$ for linguistic variables (L0 to L10) can be estimated, e.g. in the case of the little leak state (Node 14), the 1-3 people loss (Node 0) conditional probability of node 14 is (0.02, 0.17, 0.32). The relevant memberships $\eta_{L_i}(x)$ of linguistic variables are L1=0.3; L2 = 0.7 and L3 to L10 =0.00 as shown in Fig.4. The maximal probability and the minimal with membership value 0.6 are 0.225 and 0.125, respectively. And in this case, the 1-3 people loss probability of the objective node is (0.01, 0.10, 0.28). Similarly, other event probability of the objective node can be solved.

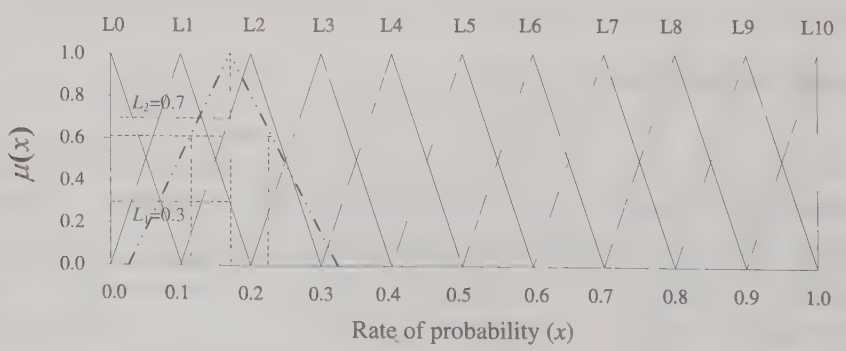

Fig.4 Membership functions of the set of criteria ratings of probability associated with risk assessment disposal

The joint probability of key events and the objective, which could be obtained from FPID, may reflect the key event influence on objective events. Table 4 gives the sort order on the key event influence importance in the case. The results show that the survival passage plays an important role in people loss. Therefore to improve the people safety condition, managers should firstly take mending the survival passage into account and insure it to be expedited. Secondly, they should pay attention to living room and survival equipments.

Tab. 4 The joint probability importance order

	1	2	3
No people loss	Survival passage	Living room	Survival equipment
1-3 people loss	Living room	Survival passage	Survival equipment
4-8 people loss	Survival passage	Living room	Survival equipment
More than 8 people loss	Survival passage	Living room	Survival equipment

4 Conclusion

The paper proposed a risk assessment method for marine configuration based on FPID and FMEA. A fuzzy logic inference system is used to capture both quantitative and subjective information in the form of numerical and linguistic data entry enabling use of approximate data. An application shows that the method is effective for the assessment, and can be widely applicable although only the offshore platform is analyzed here.

The risk assessment process combines the potential elects of cost, schedule, labor, safety, and environmental impact to produce utilities to guide decision makers. Other variations may be examined as required by the decision maker. For example, the decision-maker may require that the results of the decision model be analyzed for sensitivity to variation in choice of cost and schedule probability of occurrence and objective weighting.

References

[1] Blair A N, Ayyub B M, and Bender W J. Fuzzy stochastic risk-based decision analysis with the mobile offshore base as a case study. Marine Structures, 2001, 14: 69-88.

[2] Brandsæter A. Risk Assessment in the Offshore Industry. Safety Science, 2002, 40: 231-269.

[3] Sadiq R and Husain T. A fuzzy-based methodology for an aggregative environmental risk assessment: a case study of drilling waste. Environmental Modelling & Software, 2005, 20: 33-46.

[4] Zadeh L A. Fuzzy logic computing with words. IEEE Transactions - Fuzzy Systems, 1996, 4 (2): 103-111.

[5] Lee H M. Applying fuzzy set theory to evaluate the rate of aggregative risk in software development. Fuzzy Sets and Systems, 1996, 79: 323-336.

[6] Lawry J. A methodology for computing with words. International Journal of Approximate Reasoning, 2001, 28:

51-89.

[7] Yager R R. A general class of fuzzy connectives. Fuzzy Sets and Systems, 1980, 4: 235-242.

[8] Shachter R D. Evaluating influence diagrams. Operations Research, 1986, 34(6): 372-381.

基于模糊影响图的海洋结构风险分析方法研究

康海贵， 阎利军， 周鹏飞

（大连理工大学，海岸及近海工程国家重点实验室，辽宁 大连 116024）

摘 要：基于模糊影响图(FPID)和失效模式与效果分析(FMEA)建立了一种海洋结构风险分析方法。鉴于风险分析中某些事件发生概率和关系概率两个重要参数确定时需借助专家主观判断，本文将模糊概率的概念引入海洋结构影响图评估方法中。该方法成功地应用到海洋平台人员伤害分析中。虽然这里仅给出了该方法在海洋平台风险评估中的应用，但其具有更广泛应用价值。

关键词：风险评估； 海洋结构物； 模糊影响图； 失效模式和效果分析

Physical and Mechanical Properties of Coral Sand in the Nansha Islands

YU Hongbing (于红兵)[1], SUN Zongxun (孙宗勋)[1, 2], Tang Cheng (唐诚)[1]

1. *South China Sea Institute of Oceanology, Chinese Academy of Sciences, Guangzhou* 510301, *Guangdong, China*

2. *Guangzhou Geochemistry Institute, Chinese Academy of Sciences, Guangzhou* 510460, *Guangdong, China*

Abstract: Coral sand is a unique material developed in the tropical ocean environment, which is mainly composed of coral and other marine organism debris, with the $CaCO_3$ content up to 96 %. It has special physical and mechanical properties due to its composition, structure and sedimentary environment. In this contribution, we discuss its specific gravity, porosity ratio, compressibility, crushing, shearing and intensity for coral sand samples from the Nansha islands based on laboratory mechanical tests. Our results show distinct high porosity ratio, high friction angle and low intensity as compared with the quartz sand. We believe that grain crushing is the main factor that influences the deformation and strength of coral sand. Comprehensive study on the physical and mechanical properties of coral sands is significant in providing reliable scientific parameters to construction on coral islet, and thus avoids accidents in construction.

Keywords: Nansha Islands; coral sand; physical and mechanical properties

Nansha Islands, which include more than 200 islets, shoals and reefs, situate in the far-south of the South China Sea[1], starting from the Xiongnan islet (11°57′N, 117°E) in the north, and reaches the Zengmu shoal (3°57′44″- 3°59′N, 112 °16′25 - 112°17′10″E) in the south, and from the Haima islet (10°46″N, 117°47″E) in the east to the Wan'an islet (7°32′N, 109°30′E) in the west, with a total length of 1 195 km and width of ~ 973 km, covering an area of ~700 000 km^2. In recent years, coral reefs have been playing a more and more important role in the national defense construction and ocean resources exploiting [2]. According to the data presented by core Nanyong-1 and core Nanyong-2 drilling hole, the upper 0 - 17.3 m of coral reef consists of loose coral reef sediments with no cementation or weak cementation, below which is the catagenesis reef limestone. The coral sand covering coral reef tops is mainly composed of reef-building coral reef debris, with minor coral reef alga and bone debris of other marine organisms. It has developed into reef-flat facies or lagoon facies through onsite accumulation or short transportation driven by water and wind. The mineral contents are mostly aragonite and high magnesium the calcite with the calcium carbonate content up to 96 %. Coral sand is a unique rock and

Received on March 30, 2006

soil medium: loose, porous, and brittle, which is determined by its sedimentary environment and components [3]. It has totally different physical mechanical properties compared to the terrigenous quartz sand. Accidents often happen in construction on coral reefs due to the improper consideration of the physical mechanical properties of coral sand [4]. The study of coral sand physical and mechanical properties has great significance to ocean resources exploiting and national defense construction [5].

In order to get better knowledge of the coral sand physical and mechanical properties, mineral analysis, grain size analysis and porosity ratio and specific gravity measurement were done in the laboratory on the coral sand samples from the Nansha coral islets, and also soil mechanic tests like one-dimensional and three dimensional compression, direct shear and triaxial shear, grain crushing were made to get proper parameters for the coral islet engineering design.

1 Composition of coral reef sand

Coral reef sand is mainly composed of reef-building coral reef debris, and also includes other marine organism debris. Its mineral content is mainly aragonite and high magnesium calcite, and its chemical composition is $CaCO_3$. The grain size of coral reef varies, some reef block is above 5 mm, and some horn-shaped coral debris has high angularity, poor psephicity and high porosity. Grain size is related to the location landform unit, and becomes smaller gradually from outer reef flat to lagoon reflecting the effects of water force [6]. Coral sand of outer reef flat facies is mainly composed of grave, with fine sand and medium sand between the gravels. Coral sand of inner reef flat facies is mainly coarse sand, and also has fine sand and medium sand. Lagoon coral sand is mostly the medium-fine sand [7]. According to the grain size analysis of 36 samples collected from 25 different landform units of coral reefs, after taking out the big gravel, the composition mostly is gravel coarse sand, and a small part is coarse sand and the medium-coarse sand and medium sand are exceptional. In the grain size composition, gravel (> 2 mm) makes up of 30 % - 50 %, some reaches 50 % - 80 %, a few are lower than 10 %. Coarse sand (2 - 0.5 mm) content is 5 % - 15 %; medium sand (0.5 - 0.25 mm) 20 % - 40 %; fine sand (0.25 - 0.0063 mm) 5 % - 15 %; silt (0.063 - 0.004 mm); Clay (< 0.004 mm) makes up less than 5 %. Clay is hardly seen. The sorting coefficient of most samples is 0.6 - 1.4 [8].

2 Physical properties of coral reef sand

2.1 Specific gravity

There are 3 ways to get specific gravity: pycnometer, hydrometer and siphon tube. Pycnometer is used when the grain size is smaller than 5.0 mm; hydrometer is used for the grain size bigger than 5.0 mm, among which the grain size larger than 20 mm is less than 10 %, while the siphon tube method is used when the grain size larger than 20 mm is more than 10 %. Table 1 shows the coral sand specific gravity of Nansha islands. The dissolvable salt on the grain surface of the coral sand, which is partly or totally dissolved into the water, causes the specific gravity to be larger than that measured by kerosene.

The micro space between the coral sands is hard to be infilled by vacuumizing, so that the larger the grain size is, the smaller the specific gravity is.

Tab. 1 Coral sand specific gravity of Nansha islands

Method	Pycnometer		Hydrometer	Siphon tube
	Pure water	Coal oil		
Gravity	2.80	2.73	2.53~2.71	2.25~2.33

2.2 Porosity ratio

Porosity ratio as an important index to evaluate the engineering properties of coral sand refers to the ratio of the volume of pores to that of solid particles. As to the coral sand, the pore volume includes two parts: the volume between the particles and that inside the particles. Experimental results show that the inner-pore volume of coral reef makes up about 10 % of the total volume, which reflects the coral sand itself is loose and polyporous. It is obvious that the bigger the inner-porosity ratio, the greater the crushability under outside forces, thus presenting considerable compressibility and deformability.

It is difficult to get the original coral sand samples, and also there is no empirical formula to calculate the relationship between the onsite data and the porosity ratio. In the test of maximum and minimum porosity ratio, the punching will change the grain size especially for the uneven grain size coral sand. A proper weight was put on the sand surface instead of punching to get a minimum porosity ratio. The porosity ratio of coral sand ranges from 0.8 - 2.97, much higher than that of quartz sand [9]. Experiment shows that porosity ratio has close relation to the shape of grain, the reason is that the coral sand is formed by in-situ accumulation or short-distance transportation, it has low psephicity and high angularity.

3 Mechanical properties of coral sand

The basic mechanic properties tests of coral sand include compressibility test, direct shear test, triaxial shear test and grain crushability test. There are 3 main features of coral sand: high internal friction angle, high compressibility and high crushability.

3.1 Compression test

3.1.1 Single-axial compression test

The test was done on the high compress consolidation machine. The samples were carefully put into the sample chamber after measured by the electronic balance. A small stick was punching the machine to make it tighter, the vibration is dependent on the drying density. The original porosity ratio of the test sample can be calculated with the remaining sample quantity measured by electronic balance.

Compression device is installed after the sample is loaded, the centigrade meter is connected to the consolidation instrument and adjusted to zero. After the sample has been immerged into the water for 12

hours, get the value and then put loads of 12.5, 25, 50, 100, 200, 400, 800, 1600, 3200 and 4000 kPa, with unloading at 400, 800, 1600 and 3200 kPa according to the following procedure. The value of the centigrade meter is read before and after each loading. After this, read the value once an hour. The next load will be added when the difference between two readings is less than 0.01mm, which is considered as a stable situation. Normally each stable period lasts for ~ 24 hours, which increases as the load increases, e.g., 36 hours when the load is 4000 kPa. The maximum axial stress is 4000 kPa. In order to study the unloading restoration, the load test is done after unloading at different stress levels and the opposite way of loading is used.

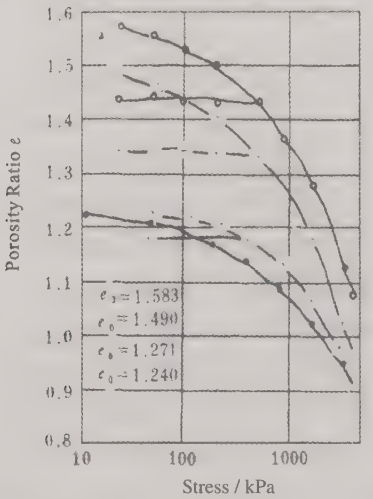

Fig.1 Single-axial compression curves at diverse initial porosity ratios

The initial porosity ratio of coral sand in the single-axial compression test is 1.583, 1.490, 1.271 and 1.240 respectively, which shows different characteristics from that of terrain sand. In case the axial stress is high enough, the coral sand with different porosity ratios will reach a similar status, while the unloading and loading curve will be a roughly superposition line, which shows a plastic deformation feature.

3.1.2 Triaxial compression test

The test was carried out on a high pressure triaxial instrument, the sample is 3.80 cm in diameter, 7.6 cm in height, and 14 Mpa in the maximum confining pressure. The load is separated into 50, 100, 200, 400, 800, 1600, 3200, 4000 kPa, unloading and loading test was done at 400, 800, 1600 and 3200 kPa. It is regarded as stable when the difference between two continuous values of deformation tube and the previous level value is less than 0.01 mL.

Fig.2 shows the triaxial compression curves of coral sand. The initial porosity ratio is 1.482, 1.316, 1.170 and 1.032, which shows a linear rise in the latter period while the compression index goes up quickly at the beginning.

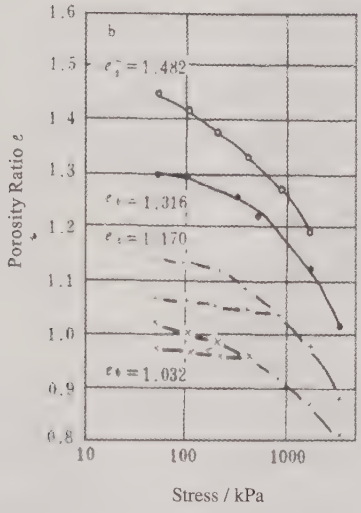

Fig.2 Triaxial compression curves at diverse initial porosity ratio

The trend of the triaxial compression curve shows similar features to the single axial curve, both of which include a starting gentle arc followed by a nearly linear segment. In the arc segment, the curvature increases with loading. In the linear segment, the slope is affected by the original porosity. Slope increases as the initial porosity increases, indicating that high initial porosity increases its compression. The linear segment of single axial curve starts at the pressure of 800 kPa while in the triaxial curve the linear segment does not show clearly until 1600 kPa.

Single-axial and triaxial loading and unloading curves are all coincident flat lines, which indicates that the compressing process of coral sand is mainly an unrecoverable plastic deformation process. The volume compression is mainly caused by grain crushing and the fine particles infilling the space between grains. The crushing of big particles also causes volume compressions. The deformation would not be recovered even after draining immediately with unloading.

3.2 Direct shear test

The direct shearing test is used for getting the strength parameters, c and Φ. Consolidated quick shear is used in such a test.

Samples are measured by using an electronic balance and put into the direct shear test container with dank stone and filter paper, the container is knocked slightly using a small wood stick until the sand fills the shear container, and then put under a designed stress for 12 hours. Vertical stresses in the test are 100, 200, 300 and 400 kPa. The shear proceeding was pushed by a hand wheel at a rate of 6 cycles per minute after consolidation. When the value reaches a peak or the strain is over 15 %, the shear is stopped. The relative densities of the samples A and B are 46 % and 95 % respectively.

The result shows that the medium-coarse sand has a high internal friction angle between 37°- 45°, the cohesion strength basically is 0, similar to the normal sand. The fact is the high internal friction angle doesn't mean high load, this strange relationship between high friction angle and load cannot be

explained by the present soil mechanics theory.

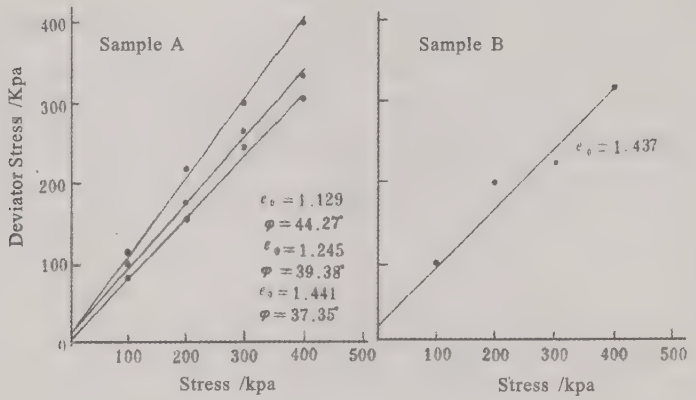

Fig.3 Curves of direct shear test of coral sands

3.3 Triaxial shear test

The focus of the research on the mechanic properties of coral sand under the triaxial shear test is the stress-strain curve. In order to study mechanic properties under normal pressure and high confined pressure, a triaxial shear test under an effective confining pressure of 100 kPa - 2500 kPa is designed. The key step is preparing samples from the loose, crushable coral sand. This new technique can make more than 95 % saturation samples within 5 h. The relative densities of samples A and B are 46 % and 95 % respectively.

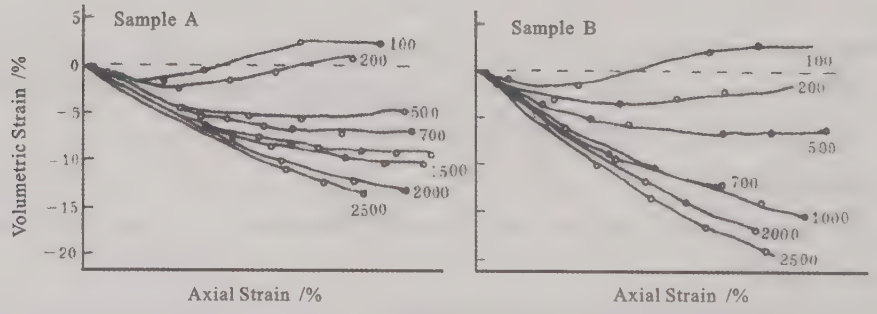

Fig.4 Curves of axial strain and volumetric strain under drained conditions

The feature of drained shearing of coral sand is related with effective confining pressure and strain hardening. Its peak value appears when the effective confining pressure is less than 1000 kPa, while it is not obvious or does not exist when the effective confining pressure is more than 1000 kPa, and rises with the increase of the effective confining pressure.

Under low confining pressure (δ < 100 kPa), the coral sand shows clear shear-dilation

characteristics, and when δ >100 kPa, it shows immediately the feature of shear-shrink. Deviator stress increases with the increasing confining pressure, and its peak value appears at a high strain stand. Stress-strain relationship of coral sand is similar to that of compact terrigenous sand, both the axial strain and the volume strain increase in the process of destroying with the increase of confining pressure. The drained shearing experiment shows a strain-harden phenomenon from shear-dilation to shear-compression.

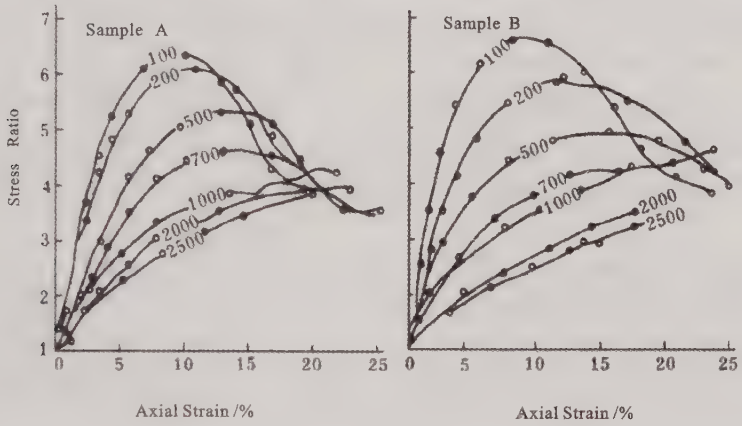

Fig.5 Curves of axial strain and effectives stress ratio

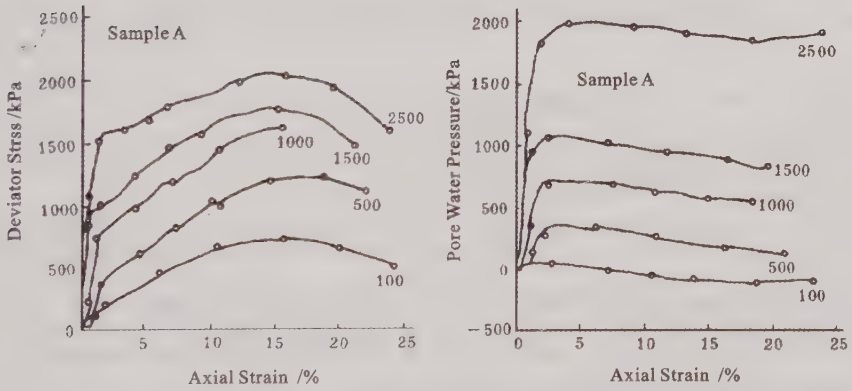

Fig.6 Relations of deviator stress and pore water pressure to axial strain under undrained conditions

Undrained shear stress-strain curve of coral sand is quite different from that of drained shearing, and can be divided into three segments: steep stress increasing segment; gentle stress increasing phase and gentle stress decreasing segment. With the increasing confining pressure, the peak value appears at the high strain force only. Pore water pressure reaches its peak rapidly but drops slowly, and at low pressure (0.1 Mpa) the negative pore water pressure appears. The variation of the pore water pressure

will transfer from positive value to negative value with the increasing axial stress under a low confining pressure, and continuously to be positive and high value when the confining pressure reaches a certain level. Such high pore water pressure will clearly decrease the mean effective stress [10].

3.4 Grain crushability test

Crushing under external forces is an important characteristic of coral sand, as shown in the process of compressing and shearing. Pressure higher than 100 kPa will produce measurable crushing, and the crushing is accelerated with the increase of confining pressure. It varies slowly when the confining pressure is less than 800 kPa and intensely when the confining pressure is more than 800 kPa. In the case of the quartz sand, usually there is no grain crushing, only slight crushing occurs when the confining pressure is more than 1600 kPa. The crushability is also affected by the shear way. It is more serious under drained shear than that with no drained shear, and also more serious under the co-action of confining pressure and shear than in a single way, and more intensive with the larger grain size and worse graduation.

The crushing degree increases with the increasing confining pressure, grain degree of angel, grain diameter, pore volume and slake debris. Grain crushing is a key factor affecting the engineering properties of coral sand. The development of grain crushing will change the stress-strain relationship from brittle to plastic, from shear-swelling to shear-contraction, and reduce the ratio of the maximum effective stress [11].

4 Conclusions

As a special marine soil medium, coral sand shows different mechanic properties compared to quartz sand:

a) The carbonate content of coral sand is up to 96 %, its specific gravity is 2.73 - 2.80 and varies with different measuring media, the larger the grain size, the smaller the specific gravity. It has a high porosity ratio, 0.8 - 2.97, which is larger than that of quartz sand.

b) The mechanic properties of coral sand are high internal friction angle, high compressibility and strong crushability.

c) Coral sand has a large internal friction angle, but a low bearing capacity

d) The high compressibility of coral sand is determined by the high porosity ratio, and the compression process is an unrecoverable plastic deformation.

e) Coral sand is crushable in the process of compressing and shearing, which is the key factor affecting the deformation and intensity of coral sand. The crushability of coral sand is related to the confining pressure.

References

[1] Chen S J. The General View of Nansha Islands. Marine science Bulletin. 1986, 1(1):52-58.

[2] Sun Z X, Zhao H T. A New disciline –Engineering Geology of Coral Reef. Hydrogeology and Engineering Geology. 1998, 25(1): 1-4.

[3] The Multidisciplinary Oceangraphic Expedition Teem of Chinese Academy of Sciences to Nansha Islands. Quaternary Coral Reef Geology of Yongshu Reef, Nansha Islands. Beijing: Ocean Press.1992, 1-264.

[4] Sun Z X, Huang D C, Zhan W H et al. Division and Qualitative Evalution of Engineering Geo-environment on Nansha Islands. Journal of Engineering Geology. 2003, 11(1): 36-43.

[5] Sun Z X, Zhan W H, Zhu J J. Rockmass Stability of Yongshu Reef, Nansha Islands. Marine Geology and Quaternart Geology. 2003, 23(4): 9-14.

[6] Yu H B, Sun Z X, Mao Q W. Geomorpic Features of Upper Seaward Slope of Yongshu Reef, Nansha Islands. Marine Science Bulletin. 1999, 18(3): 49-54.

[7] Sun Z X, Zhan W H, Zhu J J. Rockmass Structure and Engineering Geological Zones of Coral Reefs, Nansha Islands of South China Sea. Journal of Tropical Oceanography. 2004, 23(30): 11-20.

[8] Song C J, Zhao H T, Chen X S et al. The Site Selection of Channel, Anchorage and Harbor of Nansha Islands.Beijing: Science Press. 1996, 1-132.

[9] Wang R, Song C J, Zhao H T et al. Engineering Geology of Coral Reef of Nansha Islands. Beijing: Science Press. 1997, 1-169.

[10] Liu Chongquan, Wang Reng. Physical and mechanical properties of calcareous Sand. Rock and Soil Mechanics, 1998, 19(1): 32-37.

[11] Datta M, Gulhati S K, Rao G V. Crushing of calcareous sands during shear. In: Proc. Offshore Tech.confer.Houston. 1979, 1 456-1 467.

南沙群岛珊瑚砂物理力学性质研究

于红兵[1]，孙宗勋[1,2]，唐诚[1]

（1. 中国科学院南海海洋研究所，广东 广州 510301；2. 中国科学院广州地球化学研究所，广东 广州 510640）

摘 要：珊瑚砂是发育于热带海洋环境中特殊的岩土介质类型，主要由珊瑚碎屑和其它海洋生物碎屑组成，碳酸钙含量高达96%。特殊的发育环境、物质组成和结构导致了珊瑚砂具有独特的物理力学性质。本文对采自南沙群岛珊瑚岛礁的珊瑚砂样品进行了一系列室内土力学试验，根据试验结果讨论了珊瑚砂的比重、孔隙比、压缩性、破碎性、剪切特性等，指出了珊瑚砂具有不同于石英砂的比重和孔隙比等物理特性，力学性质的特殊性表现在三个方面：内摩擦角大，高压缩性和易破碎。作者认为颗粒破碎是影响珊瑚砂变形和强度特性的主要因素。全面深入地研究珊瑚砂的基本物理力学性质，可为珊瑚岛礁工程建设提供科学合理的设计参数，避免工程事故的发生。

关键词：南沙群岛；珊瑚砂；物理力学性质

Characteristics of Gas Hydrate Stability Zone and Resource Evaluation in Okinawa Trough

TANG Yong (唐 勇)[1,2], JIN Xianglong (金翔龙)[2], FANG Yinxia (方银霞)[2]

1. *China University of Geosciences, Wuhan* 430074, *China*

2. *Key Laboratory of Submarine Geosciences of State Oceanic Administration, Second Institute of Oceanography, SOA, Hangzhou* 310012, *China*

Abstract: According to the processing and interpretation of multichannel seismic reflection data in the area of Okinawa Trough, the BSR (bottom simulating reflector) was identified in 16 seismic profiles. By means of special processing technologies such as AVO and waveform inversion, the authors, for the first time, directly used the BSR to outline the distribution tendency of thickness of gas hydrate stability zone in the Trough and thought that the largest stability zone thickness was in the south and the smallest in the north. Then through calculation the authors got the thickness of hydrate stability zone and resource of the hydrate. This would be useful to the future hydrate exploration and resource evaluation in the Okinawa Trough.

Keywords : BSR; gas hydrate; hydrate stability zone

The formation of gas hydrate which is composed of mainly methane generally needs low temperature and high pressure. In the 90 % of the world ocean, the temperature-pressure field of gas hydrate stability zone exists below some depth. If sediment has the sufficient intergranular pore space (in order to form cage shape), as well as sufficient water and methane, when the shallow gas causing biologic formation and the deep gas causing heat formation in the sediment come into the temperature-pressure field in the upward migration process. Sediment has filled the sediment's pore space, forming the gas hydrate. The sediment layer which can ensure the forming and stability of the gas hydrate is called the hydrate stability zone (HSZ). The thickness of hydrate stability zone is mainly controlled by water depth, the geothermal gradient, the seabed temperature and the hydrate phase equilibrium curve. If the geothermal gradient is smaller and the seabed temperature is lower and the water depth is deeper, the thickness of gas hydrate stability zone (HSZ) is larger. The gas hydrate as far as possible fills the sediment's pore space in the hydrate stability zone, thus forming a cap rock and catching the massive free gas below it. The base of gas hydrate stability zone represents the steady phase boundary of the free gas - gas hydrate and the free gas - water. HSZ is mainly controlled by the pressure and the temperature, also possibly by the influence of the geochemistry condition. The base of gas hydrate indicates the bottom-simulating reflector (BSR [1-2]) in the seismic profile.

The natural gas hydrate can effectively cement detritus granules, and reduce the sediment porosity.

Received on April 29, 2006

So its existence changes the sediment's geophysical properties, making the hydrate sediment zone (HDZ) display a higher resistivity in geophysics and big seismic propagation velocity and small sound wave time difference and low natural electric potential. The base of gas hydrate in the seismic profile can produce the acoustic impedance contrast interface. As the interface parallels the seafloor and its phase is opposite to the latter, therefore it is called the bottom-simulating reflector (BSR[3]). The depth of BSR is consistent with the theoretical base of the gas hydrate pressure - temperature stability zone, consequently BSR is one of significant symbols for distinguishing the gas hydrate .It suggests the existence of the gas hydrate stability zone. Now, it is difficult how to confirm the upper boundary of the gas hydrate.

Many kinds of methods are synthetically utilized for the seismic characteristics such as the wave inversion, AVO inversion, reservoir forecasting technology (such as nerve network forecast stratum parameter, amplitude fitting forecast reservoir thickness), direct-viewing recognition of the blank zone, the fine velocity analysis and so on , but the wave inversion is the key technology [4-13] .

1 Characteristics of gas hydrate stability zone

There are mang factors influencing the formation and the stable distribution of seabed gas hydrate. The controlling factors are mainly the gas origin, the sediment's temperature and pressure and the rock granularity and so on. But the natural gas origin, the rock granularity and the temperature mainly are controlled by the filling characteristic and the heat system of the sediment basin. Pressure and seabed temperature are decided by the water depth. The terrain characteristic in the Okinawa trough is that it is deep in the south and shallow in the north, the water depth is more than 800 - 2 000 m, the trough topography is obvious, the fault structure is developed, it is a famous modern active structure. Trough in the west slope deposits thicker pliocene and pleistocene sediment, its thickness reaches 4 000 - 8 000 m and the thickest place surpasses 10 000 m [14]. Higher organic content (C: 0.75 % - 1.25 %) and quick sediment rate (10 - 40 cm/ka) [15] are advantageous to the organic preservation and the hydrocarbon's transformation. The high seabed heat flow characteristic (Li Naisheng et al.), the good oil gas condition and the fact that the carbon dioxide hydrate in the Mid-Okinawa Trough has been discovered, have provided an advantageous mineralization environment for gas hydrate formation, also explained why Okinawa Trough basin has the attractive prospect of hydrate resources. Because hydrate distribution is greatly influenced by the geothermal gradient and the geothermal gradient in the Okinawa Trough distributes nonuniformly in the plane, the value of geothermal gradient changes greatly, also the high value and the low value distribute closely, the distribution of geothermal gradients in the Okinawa Trough shows that it is lower in the south, highest in the middle and comes second in the north [2, 14].

We have collected 45 multichannel seismic lines in the 1980s East China Sea cruise and "973" cruise nearby the East China Sea and the Okinawa Trough. The multichannel seismic lines are more than 7 300 km long. According to the water depth distribution of marine gas hydrate in the Okinawa Trough, from the northwest side slope deep water zone, we have selected 27 seismic profiles, 4 355 km long. There are 16 seismic lines with the existence of BSR. According to the gas hydrate controlling factors

and the physical characteristics, contrasting the different special processing results, it is found that are quite ideal processing technologies and methods for gas hydrate data, such as real amplitudes processing, wavelet processing, fine velocity analysis, prestack depth migration, AVO processing, wave inversion and three-instantaneous processing technology. They make the main characteristic of gas hydrate obvious [16]. By processing and interpreting the seismic data, we have identified the bottom-simulating reflector (BSR) in the north, middle and south of Okinawa Trough. We have identified the BSR in 16 seismic lines and the distribution area of the wider and typical region is in the middle and the south. Figure 1 shows the location of the BSR seismic line in the Okinawa Trough. The thick segment denotes the range of BSR appearing in the line and each line has the BSR distribution. This article will select several typical profiles to show the BSR characteristic and the distribution characteristic of the gas hydrate stability zone.

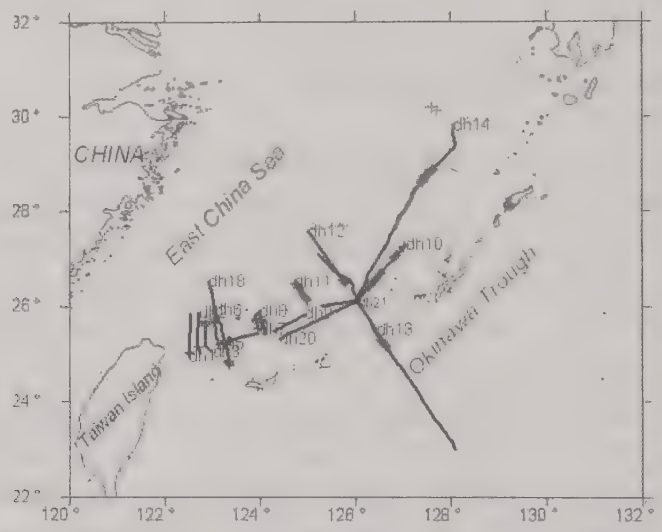

Fig.1 Multichannel seismic lines with BSR distribution in the Okinawa trough

The position of line Dh10 locates in 126°03′E and 127°03′E, 26°08′N and 27°18′N, at the deep water depth of the Okinawa Trough. The seabed two-way travel time is 2 300 ms, approximately 1 725 m in terms of water depth, and the line direction is NE-SW. The profile has an obvious weak amplitude - blank zone. The blank zone base is a continuous strong amplitude reflection, parallelling the seafloor stratum, the strong continuous amplitude reflection reversing the seabed phase, forming a clear contrast with the above blank zone. According to the bottom-simulating reflector character which has been confirmed in the world, the strong reflection in the blank zone may be identified for bottom-simulating reflectors. There is a BSR phenomenon in 2 800 ms of the two-way reflection time, the time from top to bottom is 500 ms, namely the thickness of natural gas hydrate stability zone is 250 ms. If the interval velocity of gas hydrate is 1 800 m/s, the thickness of gas hydrate stability zone (HSZ) is 450 m. The CDP range with BSR is 734 – 1666, 4700 – 6480, 13056 – 20218, the CDP spacing of 48 multichannel

seismic data is 12.5 m. Gas hydrate resource in theory is extremely considerable.

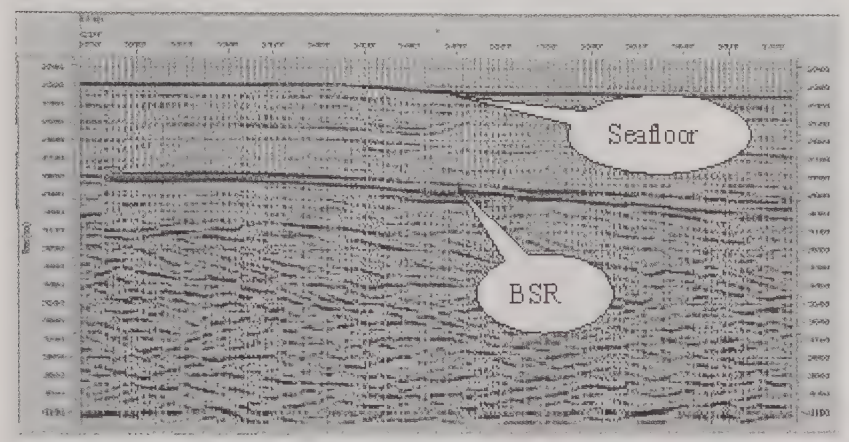

Fig.2 BSR of line DH10

DH11(Fig. 3) line locates in 124°43′E - 125°00′E, 26°06′N -26°32′N, on the west slope of the Okinawa Trough, and the line direction is NW-SE. Fig.3 shows the BSR's polarity phase, and the polarity in the 2 100 ms is opposite to the seafloor polar phase. It can be seen from wave inversion that the BSR's velocity has been changed. The CDP ranges from 500 to 3100 and from 5458 to 8676. The gas hydrate stability zone thickness is 150 ms after preliminary evaluation (converted to the thickness 270 m).

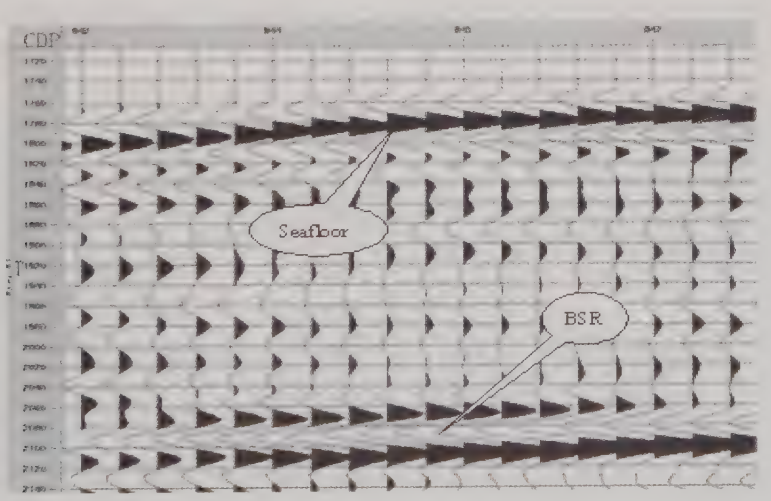

Fig.3 Polarity of BSR in the line dh11

DH6 line (Fig. 4) locates in 123°06′E – 123°01′E, 25°16′N – 25°55′N in the south of Okinawa Trough. Within the CDP 3274-5178, the profile appears a strong BSR phenomenon at 1 500 ms, and an obvious blank zone. The gas hydrate stability zone thickness is 450 m.

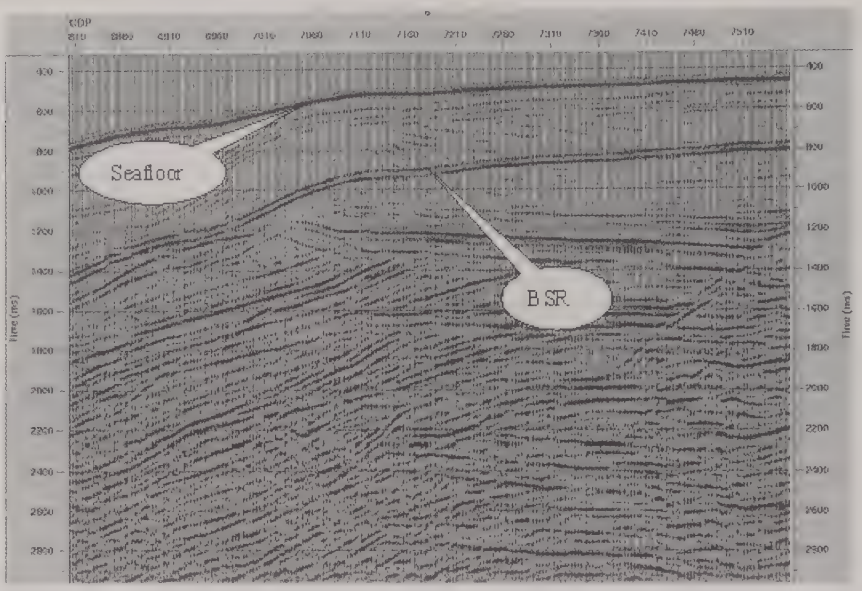

Fig.4 BSR of line DH6

DH7 line (Fig. 5) locates in 123°55′E – 124°00′E, 25°28′N – 25°48′N in the south of Okinawa Trough. BSR has been found in 3 200 ms with the polarity opposite to the seafloor. But there also appears the oppositing phase at 3 600 ms with the seafloor polarity. The observation shows this is the first double BSR phenomenon in the Okinawa Trough. The gas hydrate stability zone thickness is 495 m from CDP 858 to 1298.

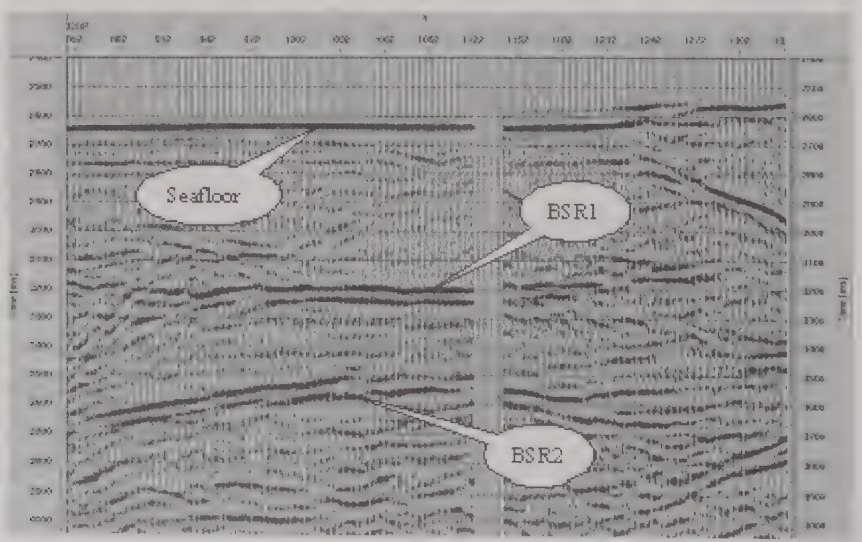

Fig.5 BSR of line DH7

2 Gas hydrate stability zone thickness in the Okinawa Trough

Gas hydrate stability zone thickness may be obtained mainly from the following two methods according to the material now available [17-20]. One method is through the geothermal gradient and the water temperature change curve, by drawing pictures, combining gas hydrate stability curves, obtaining gas hydrate stability zone thickness in various areas and water depths (Miles proposed temperature - pressure equation about the gas hydrate stability). Fang Yinxia et al.[17] gained formula from the seafloor to the bottom of stability zone according to Miles' (1995) proposed temperature - pressure equation about the gas hydrate stability, using the seabed temperature(t_0) and the temperature-water depth formula of geothermal gradient（g） and the transformation relations about the pressure P and the depth D, thereby having theoretically established the geometry algorithm of gas hydrate stability zone thickness; The other method is, through identifying the bottom-simulating reflector, with the BSR as the bottom of gas hydrate stability zone, to use the wave inversion, AVO technologies to determine the upper boundary of gas hydrate stability zone, and by considering the saturation and the porosity of gas hydrate stability zone, to calculate its thickness. The key to this method is the precise processing and analyzing of the interval velocity of gas hydrate, using the precise velocity to inverse the AVO technology for gas hydrate area and using the reservoir forecasting of petroleum seismic combined with the seismic profile blank zone to identify the BSR upper boundary. This research mainly uses the latter method, contrasting the former method to synthetically determine the gas hydrate stability zone thickness.

We have identified BSR in 16 seismic profiles among many processing seismic profiles. By means of wave inversion and AVO inversion, we have confirmed the BSR upper and lower boundaries, its velocity model using the interval velocity with DIX formula transformation. We calculate the BSR thickness to which each CDP corresponds (namely gas hydrate stability zone thickness) in 16 seismic profiles, transforming it into the data format which we need, making images as in Figure 6. BSR distribution and stability zone thickness are limited merely in the lines where BSR has been found (thickness unit is one-way reflection time, ms). According to the lines and thickness distribution, we may see:

a) BSR distribution is mainly limited to the arc slope of Trough.

b) BSR mainly distributes between the water depth 1 000 - 2 000 m, also appearing in 400 - 1 000 m, few appearing > 2 000 m;

c) The gas hydrate stability zone thickness may be divided into three zones: South, Central and North, taking 26° N and 28° N as boundary; The gas hydrate stability zone thickness in the south changes greatly, between 50 and 300 ms, stabilizing at 200 - 300 ms in most areas; 120 - 230 ms in the central area, 250 ms only in a small area; and 45 – 150 ms in the north;

In a word, the gas hydrate stability zone thickness in the south area is quite deep, the potential of hydrate distribution is biggest, the north area stability zone thickness is thin, and the potential of hydrate

is small; the probability of BSR occurrence in the central and south areas is large, and the stability zone thickness curves are concentrated.

3 Gas hydrate resource evaluation in the Okinawa Trough

By using the factors influencing the seabed gas hydrate formation and the stable distribution (gas hydrate source, sediment temperature and pressure and rock granularity), through analysis of the sediments filling character, organic matter distribution, and hot flow field in the Okinawa Trough, combining with water depth and water temperature, etc., and by applying the laboratory simulation experiment and the seabed gas hydrate stability curve using surveyed data, we may calculate the theoretical value of seabed gas hydrate resources in the Okinawa Trough. Contrasting the BSR distribution character and the gas hydrate stability zone thickness, we can preliminarily evaluate the actual resource of gas hydrate in the Okinawa Trough.

Gas volume in the gas hydrate may be calculated with the following formula:

$$V = Z \times A \times P \times H \times E$$

where, V is the gas volume (cubic meter), Z is the gas hydrate stability zone thickness (meter), A is gas hydrate area (square meter), P is the sediment average porosity (%), P is 40 % international porosity mean value and H is the sediment filled hole percentage in the gas hydrate stability zone (%). In accordance with ODP164 voyage drilling data, H in the Blake Ridge area is generally 1 %-10 %, and is bigger than 10 % in some sections. This article uses 5 % as the mean value. E is the natural gas volume equivalent formed by the gas hydrate decomposition. Under the standard pressure and temperature, 1 cubic gas hydrate may be decomposed into 164 cubics of gas.

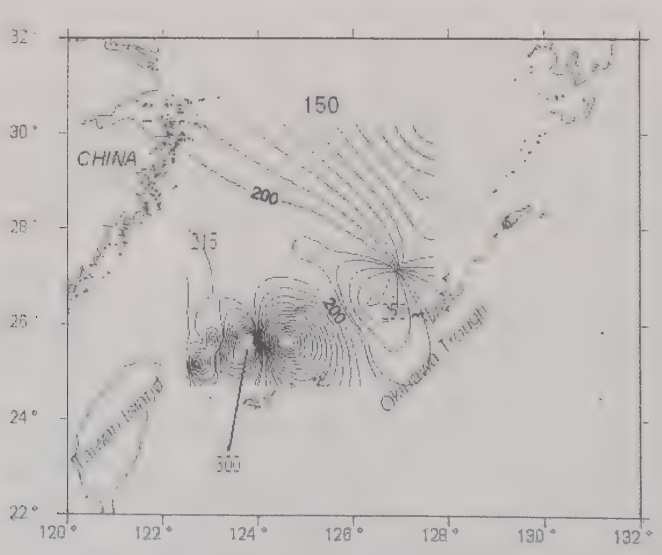

Fig.6 BSR distribution and hydrate stability zone sediment in the Okinawa Trough

According to the above parameters and the supposition, the measured data computation, the average

thickness taking the value 175 ms × 1 800 m/s = 315 m, the area 56 610 square kilometers, then the resource is 5.849×10^{13} cubic meters. If calculations is done by zones, the south area is 18 334 square kilometers, the thickness 315 m and the resource 1.8943×10^{13} cubic meters; The central area is 6 667 square kilometers, the thickness 150 m and the resource 0.33×10^{13} cubic meters; The north area is 31 669 square kilometers, the thickness 100 m and the resource 1.039×10^{13} cubic meters; Total resource is 3.26×10^{13} cubic meters, approaching the theoretical value of 2.4×10^{13} cubic meters as computated by Fang Yinxia [17].

These two values are quite close through contrasting theoretical and actual values and eliminating the uncertain erroneous factor. It is indicated that our method is reliable, and moreover that the Okinawa Trough has rich gas hydrate resources. This area will be the our country's next important resources prospecting region. Certainly, to find out the accurate resource deposits needs to obtain the relevant well drilling technical parameters in the Trough. According to the hydrate stability zone thickness and distribution range, even if the estimated content of gas hydrate in the entire sediment is 1 % - 3 %, there is still huge energy resource in the Okinawa Trough and its prospect is extremely attractive without doubt.

References

[1] Xu W, Rupple C. Predicting the occurrence, distribution, and evolution of methane gas hydrate in porous marine sediments. J. Geo-phys.Res., 1999, 104: 5 081-5 096.

[2] Fang Yinxia, Li Mingbi, Jin Xianglong et al. The formation analysis of gas hydrate in Okinawa Trough, East China Sea, Bulletin of Science and Technology. 2003(1): 1-5.

[3] Mallick S,Lauve J,Workman R. Analysis of bottom simulating reflector data. Soc.Expl.Geophys. Expanded Abstracts, 1998: 36-41.

[4] Ingo A Pecher, Timothy A Minshull et al. Velocity structure of a bottom simulating reflector offshore Peru: Results from full waveform inversion. Earth and planetary letters, 1996, 139: 459-469.

[5] Song Haibin. Seismic inversion prospect of marine gas hydrate. Inversion Research on Elastic Parameters of Stratified Media. Beijing: High Education Press, 2002: 98-102.

[6] Yuan G D, Spence R D, Hyndman et al. Seismic velocity studies of a gas hydrate bottom-similating reflector on the northern Cascadia continental margin: amplitude modeling and full waveform inversion. Journal of Geophysical Research, 1999, 104(B1): 1 179-1 191.

[7] Satish C Singh, Timothy A Minshull. Velocity structure of a gas hydrate reflector at Ocean Drilling Programe site 889 from a global seismic waveform inversion. JGR, 1994, 99: 24 221-24 233.

[8] Ganyuan Xia, Mrinal K Sen, and Paul L Stoffa. Mapping of elastic properties of gas hydrates in the Carolina trough by waveform inversion. Geophysics, 2000, 65(3): 735-744.

[9] Singh S C, Minshull T A, Spence G D. Velocity structure of a gas hydrate reflector. Science, 1993, 260: 204-207.

[10] Korenaga J, Holbrook W S, Singh S C et al. Natural gas hydrates on the southeast U.S. margin: constraints

from full waveform and travel time inversions of wide-angle seismic data. Geophys. Res., 1997, 102: 15 345-15 365.

[11] Susan E Minkoff and William W Symes. Full waveform inversion of marine reflection data in the plane-wave domain. Geophysics, 62(2): 540-553.

[12] Ma Zaitian, Gong Jianhua, Dong Liangguo. Seismic distinguish study of marine gas hydrate. Marine Geology &Quaternary Geology, 2002(1): 1-4.

[13] Song Haibin, Matsubayashi Osamu. Geopgysical researches on marine gas hydrate. Progress in Geophysics, 2001, 16(2): 118-126.

[14] Jin Xianglong. Marine Ggeology of East China Sea. Beijing: Ocean press, 1992: 323-330.

[15] Meng Xianwei. Possibility of gas hydrate occurring in the western lower slope of Mid-Okinawa Trough. Acta Sedimentologica Sinica, 2000, 18(4): 629-633.

[16] Tang Yong, Jin Xianglong, Fang Yinxia et al. Seismic study of gas hydrate BSR In Okinawa Trough. Acta Oceanologica Ainica, 2003, 25 (4): 59-66.

[17] Fang Yinxia. Calculation of gas hydrate stability zone in Okinawa Trough. Mineral Deposits, 2002, 21(4): 414-419.

[18] Fang Yinxia, Li Mingbi, Jin Xianglong. Character analysis of gas hydrate stability zone in seabed. Marine Geology & Quaternary Geology, 2001, 21(1): 103-106.

[19] Christine Ecker, Jack Dvorkin and Amos M Nur. Estimating the amount of gas hydrate and free gas from marine seismic data. Geophysics, 2000, 65(2): 565-573.

[20] Gong Jianming, Yang Wenda, Lu Zhenquan et al. Character of regional geology and possible perspective zone of gas hydrate in East China Sea. Marine Geology Letters, 2001, 17 (7): 20-23.

冲绳海槽天然气水合物稳定带特征和资源量评价

唐 勇[1, 2]，金翔龙[2]，方银霞[2]

（1. 中国地质大学研究生院，湖北 武汉 430074；

2. 海洋局海底科学重点实验室，国家海洋局第二海洋研究所，浙江 杭州 310012）

摘 要：根据冲绳海槽多道地震资料的处理解释，在 16 条地震剖面上发现了水合物拟海底反射层 BSR，经过 AVO、波形反演等特殊的处理技术，首次直接利用 BSR 圈定了冲绳海槽天然气水合物具体分布范围，直接利用数据得出了天然气水合物稳定带厚度在冲绳海槽的分布趋势，认为海槽南部最厚，中部次之，北部最薄，并通过计算得出了冲绳海槽水合物稳定带的厚度和水合物资源量，对今后海槽水合物勘查和资源量评价具有一定的指导意义。

关键词：BSR；天然气水合物；天然气水合物稳定带

Mechanism of Nutrient Silicon and Water Temperature Influences on Phytoplankton Growth

YANG Dongfang (杨东方) [1, 2, 3], GAO Zhenhui (高振会)[1], SUN Peiyan (孙培艳)[1],
LI Mei (李梅)[1], QU Yangfeng (曲延峰)[1]

1. *North China Sea Environmental Monitoring Center, SOA, Qingdao* 266033, *Shandong, China*;
2. *School of Environmental and Public Health, Wenzhou Medical College, Wenzhou* 325035, *Zhejiang, China*;
3. *College of Fishery Science, Shanghai Fisheries University, Shanghai* 200090, *China*

Abstract: This paper analyzed how nutrient silicon and water temperature influenced the variation of phytoplankton growth and the change of its assemblage structure, and probed the different characteristics of the variation of phytoplankton growth and the different profiles of the change of its assemblage structure influenced by nutrient silicon and water temperature. Taking Jiaozhou Bay for example, this paper showed the process of both the variation of phytoplankton growth and the change of its assemblage structure, unveiled the mechanism of nutrient silicon and water temperature influencing the variation of phytoplankton growth and the change of its assemblage structure, and determined that nutrient silicon and water temperature were the motive power for the healthy running of the marine ecosystem.

Keywords: silicon; water temperature; phytoplankton growth; assemblage structure; mechanism

Nutrients, water temperature and light are the important factors determining phytoplankton growth. Then, the most important factor among them for phytoplankton growth is nutrients; the second is water temperature; and the final is light [1]. They play roles in affecting phytoplankton growth in order.

The annual solar radiation in the Jiaozhou Bay is largely enough to sustain photosynthesis [2]. Therefore, the photosynthesis was not a limiting factor for phytoplankton growth and primary production. Thus, the limitation of nutrients and temperature was considered.

In the Jiaozhou Bay, nutrients N and P were sufficient and relatively richer than Si [3, 4], enough to meet the requirements of phytoplankton growth and reproduction. The limitation of nutrient Si therefore was mainly considered [5-10].

Silicate has a close relationship with the structure and metabolism of diatoms, and it may control the process of phytoplankton growth [11] and plays a key role in the bloom of phytoplankton [12]. Si is crucial for diatoms as a necessary requirement [13]. Without Si, valves would not be able to form, and the cell cycle would not be completed [14, 15]. Here diatoms predominated [12]. Nutrient silicon is found to be the main controlling factor for the primary production [5-8, 10, 16]. When nutrient silicon satisfied the

Received on May 8, 2006

phytoplankton growth, the controlling factor would be turned into the water temperature only [7, 10, 17-20]. So, taking the Jiaozhou Bay for example, this paper studies the mechanism of nutrient silicon and water temperature influencing the variation of phytoplankton growth and the change of its assemblage structure.

1 Mechanism of nutrient silicon influence on phytoplankton

1.1 Phytoplankton growth

In the Jiaozhou Bay (Fig. 1), the runoff into the bay provided abundant content of silicate, and the content of silicate assimilated by phytoplankton determined the primary production of phytoplankton, which unveiled that in spring, autumn and winter the silicate in the bay was a limiting factor for primary production [7]. In the Jiaozhou Bay, the decreasing concentration of silicate from terrestrial source is supposedly due to dilution by current and uptake of phytoplankton; In summer, the quantity of silicate assimilated by the bay's phytoplankton was about 13.33 - 73.58 t/d. The intrinsic conversion ratio of silicon into phytoplankton biomass was 0.229 - 0.542 mgC/μmol and the proportion of the quantity of silicon uptaken by phytoplankton and diluted by the water exchange was 6:94 - 20:80.

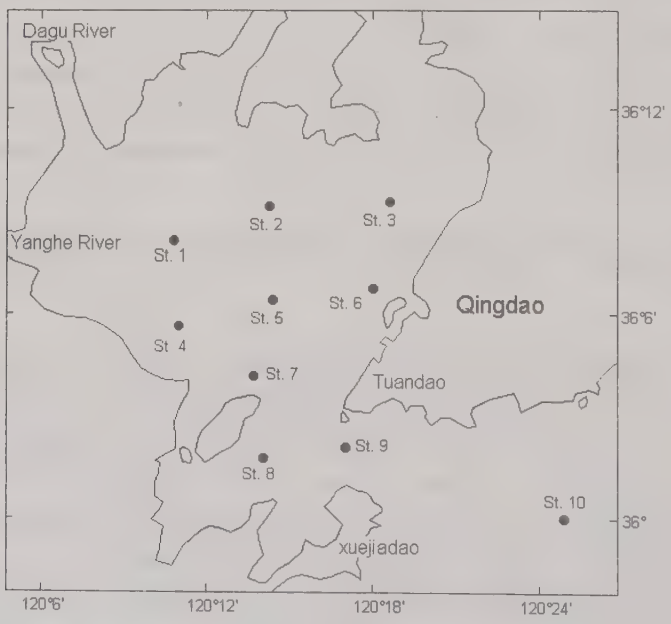

Fig.1 Investigation sites in the Jiaozhou Bay

The Si:DIN ratio was < 1 throughout the year in the Jiaozhou Bay; and the Si:16P ratio was < 1 throughout the Jiaozhou Bay in spring, autumn and winter. The results [16] proved that silicate limited phytoplankton growth in spring, autumn and winter in the Jiaozhou Bay.

Considering the nutrient concentration in the Jiaozhou Bay [16], analysis of discontinuous nutrient

data from 1962 to 1998 showed that nutrients N and P concentration kept invariable or had an increasing tendency; from1962, phytoplankton has never had the potential limitation by N and P. Analysis of between May, 1991 and February,1994 the nutrient data indicated that the annual cyclic change of silicate limits phytoplankton growth in spring, autumn and winter every year in the Jiaozhou Bay; and that in many Jiaozhou Bay waters, the phytoplankton as the predominant species need a great amount of silicate.

With the change of Jiaozhou Bay over thirty years, the N and P concentrations tended to rise; while Si concentration showed cyclic seasonal variations. According to the variation of nutrient Si limiting primary production, the range of the values of primary production is divided into three parts [9]: the basic value of Si limited primary production, the extent of Si limited primary production, and the critical value of Si limited primary production. When the silicate concentration in the Jiaozhou Bay declines to zero, the basic value of Si limited primary production is 125.28 - 256.47 mgC/m^2d; the extent of Si limited primary production is 182.04 - 485.06 mgC/m^2d; and the critical value of Si limited primary production is 336.05 - 610.34 mgC/m^2d.

The examination and validation of this vast space (Jiaozhou Bay) and very long time (6 months and 5 days in one year) investigation proved that nutrient silicon is a limiting factor of primary production in the Jiaozhou Bay [9]. The time of the critical value of Si limitation of phytoplankton growth in the Jiaozhou Bay is from about November 3 to November 13 in autumn; and that the time of the critical value of Si concentration satisfactory for phytoplankton growth in the Jiaozhou Bay is from about May 22 to June 7 in spring. The calculated critical value of Si concentration satisfactory for phytoplankton growth is 2.15 - 0.76 μmol/L; and the critical value of Si limitation of phytoplankton growth is 1.42 - 0.36 μmol/L. From these calculation results, the time period of Si limitation of phytoplankton growth is found to be from about November 13 to May 22 in the next year, the time period of Si concentration satisfactory for phytoplankton growth is from about June 7 to November 3. Consideration of the critical value of Si limitation on, and Si concentration satisfactory for, phytoplankton growth in autumn and spring showed that when the silicate concentration $s(t) < 0.36$ μmol/L, silicate concentration throughout the Jiaozhou Bay limits the phytoplankton growth; when 0.36 μmol/L $\leq$ silicate concentration $s(t) \leq 2.15$ μmol/L, the silicate concentration can potentially limit or be satisfactory for phytoplankton growth in the Jiaozhou Bay; when the silicate concentration $s(t) > 2.15$ μmol/L, the silicate concentration throughout the Jiaozhou Bay is entirely satisfactory for phytoplankton growth.

In the southwest part of the bay (Station 8) (Station E1), the predominant components of phytoplankton were different from the others in ecological character. The growth of the predominant *Asterionella japonica Cl.* in winter in the bay's southwest (Station 8) was delayed by two months compared with that of the station near it inside the Jiaozhou Bay, or even by three months compared with that at the north stations inside the Jiaozhou Bay [2]. In February in winter, the daytime lasts for around 11.3 hours, the irradiance is enough, the chlorophyll-a is high, the temperature is suitable, and nitrogen and phosphorous are ample for the predominant species *Asterionella japonica Cl.* in the Jiaozhou Bay. However, its reproduction was slow, because the silicate concentration was low in the

southwest (Station 8), resulting in the slow diatom growth [7].

The phytoplankton in the Jiaozhou Bay intensively needs silicon and is very highly sensitive and rapidly reacts, to the variation of silicate concentration. This unveils the whole process of the phytoplankton growth dependent on the dynamic variation of silicon.

1.2 Variation of phytoplankton assemblage structure

In the southwest part of the bay (Station 8) (Station E1), the proportion of the predominant warm species *Ceratium macrocers Cl.* to the total phytoplankton biomass increased obviously from July, a month earlier than that in the other stations in Jiaozhou Bay [2]. Since the silicate concentration of the southwest part of Jiaozhou Bay is lowest in the bay, however, from July to September, the warm species, *Ceratium macrocers Cl*, which does not belong to diatoms, grew in the southwest (Station 8), where diatoms were expected to grow. So, the much lower silicate concentration in the southwest part of the bay caused the space of diatom growth to be transformed into that of non-diatom growth [7].

In the southwest part of the Bay at Station 8, all the Si:DIN and Si:16P ratios were <1 throughout the year. This indicated that the nutrient Si limited the growth of phytoplankton throughout the year in some waters of the southwest part of the Bay. Under the environment deficient in silicon all the time, the diatom growth is constantly inhibited. Moreover, the marine space for diatom growth is occupied by dinoflagellates that gradually replace the diatoms. So, large changes in the food web and phytoplankton assemblage structure occur.

1.3 Mechanism of nutrient silicon influence on phytoplankton

Silicate plays an important role in the phytoplankton growth and the structure of phytoplankton assemblage.

Light is enough to satisfy the phytoplankton photosynthesis. In addition, water temperature keeps in the interval of the most appropriate temperature for phytoplankton growth, namely water temperature varies in the phytoplankton niche. Also, the absolute value and relative proportional value of nutrients N and P satisfy the phytoplankton growth, only the nutrient silicon limits phytoplankton growth. In this case, the consideration is the influence of the nutrient silicon variation on the variation of primary production and reproduction capacity.

Suppose the variations of primary production and reproduction capacity were a line, the influence of silicate variation on the variation of primary production and reproduction capacity obtained the variations of primary production and reproduction capacity limited by silicon limitation (Fig. 2).

When silicon was below the critical value of phytoplankton, with the drop of the silicon limiting the phytoplankton growth, primary production and reproduction capacity also fell; while with the rise of silicon, so do primary production and reproduction capacity. So, silicate variation had the same rise and drop as that of primary production and reproduction capacity limited by silicon.

Silicate limitation made the structure of phytoplankton assemblage shift. Phytoplankton with silicon deficiency had a high sinking rate, and in this way, the marine space belonging to diatoms was replaced and occupied by non-diatoms. With the variation of silicon limitation, an alternate shift in dominance occurred between diatoms and non-diatoms, and its shift process was rapid.

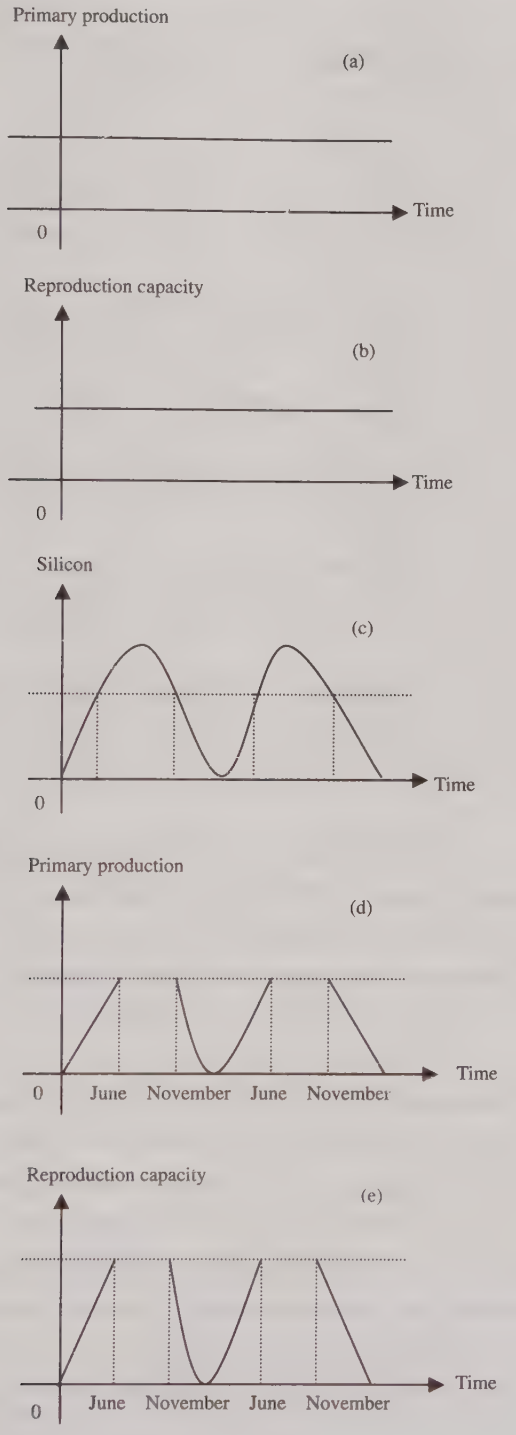

Fig. 2 (a) and (b) Given primary production and reproduction capacity variation; (c) Silicate variation; (d) and (e) primary production and reproduction capacity variation influenced by silicate variation

2 Mechanism of nutrient silicon influence on phytoplankton

2.1 Phytoplankton growth

The process of the water temperature affecting the on phytoplankton growth showed: in winter (January, February, March), because of its relative lowness, water temperature did not almost influence the phytoplankton growth.

In spring (April, May, June), the rise of water temperature enhanced the growth of warm species, limited that of cold species, and kept the eurythermal species growth well. With the nutrient silicon satisfying the growth of phytoplankton, phytoplankton started to accelerate its growth, especially after June 7, when all of the nutrients N, P and Si satisfied the growth of phytoplankton, the growth and reproduction of phytoplankton was rapid. The primary production and reproduction capacity showed a rising tendency in the whole Jiaozhou Bay.

In summer (July, August, September), when all of the nutrients N, P and Si satisfied the phytoplankton growth, with the water temperature further rising, phytoplankton growth had two variation patterns:

In the first pattern, from June 7 to August 21 or 22, the phytoplankton reproduction capacity (PRC) kept rising, and maximized in August. In this case, the PRC reached the strongest with the rising seawater temperature. From August 21 or 22 to November 3, with the seawater temperature falling, PRC began to fall.

In the second pattern, from June 7 to August 21 or 22, the PRC fell slowly, to a relatively lower value in August. Or from May to August the PRC almost did not increase, or fall. From August 21 or 22 to November 3, PRC began to rise while the seawater temperature falls. In November, it reached the second peak (the first peak in May). Consequently, the PRC did not follow the seawater temperature falling, but kept rising to the second peak. After November, it also decreased with the falling temperature.

In autumn (October, November, December), the continuous fall of water temperature limited the growth of warm species, enhanced that of cold species, and kept eurythermal species growth well. But, since in autumn the nutrient silicon began to limit the phytoplankton growth from November 13, the primary production and reproduction capacity showed a falling tendency in the whole Jiaozhou Bay.

In winter (January, February, March), the nutrient silicon limited phytoplankton growth, so the primary production and reproduction capacity was lowest in one year in the whole Jiaozhou Bay.

2.2 Variation of phytoplankton assemblage structure

The irradiation in the Jiaozhou Bay was sufficient to satisfy phytoplankton photosynthesis. Nutrient Si limited the phytoplankton growth from November 13 to May 22. However, the nutrients N, P and Si satisfied the phytoplankton growth from June 7 to November 3. Water temperature varied in a yearly cycle with time elapsing. In the Jiaozhou Bay, from June 7 to August 22, with the rise of water temperature, the structure of phytoplankton assemblage respectively shifted from cold species,

eurythermal species and warm species to warm species, eurythermal species and tropical coastal species. From August 22 to November 3, with the drop of water temperature, the structure of phytoplankton assemblage respectively shifted from warm species, eurythermal species and tropical coastal species into cold species, eurythermal species and warm species. The structure of phytoplankton assemblage continuously varied and alternated so that phytoplankton was adapted to the water temperature to keep its stable growth.

In most of the water areas in the Jiaozhou Bay, at stations1, 2, 4, 5, 6, 8, 10 (at 7 stations, there were 9 stations in all), the structure of the phytoplankton assemblage was mostly composed of eurythermal species and cold species (eurythermal species and warm species) of phytoplankton, but composed of less warm species (tropical coastal species).

In a small part of the water areas in the Jiaozhou Bay [20], at stations7, 9 (at 2 stations, there were 9 stations in all), the phytoplankton assemblage structure was composed of mostly eurythermal and warm species (eurythermal species and tropic coastal species) of phytoplankton, but composed of less cold species (warm species).

In summer, in most of the water areas in the Jiaozhou Bay [20], in the north and center of Jiaozhou Bay, the structure of the phytoplankton assemblage was mostly composed of eurythermal species and warm species, but composed of relatively less tropical coastal species. But at stations 7 and 9 in the southern near shore waters of Jiaozhou Bay, the structure of the phytoplankton assemblage was mostly composed of eurythermal species and tropical coastal species, but composed of relatively less the warm species.

2.3 Mechanism of water temperature influence on phytoplankton

Firstly, light was enough in waters to satisfy the phytoplankton photosynthesis. Secondly, the nutrients N, P and Si values were above the critical value of phytoplankton growth: N = 1 μmol/L, Si = 2 μmol/L, P = 0.1 μmol/L. In addition, the relative values of nutrients showed that any nutrients of N, P and Si had no potential limitation. According to the absolute and relative rules of nutrient limitation [16], there was no nutrient to limit phytoplankton growth among N, P and Si. Finally, water varied in a yearly cycle on a temporal scale. So, when light was sufficient for the phytoplankton growth and all the N, P and Si satisfied it, phytoplankton reproduction capacity showed the process of the water temperature influencing the phytoplankton growth.

Suppose the variations of primary production and reproduction capacity were a line (Fig. 2), the influence of water temperature variation on the variation of primary production and reproduction capacity obtained the variations of primary production and the reproduction capacity was enhanced or limited by silicon limitation (Fig. 3). The variation above the dashed line in Fig. 3 showed a protruding curve, which meant that light was sufficient for phytoplankton growth and all the N, P and Si satisfied it.

Water temperature and primary production had a variation of the same rise and fall (Fig.3). But since reproduction capacity was more relative with water temperature than primary production, reproduction capacity depicted more exactly the influence of water temperature on phytoplankton growth than primary production. Moreover, reproduction capacity powerfully indicated the effect of

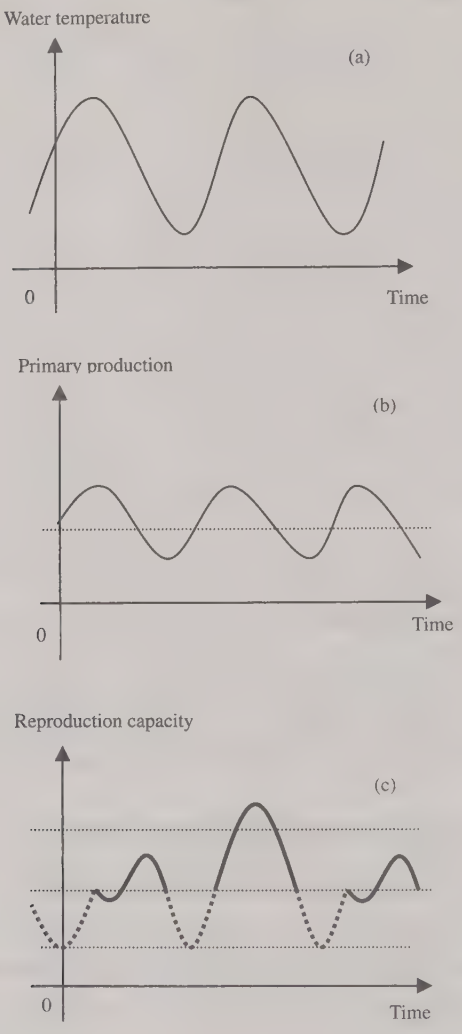

Fig. 3 Given primary production and reproduction capacity variation; (a) Water temperature variation; (b) and (c) primary production and reproduction capacity variation influenced by water temperature variation

water temperature on the physiology characteristics of algae growth: after the seawater temperature exceeded the range of the most appropriate temperature for phytoplankton growth, the algae died rapidly; In winter, when the seawater temperature continued to fall below that appropriate for algae growth, the influence of seawater temperature on the algae growth was not notable [21].

The PRC of phytoplankton had two varieties (Fig.3). One is: the PRC of phytoplankton increased with seawater temperature rising and decreased with seawater temperature falling, the reproduction in a one-peak pattern appeared; the PRC did not increase or even fell slowly with seawater temperature rising, the PRC started to rise slowly to the second peak value with seawater temperature falling, the

reproduction in a two-peak pattern appeared. Water temperature was the main motive power for one-peak or two-peak patterns.

In one year, seawater temperature had the dual functions of limiting and enhancing and inducing the PRC to have the same periodicity and variation trend as temperature. The basic explanation for the effect of seawater temperature on the reproduction is that the seawater temperature limits the photosynthesis by limiting the rate of the enzyme reaction of phytoplankton photosynthesis. So, seawater temperature had the dual functions of limitation and enhancement for phytoplankton growth.

Under the dual functions of water temperature, the structure of phytoplankton assemblage continuously shifted. When the water temperature rose from February to August, cold species, eurythermal species and warm species respectively replaced warm species, eurythermal species and tropical coastal species; When the water temperature dropped from August to February in the next year, cold species, eurythermal species and warm species respectively replaced warm species, eurythermal species and tropical coastal species.

Summary, if the seawater temperature of the water areas in summer did not exceed the most appropriate seawater temperature for the growth of the predominant species of the phytoplankton assemblage, phytoplankton in these water areas generally had a one-peak pattern; if the seawater temperature of the water areas in summer exceeded the most appropriate water temperature for the growth of the predominant species of the phytoplankton assemblage, phytoplankton reproduction in these water areas generally had a two-peak pattern. Generally, the phytoplankton assemblage structure with a one-peak pattern was composed of eurythermal species and warm species of phytoplankton; and the assemblage structure with a two- peak pattern was composed of eurythermal species and cold species of phytoplankton.

Water temperature influenced the structure of phytoplankton assemblage: cold species, eurythermal species, warm species and tropical coastal species, they alternated each other. With the water temperature having a continuously slow variation, the structure of phytoplankton assemblage continuously varied and alternated and its variation process was slow.

3 Conclusion

The variation of phytoplankton growth and the change of its assemblage structure was chiefly due to the drive of nutrient silicon and water temperature. Nutrient silicon was a main controlling factor; water temperature was a subordinate controlling factor. Nutrient silicon and water temperature controlled the variation in phytoplankton growth and the transition in its assemblage structure in the different phases and spaces.

As the transported quantity of silicon into sea in cycle tended to decrease, the nutrient silicon content in the sea also decreased; as the greenhouse effect played a role, the water temperature in the sea rose. The lack of nutrient silicon and the rise of water temperature would cause the change of the food chain basis in the marine ecosystem and that of the normal run of the marine ecosystem.

So far, human activities have already caused the lack of nutrient silicon and the rise of water temperature. How to keep the normal cycle variation of nutrient silicon and water temperature in the sea in order to provide a stable motive power for the better run of marine ecosystem was the crucial problem before human beings.

Acknowledgments

This study was funded by the Director's Foundation of the Beihai Monitoring Center and the State Oceanic Administration and Chinese Academy of Science (KZCX 2-207).

References

[1] Yang D F, Gao Z H, Wang P G, et al. The variation process of phytoplankton ecology in Jiaozhou Bay and the complementary mechanism in earth ecosystem. Beijing: Marine Press. 2005, 152-155.

[2] Guo Y J and Yang Z Y. Biological environment in Jiaozhou Bay: primary productivity. *In*: Liu R. ed., Ecology and Living Resources of Jiaozhou Bay, Beijing: Science Press. 1992, 110–125.

[3] Wu Y and Zhang Y. Chlorophyll-a of Jiaozhou Bay and characteristic distribution of primary productivity. *In*: Dong, J. and Jiao N. eds., Ecology Resources of Jiaozhou Bay, Beijing: Science Press. 1995, 137-150.

[4] Wang R, Jiao N Z, Li C, et al. Primary productivity of Jiaozhou Bay and new productivity. *In*: Dong J. and N. Jiao eds., Ecology Resources of Jiaozhou Bay. Beijing: Science Press. 1995, 125-135.

[5] Yang D F, Li H, Zhang Y M, et al. The factor and way of limiting nutrient for the growth of phytoplankton. Marine Sciences, 2000, 24(12): 47-50.

[6] Yang D F, Zhang J, Chen Y, et al. The uniqueness of nutrient limitation. Marine Sciences, 2001, 25(12): 49-51.

[7] Yang D F, Zhang J, Lu J B, et al. Examination of silicate limitation of primary production in the Jiaozhou Bay, North China Ⅰ. Silicate being a limiting factor of phytoplankton primary production Chin. J. Oceanol. Limnol., 2002, 20(3): 208-225.

[8] Yang D F, Gao Z H, Chen Y, et al. The biogeochemical process of silicon. Marine Sciences, 2002a, 26(3):35-36.

[9] Yang D F, Zhang J, Gao Z H, et al. Examination of silicate limitation of primary production in the Jiaozhou Bay, North China Ⅱ. Critical value and time of silicate limitation and satisfaction of the phytoplankton growth. Chin. J. Oceanol. Limnol., 2003a, 21(1): 46-63.

[10] Yang D F, Gao Z H, Sun P Y, et al. The studies of phytoplankton reproduction capacity. Marine Sciences, 2003, 27(5):26-28.

[11] Sakshaug E, Slagstad D and Holm-Hansen O. Factors controlling the development of phytoplankton blooms in the Antarctic Ocean—a mathematical model. Marine Chemistry, 1991, 35: 259-271.

[12] Conley D J and Malone T C. Annual cycle of dissolved silicate in Chesapeake Bay: implications for the

production and fate of phytoplankton biomass. Marine Ecology Progress Series, 1992, 81: 121-128.

[13] Lewin JC. Silicification. *In*: Lewin, R.E. ed., Physiology and Biochemistry of the Algae, Academic Press, New York. , 1962, p. 445-455.

[14] Brzezinski M A. Cell-cycle effects on the kinetics of silicic acid uptake and resource competition among diatoms. Journal of Plankton Research, 1992, 14: 1 511-1 536.

[15] Brzezinski M A, Olson R J and Chisholm S W. Silicon availability and cell-cycle progression in marine diatoms. Marine Ecology Progress Series, 1990, 67: 83-96.

[16] Yang D F, Gao Z H, Chen Y, et al. Examination of silicate limitation of primary production in the Jiaozhou Bay, North China III. Judgment method, rules and uniqueness of nutrient limitation among N, P, and Si. Chin. J. Oceanol. Limnol., 2003b, 21(2): 114-133.

[17] Yang D F, Gao Z H, Wang P G, et al.. The preliminary dissection of the daytime-length and water temperature's effect on the phytoplankton growth. Marine Sciences, 2002b, 26(12):18-22.

[18] Yang D F, Wang F, Gao Z H, et al. Ecological phenomena of phytoplankton in Jiaozhou Bay. Marine Sciences, 2004, 28(6):71-74.

[19] Yang D F, Gao Z H, Zhang J, et al. Examination of Daytime Length's Influence on Phytoplankton Growth in Jiaozhou Bay, China. Chin. J. Oceanol. Limnol., 2004a, 22(1): 70-82.

[20] Yang D F, Gao ZH, Chen Y, et al. Examination of Seawater Temperature's Influence on Phytoplankton Growth in Jiaozhou Bay, North China. Chin. J. Oceanol. Limnol., 2004b, 22(2): 166-175.

[21] Shen G. Y. and Shi B Z. ed. Marine Ecology. Xiamen: Xiamen University Press. 1990, 67-123.

营养盐硅和水温影响浮游植物的机制

杨东方[1,2,3]，高振会[1]，孙培艳[1]，李梅[1]，曲延峰[1]

（1. 国家海洋局北海环境监测中心，山东 青岛 266033； 2. 温州医学院环境与公共卫生学院，浙江 温州 325035；
3. 上海水产大学生命学院，上海 200090）

摘 要：通过研究分析 Si 和水温对浮游植物生长的变化和其集群结构的改变影响，探讨了硅和水温影响浮游植物生长的变化和其集群结构的改变，本文研究发现，浮游植物生长的变化和其集群结构的改变的过程，营养盐硅和水温影响浮游植物生长变化和其集群结构改变的机制，确定了营养盐硅和水温是海洋生态系统的健康运行的动力。

关键词：Si；水温；浮游植物生长；集群结构；机制

Forecast of Red Tide in the South China Sea by Using the Variation Trend of Hydrological and Meteorological Factors

ZHANG Junfeng (张俊峰)[1], BAI Yiping (白毅平)[1], YU Jianliang (俞建良)[1], PANG Hailong (庞海龙)[1], DENG Wenjun (邓文君)[1], LI Huajian (李华健)[1], WU Disheng (吴迪生)[1] , ZHAO Xue (赵 雪)[1], CHEN Huijun (陈惠君)[1], JIANG Yuejin (蒋跃进)[2]

1. *Forecast Center of South China Sea, Guangzhou* 510300, *Guangdong, China*

2. *South China Sea Environmental Monitoring Center, SOA, Guangzhou* 510300, *Guangdong, China*

Abstract: Many studies point out that weather conditions involving temperature, wind power, monsoon transform, air pressure, sea condition, tide, ocean current, salinity, eutrophic environment and so on are key factors causing Red Tide [1]. In the red tide high frequency areas of the South China Sea, the eutrophic environment of sea water has already existed, so the key elements such as meteorological and hydrological conditions play an importance role in the occurrence of red tide. The atmospheric circulation maintenance and variation decide whether meteorological phenomena, and hydrological key elements stabilize or change. Moreover, the red tide organisms' breeding from the initial stage to the blooming reproduction stage, until reaching the biological density of the red tide, generally takes 4 - 5 days. In the paper, the red tide examples are analyzed in the past 10 years, and the weather circulation situation and hydro-meteorological key elements of it are counted to find the previous circulation mode and bring out important factors inducing the blooming of red tide. The predicted result in 2003 according to this method was satisfactory.

Keywords: Red tide; meteorological condition; weather circulation

Introduction

Red tide is one of marine catastrophes in our country's inshore waters. For the recent ten years, red tide disasters have taken place frequently on a large scale, as a result of littoral economic development, accelerated process of urbanization and marine pollution. To carry out red tide forecast, prevention and control of red tide is a very urgent mission for effectively mitigating the catastrophic loss resulted from red tide.

Red tide forecast is a difficult scientific subject, and, there are no successful red tide forecast tools available for operational application in the world.It is reported that an expert in US applied the wind direction to forecast the red tide occurrence in a bay, that is to say, red tide is easy to take place when

Received on April 26, 2006

southwest wind prevails for a period over the bay. Up to now, there is no red tide forecast tools professionally applied in Japan even though it conducted red tide prevention and study earlier, established a complete monitoring system and made certain progress. What can be done for the occurrence of red tide is only follow-up monitoring, even the monitoring by means of satellite remote sensing is only a follow-up measure. Many researchers at home and abroad are in dire need of the forecast tools of professional operation. The variation trends of hydro-meteorological factors of ten days are applied to forecast whether red tide takes place in a period, which is of a great help for mariculture farmer to take countermeasures in advance. The followings discussion finds out the primary conditions and important factors triggering the red tide.

1 Analysis and choice of forecast factors for red tide

Preious research has pointed out that variation of the hydrological and meteorological factors is an essential inducement for the red tide blooming [2]. In the littoral waters where red tide occurs frequently, the water quality of South China becomes eutrophic especially in the rivers outlets and mariculture farms. Professor Qi Yuzao has pointed out: "Not all the eutrophic waters are the places in which red tide takes place frequently. Meteorological and hydrological factors, such as wind, current, tide and water temperature" triggering red tide are key factors [3]. This paper statistically analyzes the hydrological and meteorological factors in the red tide occurring cases in recent more than ten years. As compared with the biological and chemical data observed in recent two years in the monitored waters of red tide, the analysis results show that the water quality is eutrophic, and pH, DO, chlorophyll a, COD, phosphate, nitrite, nitrate, ammonia exist. However, the annual, monthly, ten days' and five days' variations of these biological and chemical data are weak. There is no evident distinctness for pH and DO when the data, which were observed with red tide occurrence or without red tide occurrence in the monitored waters of red tide, are compared with each other. As yet, to forecast red tide has not been successful only by means of biological and chemical data (mid-term red tide forecast). The atmospheric circulations, hydrological and meteorological factors, which have an effect on red tide organisms' reproduction, are of predictability while the biological and chemical factors are not. Therefore, the hydrological and meteorological factors (wind, wave, sea current, SST and sunlight) are dominant factors for the forecast of red tide. The hydrological and meteorological factors, moreover, depend on the weather circulation, which controls and affects a certain waters, and predicting the status variation of weather circulation is a key to forecasting red tide.

2 Choice of weather circulation status model in prophase of red tide blooming (the first 5-7 days before)

The reason why the statistical counting of weather circulation status is conducted in the prophase of red tide blooming, i.e., the first 5 - 7days, is that the culture testing of red tide organisms is carried out mostly at constant temperature, and that the testing course from the prophase, the blooming of red tide

up to reaching the red tide density takes four or five days at lab. In fact, SST in the waters in which red tide occurs varies a little daily as affected by tidal, wave, wind current as well as sunlight. In addition, there are a variety of marine algae and interaction between them, and then the evolution course of red tide organisms needs a longer time, generally five to seven days. Thus, taking five to seven days to statistically count is suitable.

Based on the count and classification of weather circulation in the red tide prophase from the year 1984 to 2001, the similar weather circulation models have been found and the results are very satisfactory. That is, the hydrological and meteorological factors keep under the stable weather circulation situation, lasting four or five days or more. The weather circulation conditions in the prophase of red tide are analyzed and classified to choose one weather circulation, which affects the occurrence of red tide, as a forecast model. And then, the forecast testing is conducted in combination with the hydro-meteorological factors. The selected forecast model and factors are as follows.

2.1 Statistical analysis of weather circulation conditions at the 500 hPa altitude in the prophase of red tide blooming

By statistically counting, it is found that the weather circulation conditions at the 500 hPa altitude in the prophase of red tide (around the first one week) mostly are controlled by the ridge back and trough front of subtropical high, while by a weak high-pressure or isobaric zone in spring and autumn, and by a 500 hPa high-pressure zone in winter. The contour of mid-latitude and high-latitude is found to be straight and there is no long-wave trough affecting the forecasted waters. It is fine, with sufficient sunlight and there is no cold air stroke over the waters under the control of this weather system. The airflow drops down and warms up adiabatically, and then the air temperature goes up rapidly, so does the water temperature. In summer, near the edge of high-pressure zone the southwest airflow from the trough front provides the condition for transporting warm and humid airflow. On the 30th Apr. to the 3rd May in 1990, a red tide event occurred in the waters nearby Changhua River and Lin'gao Bay off northwest Hainan, with an area of 5 000 km^2, when the southwest airflow coming from the western side of subtropical high had been controlling the waters in the prophase of red tide blooming (as shown in Fig. 1).

In summer, i.e., in Jul., Aug. and Sept., SST is high and sometimes goes beyond 30℃, which is unfavourable for the reproduction red tide organisms even though the waters controlled by a 500 hPa high is calm and sunny.

As yet, in the 500 hPa high-pressure map, in the prophase of red tide (the first 4 - 5 days) there are no sea areas found in the rear end of the thick and large East Asian Trough because on the sea surface, corresponding to the thick and large East Asian Trough, the strong cold air prevails. In such a way, if the waters is dominated by the thick and large East Asian Trough with 500 hPa recently or several days later, the hydrological and meteorological conditions of waters are not suitable for the red tide to take place in aftertime. Otherwise, red tide organisms would die away soon (in 24 hours) if the red tide occurs before the advent of the large East Asian Trough.

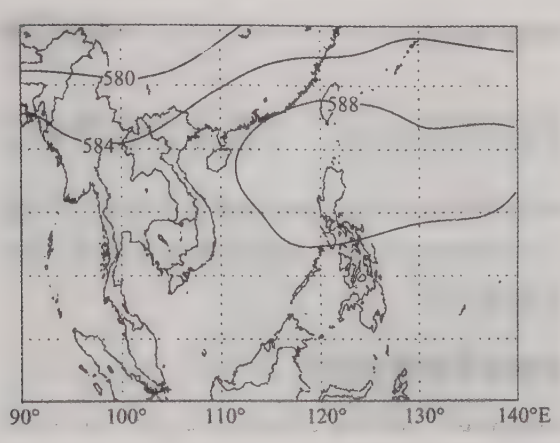

Fig.1 500 hPa weather conditions in favor of red tide occurrence (Apr., 1990)

2.2 Statistical analysis of weather circulation conditions at 850 hPa low altitude in prophase of red tide blooming

The results of analysis based on multi-annual data observed previously (from the year 1984 to 2001) indicate: in spring or autumn the southwest airflow of trough front at the 850 hPa low altitude overwhelms most waters in the prophase of red tide blooming, and the southwest wind velocity is larger (wind velocity amounts to 8 - 12 m/s). Affected by the southwest airflow of trough front, the air temperature over waters goes up, the air pressure lowers relatively and the weather is sweltering. Under the high air temperature condition for a long time, SST rises and keeps for a certain period. All of these are of great advantage to the red tide organisms' growth. The denaturalized high-pressure zone at 850 hPa or the back of high pressure controls the waters in winter (as shown in Fig. 2).

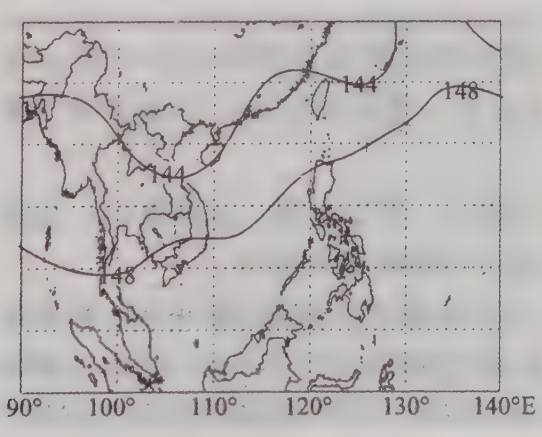

Fig.2 850 hPa weather conditions in favor of red tide occurrence (Apr., 1990)

2.3 Statistical analysis of weather circulation conditions over ground in the prophase of red tide blooming

On the basis of the previous data analysis, in the prophase of red tide blooming the weather situation over ground behaves as follows: frequently there are stationary fronts in spring in the Nanling region, the waters off South China is controlled by the southwest airflow or the southeastern side of the southwest low eddy, with the southwest a wind blowing and wind power of less then force 4. In autumn, the waters is controlled by a weak high or isobaric field while controlled by a denaturalized high or warm high in the prophase of red tide blooming in winter. Thus, in or over the waters there are little waves, poor exchange among water bodies, strong sunlight, high air temperature, which results in the rise of water temperature. In this way, the rise and stability of SST are advantageous to the red tide organisms' growth (Fig. 3 presents an example).

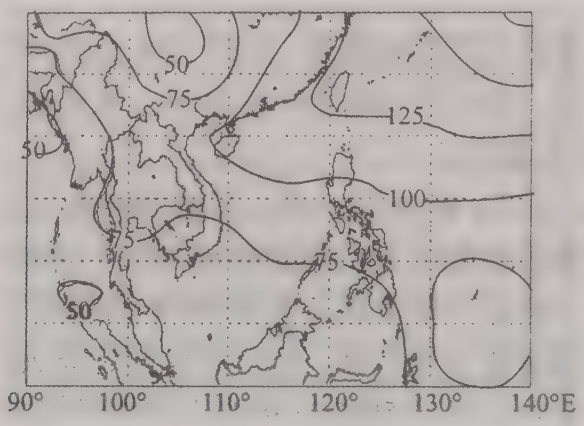

Fig.3 Ground weather circulation conditions in favor of red tide occurrence (Apr., 1990)

3 Statistical analysis of hydrological and meteorological factors in the prophase of red tide blooming (the first 5 - 7 days)

In the prophase of red tide blooming, variation and stability of the hydrological and meteorological elements depends on the stability and maintenance of the above-mentioned weather situation, and the weather is distinct at high, low altitude and ground, thus it is necessary to statistically analyse the variation of hydrological and meteorological factors.

3.1 Statistical analysis of SST variation in the prophase of red tide blooming

The SST counting period is from 1984 to 2001, counting three times every day. These data have been statistically analyzed and the results are as follows (as shown in Table 1).

In the prophase of red tide occurrence, based on the table, SST keeps stable, ranging from 18 to 30 ℃ (less than 30 ℃ accounting for 94.0 %). Therefore, the SST range between 18 ℃ and 30 ℃ is taken as one of the judging conditions favourable red tide blooming.

In addition, there is no evident SST daily variation found in accordance with the analysis (SST keeps the quasi-constant temperature in the prophase of red tide occurrence [5]), with a daily range of 0.6 ℃ on the average. As above, the SST daily average variable less than 1 ℃ (making up 90 %) is employed as one of the judging conditions favourable for red tide growth (as shown in Fig 4).

The distinct genera of red tide algae adapt themselves to different water temperatures (due to the limited data, no relationship among algae species and water temperature has been exactly and statistically counted as yet).

Tab.1 SST daily variation and wind velocity average (Seven days before red tide occurrence)

No	Blooming time of red tide	Blooming place	Algae genera or species	Cloudage & weather	Daily mean variation of water temperature in the prophase of red tide blooming and average water temperature in the red tide course /℃		Average wind velocity /m·s^{-1}	Wind direction
1	Jul. 16 - Aug. 3, 1984	Waters near Dangan Islands	*Trichodesmium* sp	Partly cloudy	0.8	28.9	6.7	SW
2	Jul. 27, 1984	Waters off Leizhou Peninsula	*Trichodesmium* sp	Cloudy	0.7	30.7	7.7	SSW
3	Feb. 15-17, 1988	Dapeng Bay	*Noctiluca scintillans*	Light fog	0.2	17.8		
4	May 9-19, 1988	Shenzhen Bay	*Dinophceae*	Cloudy	0.9	24.1		
5	Dec. 23-26, 1988	Yantian, Dapeng Bay	*Noctiluca scintillans*	Cloudy		18.3		
6	2-4 Apr, 1989	Chiwan, Shenzhen	*Prorocentrum* sp.	Cloudy	0.6	28.8	4.9	ENE
7	Apr. 17-20, 1989	Dapeng Bay	*Noctiluca scintillans*	Partly cloudy	1.0	21.5	4.3	E
8	Jan. 26-27, 1990	Yantian, Dapeng Bay			0.4	16.7	4.0	NNE
9	Feb. 13-17, 1990	Dapeng Bay	*Noctiluca scintillans*	Cloudy	0.6	16.7	3.4	ENE
10	Mar. 10-13, 1990	Dapeng Bay	*Noctiluca scintillans*	Cloudy	0.7	16.3	3.9	E
11	Mar. 18-19, 1990	Dapeng Bay	*Noctiluca scintillans*	Cloudy	0.9	19.2	4.0	ENE
12	Mar. 20-24, 1990	Dapeng Bay	*Noctiluca scintillans*	Cloudy	0.7	19.2	4.7	ENE
13	Apr. 1-2, 1990	Yantian, Dapeng Bay		Partly cloudy - Cloudy	0.5	21.4	5.0	SSE-SSW
14	Apr. 7-9, 1990	Shenzhen Bay	*Noctiluca scintillans*	Cloudy	0.9	21.6	4.9	ENE
15	Apr. 7-10, 1990	Guishan Island	*Noctiluca scintillans*	Fine	0.4	21.6	5.3	S-ENE
16	Apr. 15-17, 1990	Dapeng Bay	*Noctiluca scintillans*	Cloudy	0.5	21.1	4.1	E
17	Apr. 18-20, 1990	Dapeng Bay	*Noctiluca scintillans*	Cloudy	0.4	21.1	4.1	E-NE
18	Apr. 19-20, 1990	Yantian, Dapeng Bay		Cloudy	0.3	21.1	5.4	ENE
19	May. 10-15, 1990	Dapeng Bay	*Noctiluca scintillans*	Partly cloudy		24.2	3.6	E
20	Jun. 10, 1990	Dapeng Bay	*Thalassiosira subtilis*	Cloudy	0.6	27.1	4.9	SSW
21	Dec. 5, 1990	Dapeng Bay	*Pseudo-nitzschia pungens*	Cloudy	0.5	20.8	5.3	NNE
22	Dec. 23, 1990	Dapeng Bay	*Pseudo-nitzschia pungens*	Partly cloudy	0.2	20.3	3.4	NNE
23	Mar. 1, 1991	Shekou, Shenzhen		Partly cloudy	0.3	17.8	3.9	ENE
24	Mar. 10-13, 1991	Dapeng Bay	*Gymnodinium* sp.	Partly cloudy	0.5	20.3	4.6	E
25	Mar. 19-21, 1991	Yantian, Dapeng Bay	*Phaeocystis pouchetii mican*	Cloudy	0.4	21.0	3.9	E
26	Apr. 9, 1991	Dapeng Bay	*Noctiluca scintillans*	Partly cloudy	0.5	20.6	4.3	ENE
27	Apr. 17-18, 1991	Yantian, Dapeng Bay		Fine	0.8	23.7	6.2	S

Tab.1 SST daily variation and wind velocity average (Seven days before red tide occurrence)

(continued)

28	May 5-6, 1991	Yantian, Dapeng Bay	*Eonyaulax polygramma*	Overcast to cloudy	0.6	25.0	5.9	ENE
29	Jun. 2, 1991	Dapeng Bay	*Leptocylindrus danicus*	Cloudy	1.0	29.3	4.5	SSW
30	Jul. 6, 1991	Dapeng Bay	*Pseudo-nitzschia*delicatissma	Cloudy	0.9	28.9	7.3	S
31	Sept. 4, 1991	Dapeng Bay	*Pseudo-nitzschia*delicatissma	Partly cloudy	1.1	29.5	2.9	ENE
32	Dec. 23-24, 1991	Yantian, Dapeng Bay	*Noctiluca scintillans*	Partly cloudy	0.5	20.3	3.6	NE
33	Apr. 21-22, 1992	Yantian, Dapeng Bay	*Noctiluca scintillans*	Cloudy	0.9	20.5	3.8	S
34	Apr. 24, 1992	Yantian, Dapeng Bay	*Noctiluca scintillans*	Cloudy	0.8	21.3	5.8	S-SSW
35	Apr. 29, 1992	Dapeng Bay	*Noctiluca scintillans*	Partly cloudy	1.1	23.9	5.1	S
36	May 5, 1992	Dapeng Bay	*Noctiluca scintillans*	Partly cloudy	1.1	25.7	6.3	SSW
37	Oct. 22, 1992	Dapeng Bay	*Thalassionema nitzshioides*	Partly cloudy	0.3	25.4	4.2	E
38	Nov. 3, 1992	Dapeng Bay	*Rhizosolenia alata f. gracillima*	Partly cloudy	1.0	23.8	4.0	ENE
39	Apr. 26-30, 1996	Shekou, Shenzhen	*Skeletonema* sp.	Cloudy	0.7		4.9	SE
40	Nov. 26, 1997	Zhelinwan, Guangdong	*Phaeocystis* sp.	Partly cloudy	0.6	21.7	2.9	ENE
41	Dec., 1997	Zhelinwan, Guangdong	*Phaeocystis* sp.	Partly cloudy	0.5	19.0	4.1	ENE
42	Jan.-Feb., 1998	Qiuanzhou, Shanwei	*Phaeocystis pouchetii*	Partly cloudy	0.5	16.8	4.0	ENE
43	Mar.-Apr., 1998	The Pearl River Estuary	*Gymnodinium mikimotoi*	Partly cloudy	0.6	21.1		
44	Apr., 1998	Waters off West Shenzhen	*Pyrrophyta, Bacillariophyta*	Partly cloudy	0.5	23.9		
45	May 18, 1998	Daya Bay	*Pyrrophyta*	Cloudy	0.7	28.8		
46	Sept. 10, 1998	Daya Bay	*Scippsiella trochoidea*	Cloudy	0.5	28.7		
47	Nov. 8-9, 1998	Daya Bay	*Mesodinium rubrum*	Partly cloudy	0.3	23.1		
48	Mar. 14-15, 1999	Nan'ao, Dapeng Bay	*Eonyaulax polygramma*	Partly cloudy	0.6	21.1	3.8	ENE
49	Mar. 25-29, 1999	Dapeng Bay		Cloudy	0.4	21.2	4.1	SE
50	May 20-26, 1999	Huizhou, Daya Bay	*Peridinium pentagonum*	Cloudy	0.9	26.9	4.8	S
51	Aug. 17-20, 2000	Aotou, Huiyang	*Scippsiella trochoidea*	Partly cloudy	0.9	30.4	3.7	S
52	Sept. 3-6, 2000	Daya Bay	*Scippsiella trochoidea*	Partly cloudy	0.5	28.4	3.9	S-SE
53	Sept. 3-6, 2000	Dameisha, Xiaomeisha, Shenzhen		Partly cloudy	0.5	28.4	3.9	S-SE
54	Feb. 3-23, 2001	Dapeng Bay	*Gymnodinium sanguineum*	Cloudy	0.2	18.8	2.6	N
55	Feb. 26 - Mar.1, 2001	Dachanwan, The Pearl River Estuary		Partly cloudy	0.9	20.2	2.9	S-SW
56	Mar. 5-7, 2001	Yantian, Dapeng Bay	*Heterosiyma* sp.	Cloudy	0.4	19.9	3.4	ENE
57	Mar. 17-25, 2001	Shenzhen Bay	*Thalassiosira* sp.	Cloudy	0.5	21.8	3.2	ENE
58	Mar. 22-28, 2001	Yantian, Dapeng Bay	*Eonyaulax polygramma*	Cloudy	0.9	22.7	3.3	SW SE
59	Apr. 18-23, 2001	Xiaomeisha, Shenzhen	*Heterosiyma* sp.& *Phaeocystis pouchetii*	Cloudy	0.6	22.9	3.1	S-E
60	Apr. 23-28, 2001	Beiguan, Shenzhen	*Phaeocystis pouchetii*	Cloudy	0.6	23.5	4.0	SE
61	Apr. 28 - May 2, 2001	Dameisha, Xiaomeisha, Shenzhen	*Heterosiyma* sp.	Cloudy	0.6	24.0	3.8	SE
62	Jul. 10-13, 17, 2001	Waters near Hongkong Island, Daya Bay		Partly cloudy	0.5	28.0	6.9	SE
63	Sept. 10-20, 2001	Beiguan, Dongshen, Shenzhen		Partly cloudy	0.6	29.0	3.4	ENE-E
64	Average				0.6		4.6	

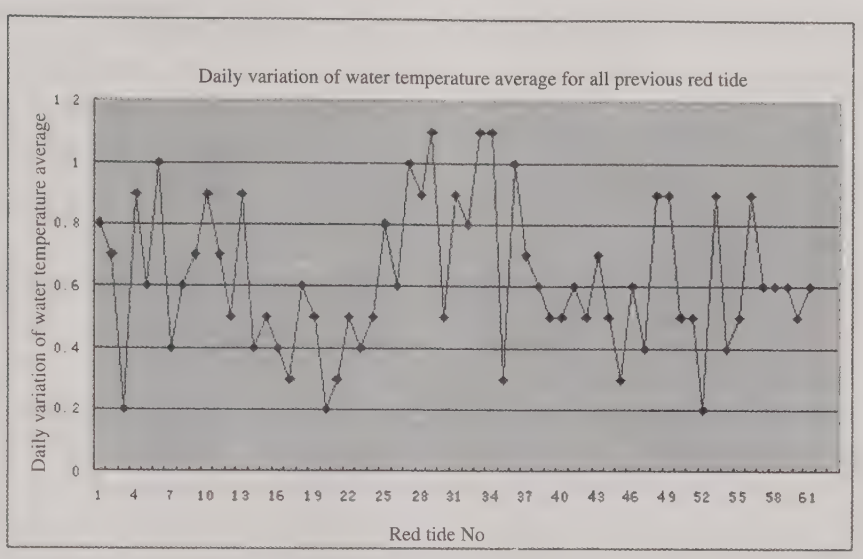
Daily variation of water temperature average for all previous red tide
Daily variation of water temperature average
1.2
1
0.8
0.6
0.4
0.2
0
1 4 7 10 13 16 19 22 25 28 31 34 37 40 43 46 49 52 55 58 61
Red tide No

Fig.4 Daily variation curve of SST for 63 red tide events from the year 1984 to 2001

3.2 Statistical analysis of wind direction and velocity in the prophase of red tide blooming

The counting results of wind velocity during red tide occurrence in the past years show that in the prophase of red tide the average daily wind speed amounts to below force 4 (7 m/s); for wind direction, in winter the southwest or south wind blows mostly in the prophase but the wind power is force 3 (5 m/s) when the north or northeast wind prevails, and the wind direction variation is not obvious in summer. Statistical results indicate that there is no red tide event occurring under the gale (force 6 or over) and rough sea conditions, in other words, the red tide event will not soon take place in the waters where the gale overwhelms several days in succession (as shown in Table 1). Thus, the average daily wind speed less than force 4 (7 m/s) serves as one of the judging conditions favourable for the red tide blooming.

3.3 Statistical analysis of wind wave and surge in the prophase of red tide blooming

The condition of wind wave height larger than 1.5 m is disadvantageous to the red tide formation. Because of larger wind wave, the upper and bottom seawaters exchange evidently, and then the daily SST varies greatly and unstably, which is unfavourable for the red tide organisms' reproduction. The statistical data indicate: the wind wave height is mostly below 1.2 m in the prophase of red tide occurrence. For instance, five days before two red tide events, one occurred in the outer waters of the Pearl River Estuary, i.e. Dangan Island (in Jul., 1984) and the other in the waters near Weizhou Island, the wave heights on the average amounting to 1.1 m and 0.8 m respectively. According to the wind speed mentioned in the above table, the wave height can be calculated to be less than 1 m. As a result, the wave height less than 1.2 m is taken as one of the judging conditions favourable for the red tide blooming.

3.4 Sunlight variation analysis in the prophase of red tide blooming

Some studies point out that the sweltering weather, continuous drought and high temperature (not in summer) is an important factor triggering the red tide [7]. For example, the following red tide events, one at Zhelinwan of Shantou from Dec., 1997 to Feb., 1998, the other in the waters off Shantou respectively from Nov., 2003 to Jan., 2004 and Nov., 2004, occurred when there were successive drought and enough sunlight.

The statistical analysis of cloudage based on the above-mentioned table indicates that the weather is partly cloudy or cloudy when most red tides occur, that is to say, the sunlight is enough. In different seasons, the sunlight effect on the red tide is different. In summer (Jul. – Sept.), strong sunlight irradiates the sea surface, results in a higher SST (larger than 30 ℃) which is disadvantageous to the red tide organisms' growth. The cloudy or overcast weather is in favor of red tide organisms developing. In autumn and winter (only limit to the South China Sea), there are drought and few rainfalls, the weather is fine – partly cloudy, with enough sunlight, and warm SST, all of which is advantageous to the red tide blooming. Sometimes, even it is cloudy or overcast but sweltering, the ambient waters is still suitable for red tide organisms to grow up in weak sunlight. Thus, the long sunlight duration is accounted as one of the judging conditions in favor of the red tide blooming.

3.5 Statistical analysis of sea surface current variation in the prophase of red tide blooming

Based the analysis of sea current and climatic data of the South China coast, in spring and autumn, the southwest wind prevails over the inshore off South China for a long time, easily resulting in a warmer wind-born current by south, and a higher SST in the waters, which is advantageous to the red tide organisms' occurrence and the outbreak of red tide. In winter, the northeast wind overwhelms for a long time with an alongshore cold sea current and surge-born current occurring, and under such circumstances, the red tide is not easy to take place as the waters is disadvantageous to the red tide organisms' reproduction.

3.6 Analysis of salinity variation in the prophase of red tide blooming

Due to the limited data, there are few samples for salinity variation analysis in the waters, in which the red tide occurs. But, in general, the salinity becomes smaller [6] in the prophase of red tide while the red tide is not easy to occur in the higher salinity waters (salinity is over 32). Thus, the seawater salinity is considered as one of the judging conditions in favor of the red tide blooming as well.

4 Establishment of forecast tools

Based on the above hydrological and meteorological factors, the forecast map of distinguishing flow is established, and then the forecast model of synoptic picture is configured in combination with the synoptic map category. The duration of future weather advantageous to the red tide occurrence is reckoned to judge whether the waters is in favor of red tide outbreak or not, according to the index values of hydro-meteorological factors.

4.1 Forecast model depending on weather circulation

The weather situation, which is advantageous to the red tide blooming, is accounted as an important judging criterion. The four primary categories are presented as follows.

4.1.1 Southwest monsoon category

In the northern waters of the South China Sea, red tide takes place every season all the year around (as shown in Fig 5), but most occur in the end of winter, spring and early summer (from Feb. to Jun.). When the weather is fair and warms up with enough sunlight after rainstorm [6], the red tide is easy to take place.

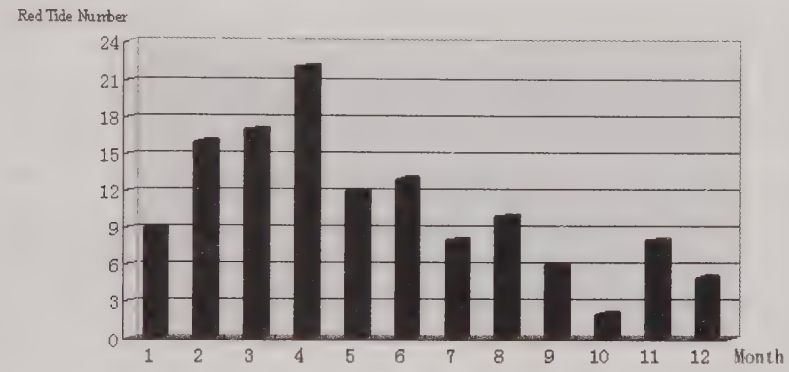

Fig.5 Monthly distribution of red tides from 1980 to 2004 in the waters of the South China Sea

4.1.2 Southwest inverse trough category

Spring and early summer see this category frequently, now and then there are inverse troughs found in the western part and the east of the southwestern part of South China. At this time, the southwest airflow, coming from the southern part of the inverse trough, dominates along the South China coast. The warm and humid airflow heads for the South China coast, which is under the control of the southwest airflow from the northwest side of the 500 hPa sub-tropical high ridge.

4.1.3 Linnan stationary front category

Most of this category is seen in the early spring. The stationary front is situated near the Nanlin Mountain, and the warm and humid airflow on the south side of frontal surface overwhelms over the South China coast. At high altitude, the 500 hPa sub-tropical high frequently controls the South China coast; at low altitude, i.e. 850 hPa, the shear line prevails near the Nanlin Mountain. The southwest race is obvious at low altitude (the figure is omitted), the corresponding sea surface is the southwest wind but the wind power is less than force 4.

4.1.4 Category of cold high denaturalization at low altitude

In the end of spring, early summer and autumn, the cold high denaturalization is constantly detained

in the South China coast. The waters, dominated by the denaturalized high, see drought and little precipitation, calm sea and enough sunlight. These conditions are advantageous to the going up of seawater temperature, but the seawater temperature has little daily variation.

The appearance and maintenance of above four categories of weather circulation are one of the essential and natural environment conditions supporting red tide organisms' reproduction. What is more, only when the occurrence of any kind of categories maintains for 5 days or more, can red tide organisms bloom. Thus, to exactly predict the weather situation one week in the future is a key to the forecast of red tide occurring conditions.

4.2 Forecast and judgement model establishment of red tide occurring conditions

The above-mentioned hydro-meteorological factors, such as wind. wave, seawater temperature, salinity, are digitized.

By means of the successful digital weather forecast, the future variation trend of wind, wave, seawater temperature, and salinity are analyzed to distinguish if these factors arrive at or approach the forecast values. The variation trend of sea surface current and sunlight are analyzed, and then the future weekly status (or a period of ten days) is analyzed to see whether not only anyone of the above weather circulation categories will take place but also this circulation will keep five days and more in succession. The waters is forecasted to be advantageous to the red tide occurrence, if the waters meets with the above conditions, otherwise it is disadvantageous to the red tide occurrence. The discriminatory flow chart of red tide forecast is shown as follows.

4.2.1 Forecast flow chart of red tide (as shown in Fig. 6)

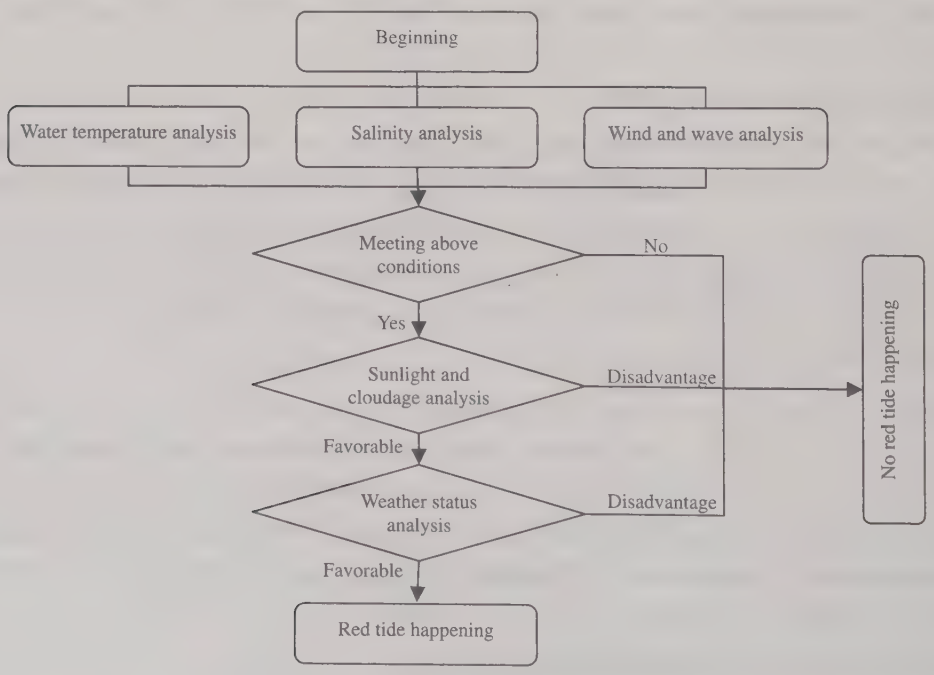

Fig.6 Flow chart of red tide forecast

5 Experiment and validation of forecast tools

By means of various tools, the forecast of red tide occurrence conditions was conducted from 2003 to 2004, and the result was satisfactory. The successful examples were the red tide conditions contrast between the forecast and what was actually happening in the year 2003. In the South China Sea, the eleven red tide events occurring in 2003 (fourteen events in total) were forecasted more precisely. As the observational and seasonal conditions are limited, the data obtained in the Hong Kong observatory network of red tide have been used to validate and supplement the forecast and observation.

Successful examples of the red tide forecast in 2003:

a) In the middle ten days of February, it was forecasted that abnormal phenomena in the waters would appear (A few red tides would take place) near the Pearl River Estuary; in fact, on Feb. 8, a red tide event occurred in the waters off Naozhou Island. The forecast delayed two or three days as compared with the fact.

b) In the last ten days of February, the waters off Guangxi was predicted to present abnormal phenomena; actually, on Feb. 24, the Zhuhai Marine Observatory reported a red tide with a large sea area occurring in the waters off the western side of Leizhou Peninsula. The forecast was precise.

c) In the first ten days of April, the marine environmental conditions were forecasted to be advantageous to the red tide algae growing from the Pearl River Estuary to West Guangdong coast; what was actually happening on Apr. 2, 7 and 8 was reported by the Hong Kong observatory network of red tide: red tide events were found in the Shenshui Bay, Baisha Bay of Xigong and Qianshui Bay individually. The prediction was right.

d) It was forecasted that there would be a red tide happening on the western side of the Pearl River Estuary in the last ten days of April; in fact, the Monitoring Center of Guangdong Marine and Fishery Administration reported on April 27 in the waters near Guishan and Jiouzhou Island off Zhuhai, a red tide event was found with a sea area of 350 km^2; on Apr. 29 the Zhuhai Marine Observatory reported a red tide with a large sea area occurring in the waters surrounding Wanshan Islands. The forecast was exact.

e) In the last ten days of May, the marine environmental conditions were predicted to be in favor of red tide algae reproduction from the Pearl River Estuary to East Guangdong coast; the fact was on May 25 a red tide event was discovered at the mouth of Jieshi Bay (22°7′N, 115°7′E); on May 27 another red tide event with a sea area of 15 km^2 was reported to happen from Shekou to Shenzhen Bay.

f) It was predicted, in the first ten days of Jun, a red tide would take place from the Pearl River Estuary to Shanwei coast; as a matter of fact, on Jun. 9 and 10 in the waters of Shenzhen Bay, Dongjiaotou Fishing Port, Zhaoshang Port, Mawan Port of SCT and Santudi of Shekou Port a red tide with a sea area of 41 km^2 was discovered. The prediction was right.

g) In the middle ten days of June, a red tide was forecasted to happen from the Pearl River Estuary to Daya Bay; in fact, on June 13 and 14 a red tide event with an area of 15 km^2 occurred in the waters

adjacent to Meishawan, Dameisha, Xiaomeisha, Yantian Fishing Port and Yantian Port. The forecast was precise.

h) It was forecasted, in the last ten days of June, a red tide would occur from the Pearl River Estuary to Shanwei coast; in fact, a red tide with a sea area of 20 km^2 took place on June 23-25 in the waters of Houhaiwan, Dongjiaotou Fishing Port, Zhaoshang Port and Santudi of Shekou Port. The prediction was right.

i) In the first ten days of August, the marine environmental conditions were predicted to be advantageous to the red tide organisms' blooming; what was actually happening was that a red tide was discovered in the waters of Daya Bay, Dongsheng mariculture farm and fishery administrative wharf of Aotou port. The forecast was exact.

j) In the middle ten days of August, the marine ambient from the Pearl River Estuary to East Guangdong coast was forecasted to be in favor of red tide algae growing; as a matter of fact, on Aug. 6-13 a red tide took place in the Dongsheng mariculture farm and fishery administrative wharf of Aotou. The prediction was right.

k) In the end of the first ten days of September, it was predicted that a small red tide would happen in some waters from the Pearl River Estuary to East Guangdong coast; in fact, on Sept. 8 a red tide occurred and faded away in the waters of Shatoujiao. Besides, on Sept. 10 a red tide event was discovered in an aquaculture farm of Shawan of Hong Kong. The red tide did not vanish on Sept. 11 as yet, and the forecast was precise.

According to the above exact forecast analysis of 11 red tide events, the forecast tools are feasible and accord with the judgment criterion of mid-range weather forecast specified by the State Meteorological Administration, though the predicted area is large and the duration is long. This is a great progress in the red tide forecast.

7 Conclusions and discussion

a) The weather circulation status is stable and lasts a long period of time in the prophase of red tide blooming.

b) The SST keeps stable with a daily variation of less than 1℃ in the prophase of red tide outbreak.

c) The wind speed is small and daily is less than force 4 on the average in the prophase of red tide blooming.

d) The weather is fine, or partly cloudy, with enough sunlight, or sweltering in the prophase of red tide outbreak.

The weather circulation status, hydrological and meteorological factors are chosen to forecast the red tide happening. The red tide sets used in the analysis occur in recent 20 years.It indicates as well that the variation of hydro-meteorological factors plays an important role in triggering the red tide occurrence. The statistical analysis shows the red tide will never take place under gale and rough sea conditions. The red tide will not happen in lower water temperature (less than 16℃) and higher water

temperature (higher than 30℃).

SST stability (quasi-normal temperature) and maintenance depend on the weather circulation's control of and impact on a certain region. Up to now, the 15-day atmospheric circulation prediction and 7-day hydro-meteorological factors prediction in future can be figured out by means of marine meteorological numerical forecast. Thus, the numerical model is a key to the mid-range forecast of red tides.

Red tide forecast is still a rising subject. At present, red tide monitoring and prediction are separated, and the definitions of red tide are not uniform. Red tide monitoring and prediction should be combined just like meteorology. Nowadays, at home and abroad there are no successful and professional forecast tools for red tide and there are a variety of different professional opinions on it. "In terms of hydro-meteorology, red tide happening can be predicted." The above examples show up clearly: making use of hydro-meteorological factors to forecast red tide happening is valid and accords with the judgment criterion of mid-range weather forecast. Hydrology and meteorology are full-grown disciplines, the weather of one week in future can be predicted by means of numerical forecast tools, and the biological and chemical factors are not full-grown to be used in the mid-range forecast of red tide. Different views and opinions are always allowed on the discussion of rising disciplines. The experts in different professions can understand each other, particularly those whose specialty are not prediction, should know the status of the development of marine meteorological forecast red tide prediction and forecast tools at home and abroad, as well as red tide forecast veracity. Only by comparing can one distinguish.

References

[1] Liang Song, Qian Honglin. Discuss of relationship between red tide occurrence frequency and monsoon transition period in the northern part of South China Sea. Red Tide Study of Guangdong Coast, 2002, 74-78.

[2] Huang Weigeng, Selected works of red tide monitoring and forecast. The Second Institute of Oceanography, SOA, 2000, 3.

[3] Liang Song, Qian Honglin, Huang Lixian. Red tide survey from Yantian of Dapeng Bay to Nan'ao coast. Red Tide Study of Guangdong Coast, 2002, 5-7.

[4] Lian Shuangxi. Concept of red tide monitoring and forecast. Marine Technology, 2002, 6 (2).

[5] Deng Song, Tang Chaolian, You Dawei. Discuss of abnormal high SST formation cause in the waters off Guangdong and Hong Kong in winter and spring of the year 1998. Marine Science Bulletin, 2005, (4): 17-21.

[6] Chao Chonghua et al. Analysis of red tide and environmental factors in Bayuquan of Liaodong Bay. Marine Forecast, 2005, (2): 1-5.

[7] Qiou Yibing et al. A case study of red tide formation cause in the western waters of Shenzhen in the year 1998. Collected Works of the South China Sea Resources and Environment Research, 1999, 236-242.

[8] Huang Chuguang et al. Study of Relationship between hydrological environment and red tide in East Guangdong waters in the year 1997. Collected Works of the South China Sea Resources and Environment

Research, 1999, 229-235.

[9] Zhang Shuijin, Yang Qingliang. Red tide and its prevention and cure countermeasures. 1994.

[10] Qian Honglin, Liang Song. Discuss of prevention and cure ways of red tide. Red Tide Study of Guangdong Coast, 2002, 110-114.

[11] Qi Yuzao, *et al*. Red tide and red tide study in China. Red Tide Study of Guangdong Coast, 2002, 14-20.

[12] Peng Kunlun et al. Cause discuss of red tide occurred in the western port waters of Shenzhen in the end of Apr 1996. Collected Works of the South China Sea Resources and Environment Research, 1999, 259-266.

[13] Qian Honglin et al. Red tide study of the Pearl River Estuary and its surrounding waters. Red Tide Study of Guangdong Coast, 2002, 39-44.

利用水文、气象要素因子的变化趋势预测南海区赤潮的发生

张俊峰[1]，白毅平[1]，俞建良[1]，庞海龙[1]，邓文君[1]，李华健[1]，吴迪生[1]，赵雪[1]，陈惠君[1]，蒋跃进[2]

（1. 国家海洋局南海预报中心,广东 广州 510300；2. 国家海洋局南海监测中心，广州 广州 510300）

摘 要：有些文献指出："赤潮发生起因因种而异，但大体上气候气象条件诸如温度、风力、风向，季风转换、气压等；海况、潮汐、流等以及海水的理化特征，如盐度、营养元素等，这些皆会成为某种赤潮爆发的因子或诱导因素[1]"。根据赤潮监控区监测资料分析：在南海赤潮多发区，海水富营养化条件已经具备，因此气象、水文要素条件就成为赤潮爆发的重要启动因子，而天气环流的维持与变化决定了气象、水文要素因子的稳定与变化，再根据赤潮生物培养试验，从初期繁殖到后期的爆发性繁殖，直至达到赤潮生物密度，这一过程一般都需要 4 ~ 5 d 的时间。针对这一现象，通过对近 10 a 的赤潮发生个例进行统计分析，统计其生成前期的天气环流形势和水文气象要素，分析出赤潮生成前期的环流模式和筛选出诱发赤潮爆发的重要因子，并依此来作为预报赤潮生成的方法，依照此方法对 2003 年的赤潮进行预报，其效果是另人满意的。

关键词：赤潮；气象条件；天气环流

Some Trials of Typical Typhoon Tracks Using the Adjoint Method

CAI Qifa (蔡其发)[1,2], HUANG Sixun (黄思训)[1], XIANG Jie (项杰)[1], LAN Weiren (兰伟仁)[2]
1. *Meteorological College, PLA University of Science and Technology, Nanjing* 211101, *Jangsu, China*
2. *Hydrometeorological Center of the Headquarters of General Staff, Beijing* 100081, *China*

Abstract: In this paper, the adjoint method is applied to the statistical-dynamic model (SD-90) for the prediction of typhoon tracks along with the regularization thinking and optimal control techniques. The adjoint model and the gradient of objective function are deduced with the continual model respectively. For 4 typical typhoons, the forces and the initial velocity can be retrieved well, and the tracks of these typhoons are accurately fitted for an appropriate regularization parameter and optimal control parameter.

Keywords: typhoon tracks; variational assimilation; regularization methods; optimal control

Introduction

Tropical cyclone (TC) motion is one of the two core problems (tracks and intensity) in TC dynamics and prediction. In this paper, we will discuss the problem about TC tracks. It is shown that, the motion of TC is mainly affected by the large scale atmospheric background fields (the leading current theory) [1], meantime, the reciprocity among large scale atmospheric background fields; the circulation and β plane cause the motion of TC to deflect the leading current (called the drift of β) [2]; In addition, the mesoscale system among TC and the nonsymmetrical structure of TC (including dynamical and theoretical aspects), topography and the dynamical characteristic of boundary layer also affect the motion of TC. The actual TC moves under the influence of these factors [3].

The adjoint method is applied to the statistical-dynamic model (SD-90) for the prediction of typhoon tracks along with the regularization thinking and optimal control techniques [4]. The adjoint model and the gradient of objective functional are deduced with the continual and discrete models respectively. For 4 typical typhoons, the forces and the initial velocity can be retrieved well, and the tracks of these typhoons are accurately fitted for an appropriate regularization parameter and optimal control parameter.

1 Theoretical aspects

The following presents the theoretical part of the application of the adjoint method to SD-90.

Received on April 11, 2006

For SD-90, a TC is regarded as a point vortex versus easterlies and westlies. On the β plane, the center of TC satisfies the ordinary differential equations as bellow [5]:

$$\begin{cases} \dfrac{dx}{dt} = u \\ \dfrac{dy}{dt} = v \\ \dfrac{du}{dt} = (f_0 + \beta y)\, v + F_x(t) \\ \dfrac{dv}{dt} = -(f_0 + \beta y)\, u + F_y(t) \\ x|_{t=0} = x_0, \quad y|_{t=0} = y_0, \quad u|_{t=0} = u_0, \quad v|_{t=0} = v_0 \end{cases} \tag{1}$$

where, $0 \le t \le T$, and (x, y), (u, v) represent the coordinates and velocity of TC respectively, f_0 is the Coriolis parameter on the original coordinates, $F_x(t)$, $F_y(t)$ is the force exerted on the TC excluding the Coriolis force $(f_0 + \beta y)$.

Suppose that over the time $0 \le t \le T$, the observational TC track is $X = X_{obs}(t)$, $Y = Y_{obs}(t)$. Now, the goal is to determine the optimal initial velocity u_0, v_0 and forces $F_x(t)$, $F_y(t)$, such that the corresponding solution $x(t), y(t), u(t), v(t)$ of Eq.(1) minimizes the objective function:

$$J[u_0, v_0, F_x(t), F_y(t)] = \frac{1}{2}\int_0^T [(x(t) - X_{obs}(t))^2 + (y(t) - Y_{obs}(t))^2]dt \tag{2}$$

It can be seen that the solution $u_0(t), v_0(t), f_x(t), f_y(t)$ is possibly not unique (in fact, it is an inverse problem to determine $u_0(t), v_0(t), f_x(t), f_y(t)$). In order to obtain a unique physical solution, motivated by the thinking behind regularization, a stable function is added to J so as to keep the solution unique, to speed up convergence of the solution, and to reduce numerical oscillations in the iterative process. In the meantime, motivated by the theory of optimal control, a terminal control term is also added to J so that the fitted track (namely $x(t), y(t)$) and the observational TC track (namely $X_{obs}(t)$, $Y_{obs}(t)$) are kept as close as possible to each other at the terminal. Therefore, the new functional (still denoted by J conventionally):

$$\begin{aligned} J[u_0, v_0, F_x(t), F_y(t)] = {} & \frac{1}{2}\int_0^T [(x(t) - X_{obs}(t))^2 + (y(t) - Y_{obs}(t))^2]dt + \frac{\gamma_1}{2}\int_0^T [u^2 + v^2]dt \\ & + \frac{\gamma_2}{2}\int_0^T [(\frac{du}{dt})^2 + (\frac{dv}{dt})^2]dt + \delta[(x(T) - X_{obs}(T))^2 + (y(T) - Y_{obs}(T))^2] \end{aligned} \tag{3}$$

where γ_1, γ_2 are the regularization parameters respectively, and δ is the restraint parameter at the terminal corresponding to the optimal method.

After determining the optimal initial velocity u_0, v_0 and force added to TC $F_x(t)$, $F_y(t)$, the position and velocity of TC can be obtained using Eq.(1).

The adjoint equations and their initial conditions can be obtained after a series of processes [6]:

$$\begin{cases} -\frac{d}{dt}P = x(t) - X_{obs} \\ -\frac{d}{dt}Q - \beta(vR - uS) = y(t) - Y_{obs} \\ -\frac{d}{dt}R - P + (f_0 + \beta y)S = \gamma_1 u - \gamma_2 \frac{d^2u}{dt^2} \\ -\frac{d}{dt}S - Q - (f_0 + \beta y)R = \gamma_1 v - \gamma_2 \frac{d^2v}{dt^2} \\ P(T) = \delta(x(T) - X_{obs}(T)), Q(T) = \delta(y(T) - Y_{obs}(T)) \\ R(T) = \gamma_2 u \left.\frac{du}{dt}\right|_{t=T}, S(T) = \gamma_2 v \left.\frac{dv}{dt}\right|_{t=T} \end{cases} \quad (4)$$

The gradients of objective function versus $u_0, v_0, F_x(t), F_y(t)$ are:

$$\nabla_{u_0} J = R(0) - \gamma_2 \left.\frac{du}{dt}\right|_{t=0}, \nabla_{v_0} J = S(0) - \gamma_2 \left.\frac{dv}{dt}\right|_{t=0} \quad (5)$$
$$\nabla_{F_x} J = R(t), \nabla_{F_y} J = S(t)$$

Taking $R = (R_1, R_2, R_3, R_4) = (u_0, v_0, F_x(t), F_y(t))$, the descent algorithm can be expressed as follows

$$R_j^{i+1} = R_j^i - \nabla_{R_j} J\big|_{R^i} \cdot \rho_j^{i+1} \quad (6)$$

the optimal parameters can be obtained [8]. Here $i = 0$ represents the initial guess value, and ρ_j^{i+1}, $(j = 1, 2, 3, 4)$ is the iterative step for Step I.

On the whole, the following five steps must be followed to apply the adjoint method to the simulation of TC track:

a) Supply the initial guess value of the retrieved variables $u_0, v_0, F_x(t), F_y(t)$.

b) Integerating Eq.(1) using the initial value $u_0, v_0, F_x(t), F_y(t)$,obtain and store the values of $x(t), y(t), u(t), v(t), F_x(t), F_y(t)$.

c) Using $x(t), y(t), u(t), v(t)$ and the X_{obs}, Y_{obs},intenerate Eq.(4) and obtain the value of adjoint variable $P(t), Q(t), R(t), S(t)$.

d) Calculate the gradient of the objective function using Eq.(5) and the objective function using Eq.(3).

e) Update the value of $u_0, v_0, F_x(t), F_y(t)$ using Eq.(6). If the final condition is satisfied, e.g., the objective function reaches the given precision or the maximum given search steps are exceeded, then stop the program, otherwise rerun the program from the step 2,the new iteration will be executed using the updated $u_0, v_0, F_x(t), F_y(t)$.

2 Numerical trials

In this section, four typical TC tracks occurring in the Northwest Pacific Ocean are chosen. These tracks are obtained through 3-hour satellite positioning. By using the adjoint method, the initial velocity and forces exerted on TCs are retrieved, and the tracks are fitted. The characteristics of the four TCs are

exhibited in Table 1. The validity of the adjoint method with regularization thinking and control technique to simulate TC track and the influence of different combination of parameters (the regularizational parameter and the terminal optimal parameter) imposed to the precision of TC tracks simulation are checked on the one hand, and the analysis of the evolvement of forces for different TC track is applied on the other hand, which can offer new thought to TC track forecasting. The descent algorithm used in the trials is M1qn3 [7].

Tab. 1 The characteristics of the four TCs

TC	Occurrence	Initial position	Terminal position	Track description
9804	2000 UTC 25 Aug - 1400 UTC 7 Sept	24.1N, 132.9E	48.1N, 166.0E	Snake-tread
9806	2000 UTC 16 Sept - 1200 UTC 20 Sept	21.2N, 132.8E	29.5N, 120.9E	Northeastward to Westward
9807	1400 UTC 18 Sept - 0200 UTC 23 Sept	16.1N, 118.8E	41.8N, 143.5E	Northeastward
0004	0800 UTC 6 July - 0800 UTC 11 July	19.6N, 119.9E	38.3N, 123.7E	Turning on midway

2.1 Influence of different combinations of parameters on the precision of TC track simulation

In this section, the TC 9804 is illustrated to check the influence of different combinations of parameters on the simulation precision. The combination (a) is defined as $\gamma_1 = 0, \gamma_2 = 0, \delta = 0$ (which represents the condition that neither regularization nor optimal control is added to the process of simulation), and the combination (b) is defined as $\gamma_1 = 1e-3, \gamma_2 = 1e-3, \delta = 3dt$ (which represent the condition that the regularization and optimal control with a reasonable value is applied to the simulation of TC track), where dt denotes the step length of integration. Fig. 1 and 2 illustrate the effect of different combinations. It can be shown that different combinations of parameters will obtain different retrieved results of initial velocity and forces exerted on TC, and the precision of simulation of the TC tracks using the above results is also different. Furthermore, the descent speed of objective function is distinct. From the two figures, we can conclude that the combination (b) which added the regularization and optimal control to the TC track simulation surpasses the combination (a), so the trials bellow will use the combination (b) to simulate the TC track.

2.2 The analysis of retrieved result

The deviation of the retrieved result versus observation value is shown in Table 2, where 9804 (a) represents the result of simulation using parameters combination (a) and 9804(b) denotes the result of simulation using the combination (b).We can further check the excellent result of combination (b) using the regularization and optimal control method. For the evolution of force exerted on the TC, Figures 3-5 show that F_x, F_y appear an antiphase change at the turning point and a similar phase change on the other points, and the intension of F_x, F_y is weak relatively at the turning point.

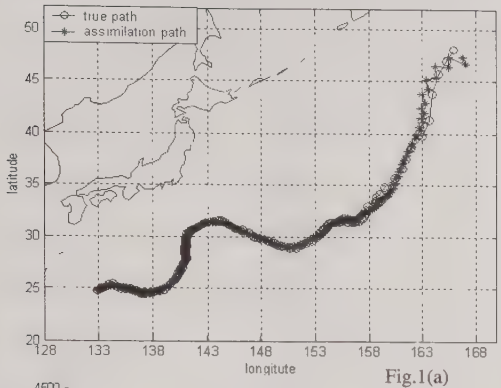

Fig.1(a)

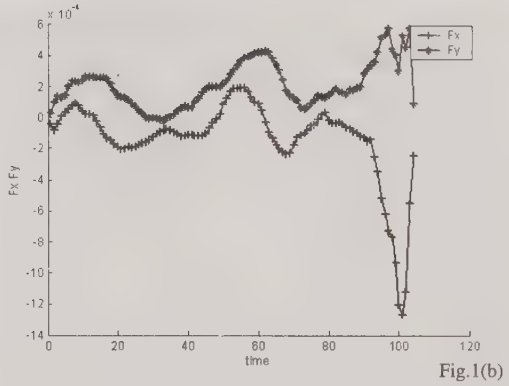

Fig.1(b)

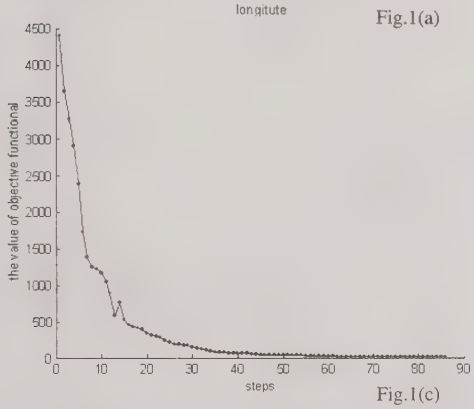

Fig.1(c)

Fig.1 TC 9804 with the combination (a)

(a)The fitted and real track where * represents the fitted value and "o" denotes the observational value; (b)The retrieved F_x, F_y; (c)The descent trend of objective versus iteration

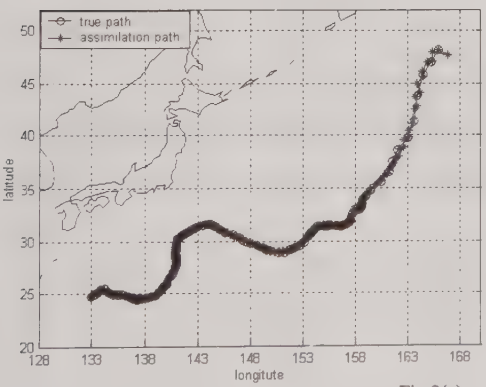

Fig.2(a)

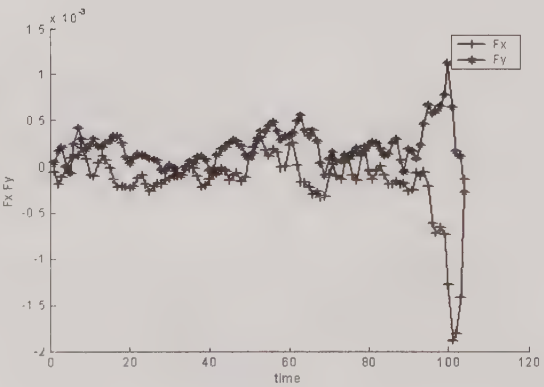

Fig.2(b)

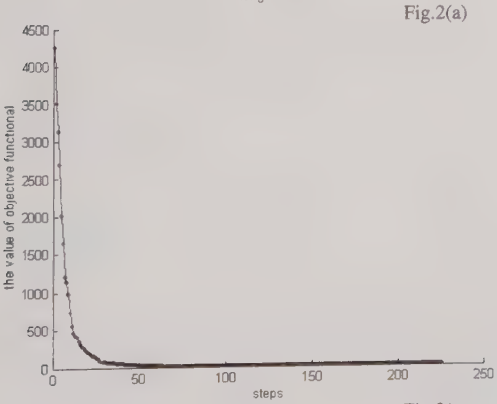

Fig.2(c)

Fig.2 TC 9804 with the combination (b)

(a)The fitted and real track where * represents the fitted value and "o" denotes the observational value; (b)The retrieved F_x, F_y; (c)The descent trend of objective versus iteration

Tab. 2 The deviation of the simulation for the four TCs (Unit: deg)

TC	Meridional Mean square deviation	Meridional Maximum square deviation	Zonal Mean square deviation	Zonal Maximum square deviation
9804 (a)	0.069	0.256	0.065	0.204
9804 (b)	0.054	0.222	0.051	0.184
9806	0.011	0.020	0.012	0.025
9807	0.020	0.064	0.021	0.039
0004	0.010	0.015	0.010	0.023

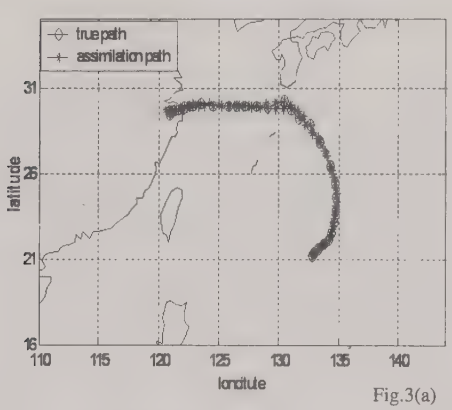

Fig.3(a)

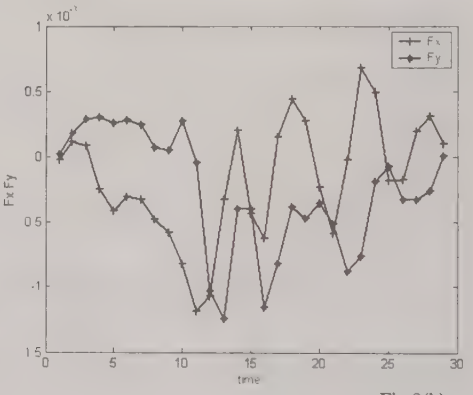

Fig.3(b)

Fig.3 TC 9806 with the combination (b)

(a) The fitted and real track where * represents the fitted value and "o" denotes the observational value;

(b) The retrieved F_x, F_y

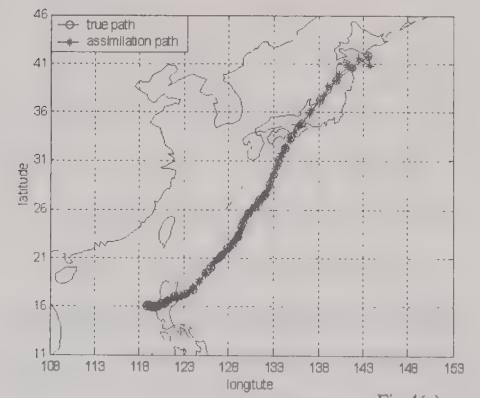

Fig.4(a)

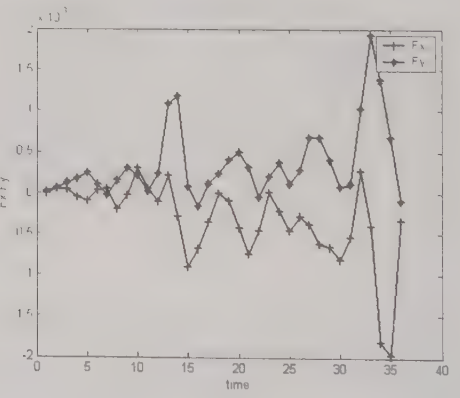

Fig.4(b)

Fig.4 TC 9807 with the combination (b)

(a) The fitted and real track where * represents the fitted value and "o" denotes the observational value;

(b) The retrieved F_x, F_y;

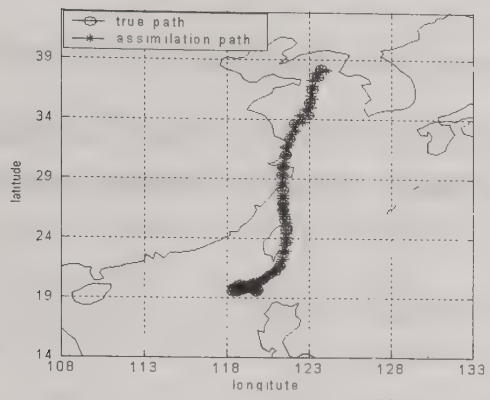

Fig.5(a)

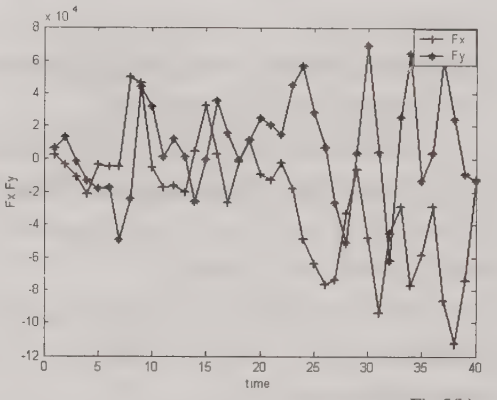

Fig.5(b)

Fig.5 TC 0004 with the combination (b)

(a) The fitted and real track where * represents the fitted value and "o" denotes the observational value;

(b) The retrieved F_x, F_y;

3 Conclusion and discussion

In this paper, an adjoint method with regularization and optimal control method is carried out for four real TC tracks, and the model used is the statistical-dynamical prediction model SD-90. The result indicates that, although the TC motions are very complicated, the TC tracks can be fitted well using the adjoint method. And TC 9804 is applied to check the validity and precision with two different combinations of parameters, and the method using regularization and optimal control method shows a better result than the method using neither regularization nor optimal control thinking. With a simpler model, litter input data and high precision of simulation, the method shows its merit in the simulation of TC track.

The SD-90 is now in use in the operational TC prediction. Since the force F_x, F_y exerted on TC is determined according to the statistical regression method in SD-90, theoretically, the present method for determining force should be superior to the statistical regression method, as is shown above by the numerical results. For instance, the force appears an antiphase change and the intension of F_x, F_y is weak relatively at the turning point. This is now under research.

Acknowledgements

The National Nature Science Foundation of China under Grant No. 90411006 supported this work simultaneously.

References

[1] Wang Bin et al. The progress in dynamics of typhoon track research. China atmospheric science, 1998, 25:

420-432.

[2] Chen Lianshou, Meng Zhiyong. The ten-year progress of tropical cyclone research in our country. China atmospheric science, 2001, 25: 420-432.

[3] Chen Lianshou, Ding Yihui. The western Pacific typhoon conspectus. Beijing: China science press, 1979, 491.

[4] Huang Sixun, Han Wei,and Wu Rongsheng. Theoretical analyses and numerical experiments of variational assimilation for one-dimension ocean temperature model with techniques in inverse problems. Science in china(D), 2004, 47(7): 630-638.

[5] Niu Xuexin. The dynamics of typhoon.Beijing:China meteorological press,1992.

[6] Huang Sixun, and Wu Rongsheng. Methods of mathematical physics in atmospheric science. Beijing: China meteorological press, 2001.

[7] GILBERT J C and LEMARECHAL C. Some numerical experiments with variable storage quasi-Newton algorithms. Math. Programming, 1990, B45: 407-435.

几个典型台风路径的同化试验

蔡其发[1, 2]，黄思训[1]，项杰[1]，兰伟仁[2]

（1. 解放军理工大学气象学院，江苏 南京 211101；2. 总参气象水文中心，北京 100081）

摘 要：从上海台风所的台风路径统计动力预报模型SD－90出发，利用变分同化方法结合反问题正则化思想和最优控制技巧（而非统计方法），反演出台风所受到的除科氏力以外所有力的合力及台风的初始速度，用实际台风定位资料分析不同的正则化参数及最优控制参数的组合对同化结果的影响，分析不同路径特征台风路径的拟合效果。该方法具有模式简单、应用资料少、拟合精度高等优点，为台风路径的预报提供了新的思路。

关键词：台风路径；变分同化；正则化方法；最优控制

The Catch Distribution of *Ommastrephes batramii* in Squid Jigging Fishery and the Relationship between Fishing Ground and SST in the North Pacific Ocean in 2004

CHEN Xinjun (陈新军), LIU Bilin (刘必林)
Ocean College of Shanghai Fisheries University, Shanghai 200090, *China*

Abstract: Neon flying squid *Ommastrephes batramii* is widely distributed in the North Pacific Ocean, which has become the main fishing species for Chinese squid jigging fleets since 1993. Many authors have made the studies on the fields of fishing ground and its environment conditions. However, the squid catch per fishing vessel attained the highest level of about 550 t in 2004. In this paper, the catch and its distribution in 2004 would be compared with the previous year. Based on the catch data from Chinese squid jigging vessels and sea surface temperature with the format of 1°latitude by 1°longitude from May to November in 2004, the distribution maps were drawn by Marine explorer 4.0. The results show that the production in the east waters to 160°E was low during May and July. During October and November, the production in the waters from 150°E to 160°E was relatively higher, which occupied 62.5 percent of the total catch. During November, the production in the west waters to 150°E was also low. The highest CPUE area located in the west waters to 150°E, the next was the area from 150°E to 160°E and the lowest CPUE area located in the east waters to 160°E. The SST in the fishing ground seems to change seasonally. The suitable SST for each month is as follows: 12-14 ℃ in May, 15 ℃ - 16 ℃ in June, 14 ℃ - 16 ℃ in July, 18 ℃ - 19 ℃ in August, 16 ℃ -17 ℃ in September, 15 ℃- 16 ℃ in October and 12 ℃ - 13 ℃ in November. The result of K-S test shows that the above monthly suitable SST is considered as the indicator of looking for the main fishing ground.

Keywords: Ommastrephes batramii; North Pacific; Catch distribution; Sea surface temperature; K-S test

Introduction

Neon flying squid *Ommastrephes batramii* is one of the mainly economic cephalopods in the North Pacific, which is widely distributed in the ocean [1].The main fishing ground located in the areas where Kuroshio current and Oyashio current blend and the area extending towards east in the subarctic frontal zone of the central North Pacific Ocean. It is showed that the distribution and formation of fishing ground and squid migration are closely related with the oceanic environment, especially for the

Received on April 3, 2006

development and falling of both Kuroshio and Oyashio currents [3]. Exploiting the oceanic squid *Ommastrephes batramii* in the North Pacific began in 1993 in China. Since then the fishery has improved greatly, the number of fishing vessels has increased to over four hundred and the total catch per year has attained 110 000 t which possessed 12 percent of the total in the Chinese distant-water fishery [2, 4, 5].

There are many papers published about the relationship between the fishing ground and oceanic environment, Yatsu et al [6], Chen X J [3, 7-8], Gao C Y [9], Ding Y M [10], Shen H M [11], Shen X Q et al [12], Yatsu A [13], Murata et al [14] and Wang W Y et al [15] have got some results. In 2004, the catch of squid from Chinese jigging vessels attained the highest point of more than 500 t, so the reason is needed to be discussed. In this paper, we will analyze the catch distribution and its relationship with SST and discuss the variation of fishing ground based on the catch data from Chinese squid jigging vessels, which will present some reference for fishing and reasonably utilizing the squid in the future.

1 Materials and methods

1.1 Materials

The production data for squid jigging fishery in the North Pacific Ocean during May to November in 2004 come from the jigging fishing technology group of Shanghai Fisheries University, which contains operating date, fishing position and production. The dataset of SST with 1° latitude by 1° longitude is downloaded from http://iridl.ldeo. columbia.edu [16].

1.2 Methods

1.2.1 Data processing

The data of production are prepared by the form of 1° latitude by 1° longitude, and calculated by month. The CPUE is expressed as follows:

$$\mathrm{CPUE} = C / F$$

where, C is the total production in one grid, unit: t; F is the fishing times in one grid, unit: days; CPUE is the catch per day, unit: $t \cdot d^{-1}$.

1.2.2 Data analysis

Distributions of production, CPUE and SST are drawn by the GIS software Marine explore 4.0, which is to analyze the spatial production and its relationship with SST.

Based on the non-parameter Statistic (Kolmogorov-Smirnov) method [17-19], the remarkable test on the relationship among production, CPUE and SST is made. The formula of K-S test is as follows:

$$f(t) = \frac{1}{n}\sum_{i=1}^{n} l(x_i) \quad ; \quad g(t) = \frac{1}{n}\sum_{i=1}^{n} \frac{y_i}{\bar{y}} l(x_i) \quad ; \quad D = \max\left|g(t) - f(t)\right|$$

where, n is the number of samples; t is the value of SST which has been grouped (the grouped gap is 0.5 ℃); x_i is the observed value of SST in the i month; y_i is the CPUE in the i month; $\bar{y}$ is the average

value of total monthly CPUE; $l(x_i)$: if $x_i \leq t$, $l(x_i)$ is equal to 1; otherwise $l(x_i) = 0$.

2 Results

2.1 Monthly distribution of production and CPUE

Based on the statistics in Tab.1, there are 68,103 t in the total production with 21 261 fishing times and 3.2 $t \cdot d^{-1}$ for CPUE from May to November. Monthly production was over 10 000 t from August to November, which occupied 81.1 percent of the total, while the fishing times only occupied 64.1 percent and its CPUE on the average was about 2.9-5.0 $t \cdot d^{-1}$. From May to July, there was 18.9 percent of the total production and 35.9 percent of the total fishing times, and the average CPUE was below 2 $t \cdot d^{-1}$.

Tab.1 The fishing times, catch and CPUE for Chinese squid jigging boats from May to November in 2004

Month	Fishing times / time	Production / t	Production per day / $t \cdot d^{-1}$
May	710	1176	1.7
June	3540	5474	1.5
July	3379	6244	1.8
August	3829	19197	5.0
September	3594	13258	3.7
October	3520	10125	2.9
November	2689	12629	4.7

2.2 Spatial distribution of production and CPUE and its relationship with SST

The squid fishing vessels from May to November were distributed in the areas of 143° - 180° E and 38° - 46° N, and most of the production was located in the waters west of 150° E and the waters from 150° to 160° E. In May, the main fishing grounds were located in the areas from 175° to 180° E and from 38° to 40° N, in which the suitable SST was 12 ℃ - 14 ℃ and the production was less than 2 000 t (Fig.1). In June, the main fishing grounds were from 169° to 178° E and from 38° to 42° N with a suitable SST of 15 ℃ - 16℃, and the production for some fishing areas was more than 2 000 t (Fig.1). In July, the fishing grounds were scattered in the areas from 175° to 180° E and from 38° to 40° N with the production less than 2 000 t (Fig.1). In August, the fishing grounds were located in the areas from 152° to 180° E and from 39° to 43° N with a suitable SST from 15 ℃ to 16 ℃, and for some fishing areas the production was more than 6 000 t (Fig.1). In September, the fishing grounds were distributed in the areas from 152° to 180° E and from 39° to 43° N with a suitable SST of 16 ℃ - 17 ℃, and the productions for some fishing waters are between 2 000 and 4 000 t (Fig.1). In October, the fishing grounds were located in the areas from 147° to 160° E and from 39° to 44° N, in which the suitable SST was 15 ℃ - 16 ℃ and the productions for some fishing areas were between 2 000 and 4 000 t (Fig.1). In November, the fishing grounds were distributed in the areas from 146° - 150° E and

from 39° - 42° N, in which the suitable SST was 12 ℃ - 13 ℃ and the productions for some fishing areas were more than 8 000 t (Fig.1).

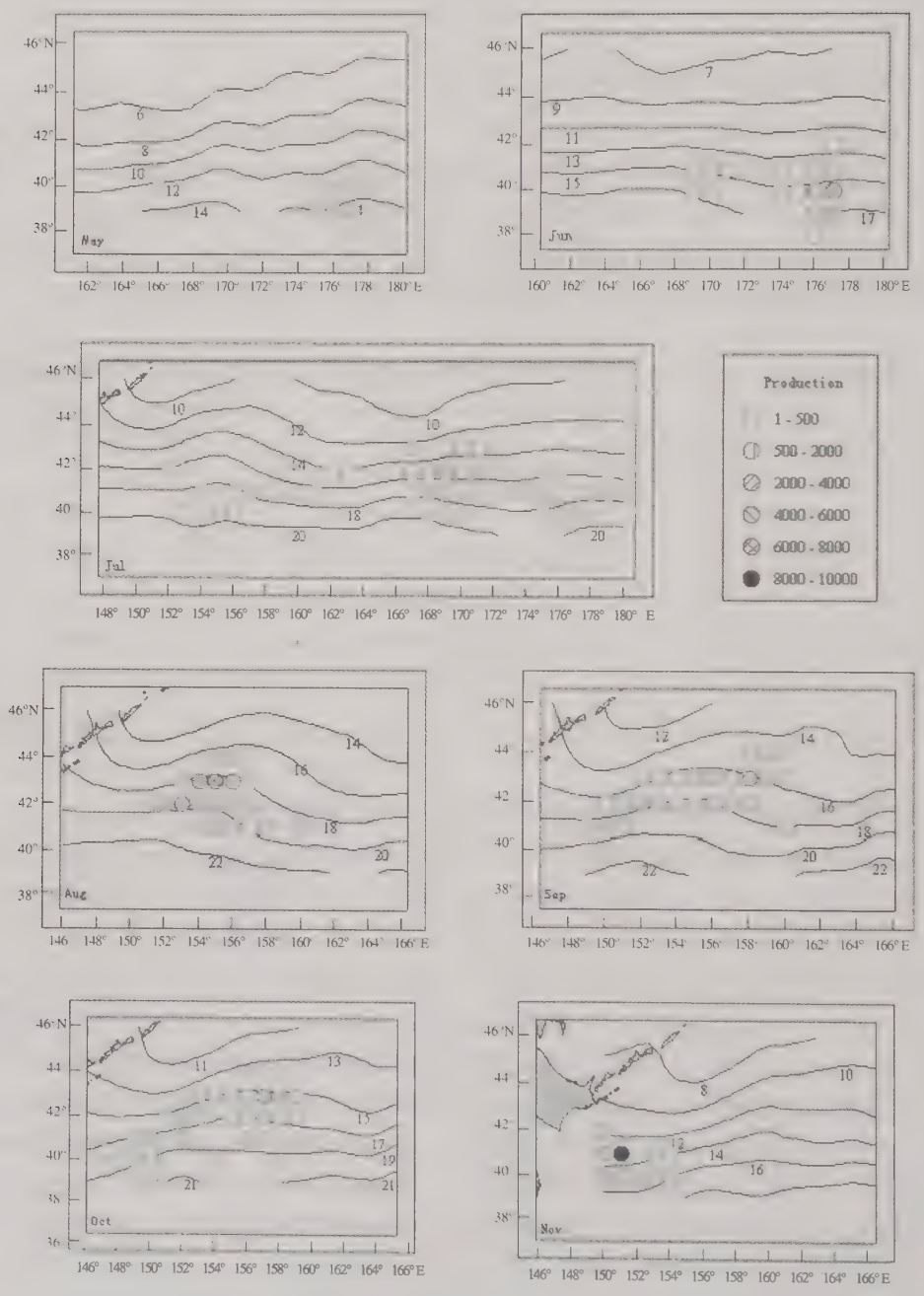

Fig.1 The catch distribution and its relationship with sea surface temperature

As a result, from May to July, the fishing grounds were located in the waters east of 160° E but the production was lower. From August, the fishing ground was transferred to the waters from150° to 160°

E, and most of the production was located in the waters 153° - 155° E and 42° - 43° N. From September to October, the fishing ground was around the waters of 157° - 158° E and 43° N. In November, the fishing areas were located in the Japanese EEZ and the higher production is distributed in the waters around 146° E and 41° N.

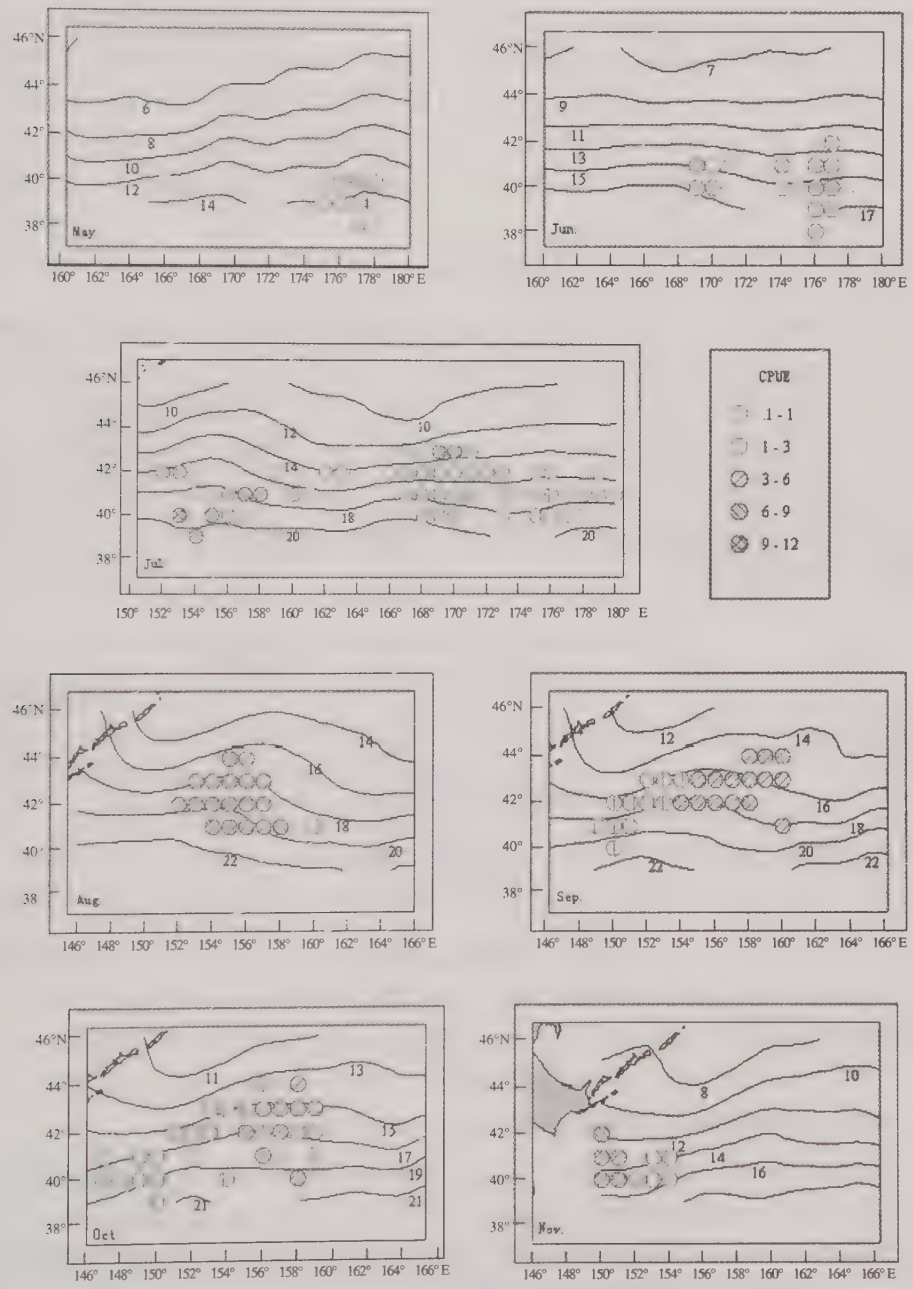

Fig.2 The CPUE distribution and its relationship with sea surface temperature

Based on the spatial distribution of CPUE, the value of CPUE was lower from May to June which was below 3 $t \cdot d^{-1}$ (Fig.2). In July, the higher CPUE was located in the waters of 152° - 158° E and 39° - 42° N, in which the CPUE around the waters 153° E and 40°N with a SST of 19 ℃ - 20 ℃ was more than 9 $t \cdot d^{-1}$. The next is distributed in the waters 152° - 153° E and 42° N with a SST of 16 ℃ – 17 ℃ and the CPUE was from 6 to 9 $t \cdot d^{-1}$ (Fig.2). In August, the area with the CPUE from 6 to 9 $t \cdot d^{-1}$ was located in the waters of 153° E and 43° N, 154° E and 42° N, 158° E and 41° N, in which the SST was 17 ℃ - 20 ℃ (Fig.2). In September, the higher CPUE between 3 and 6 $t \cdot d^{-1}$ was located in the waters of 154° - 160° E and 42° - 44° N, in which the SST was 15 ℃ - 18 ℃ (Fig.2). In October, the higher CPUE from 3 to 6 $t \cdot d^{-1}$ was located in the waters of 155° - 159° E and 42° - 44° N with a SST of 15 ℃ – 18 ℃ (Fig.2). In November, the highest CPUE over 9 $t \cdot d^{-1}$ was located around the waters of 146° E and 42° N, in which the SST was 11 ℃ - 12 ℃ (Fig.2).

2.3 Suitable SST in the fishing ground and K-S test

Based on the relationship among production distribution, CPUE and SST, the monthly suitable SST of fishing ground was as follows: 12 ℃ - 14 ℃ in May, 15 ℃ - 16 ℃ in June, 14 ℃ - 16 ℃ in July, 18 ℃ - 19 ℃ in August, 16 ℃ - 17 ℃ in September, 15 ℃ - 16 ℃ in October and 12 ℃ - 13 ℃ in November. The analysis of relationship of CPUE and SST from May to November by K-S test was made, and the value $D = 0.050203 < P(\alpha/2) = 0.1278$ ($\alpha=0.05$). The result of K-S test shows that the difference between sea temperature and CPUE is not remarkable; the SST range of fishing ground for each month is suitable (Fig.3).

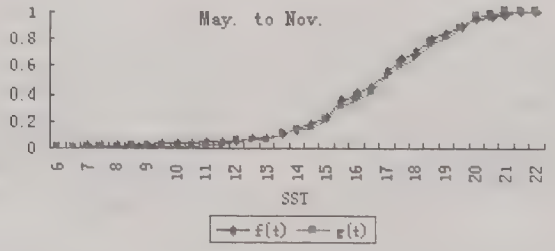

Fig.3 The figure of K-S test

3 Discussion

3.1 Production distribution in 2004 and comparison with the previous years

The production per squid fishing vessel was over 500 t in 2004, which was the highest level since 1993. But the catch varied with different fishing waters. Based on the spatial distribution of production (Tab.2), the majority of the catch which possessed 64.66 percent was located in the waters of 150° E - 160° E. The next fishing area occupying 17.71 percent of the total catch was distributed in the waters west of 150° E. The last fishing area was distributed in the waters of 170° E - 180° E and 160° E - 170°

E, which possessed 9.55 and 8.09 percent respectively. Compared with the previous yeas, the production ratio was variable in different waters, while in recent years the waters of 150° E - 160° E was the main traditional fishing ground.

Tab.2 The catch percentage in different fishing areas for Chinese squid jigging boats from 1995 to 2004

Fishery area	1995	1996	1997	1998	1999	2000	2001	2002	2003	2004
West of 150°E	95.92	53.66	60.45	34.21	31.00	14.06	20.19	18.57	15.13	17.71
150°-160°E	3.54	46.33	34.90	48.92	34.94	49.24	61.61	41.51	66.39	64.66
160°-170°E	0.53	0.00	4.63	14.37	26.09	20.61	9.28	24.63	4.12	8.09
170°-180°E	0.00	0	0.01	2.50	2.02	7.6	5.45	4.90	8.06	9.55
East of 180°W	0	0	0	0	4.68	8.47	3.47	10.40	6.31	0.00

3.2 Analyzing the cause of the highest production per fishing vessel in 2004

Based on the SST distributions and SST anomaly from May to November in 2004 [16], the highest production per fishing vessel is due to the fact that the SST is 1 - 2 degrees Centigrade higher than the normal year in the main fishing grounds between 150° E and 160° E, thus being favorable to the growth of squid. In addition, the number of Chinese squid fishing vessels in the North Pacific Ocean fell from more than 400 boats in 2001 to about 210 boats in 2004, so the interference among fishing vessels was reduced.

3.3 Analysis on the relationship between fishing ground and SST

Generally the SST is regarded as one of the most common indicators for looking for the fishing ground. Based on the monthly production, CPUE and SST distribution maps, the suitable SST in the main fishing ground was as follows: 12 ℃ - 14 ℃ in May, 15 ℃ - 16 ℃ in June, 14 ℃ - 16 ℃ in July, 18 ℃ - 19 ℃ in August, 16 ℃ - 17 ℃ in September, 15 ℃ - 16 ℃ in October and 12 ℃ - 13 ℃ in November. During May and August, the suitable SST rises gradually, but during August and November the suitable SST falls by month, which is the same as other results [7-15, 20].

3.4 Research in the future

Because the data and the materials are limited, the study is made only from analyzing the production distribution and its relationship with SST, not including other environmental data such as salinity, chlorophyll and plankton, which needed to be studied furthermore.

Acknowledgements

The paper is sponsored by the Shanghai Morning-Star Program (Serial Number 02QC14040) and supported by the Shanghai Leading Academic Discipline Project (Project Number T1101).

References

[1] Dong Z Z. Biology of ocean economic cephalopod in the world [M]. Jinan: Shandong Science Technology Press. 1991, 82-86

[2] Cheng J H, Huang H L. Relationship between environment characters and *Ommastrephes bartramii* fishing ground in the North Pacific [J]. Journal of Fishery Sciences of China. 2003, 10(6): 507-512.

[3] Chen X J. An analysis on marine environment factors of fishing ground of *Ommastrephes bratramii* in northwestern Pacific [J]. Journal of Shanghai Fishery University, 1997, 6(4): 263-267.

[4] Wang Y G, Chen X J. The current exploitation of cephalopod resources in the world and the development of Chinese distant-water squid jigging fishery [J]. Journal of Shanghai Fishery University, 1998, 7(4): 275-278.

[5] Shao Q Q, Rong K, Ma W W. et al. Study on spatial patterns of *Ommastrephes Bartramii* fishing ground in the Northwest Pacific Ocean [J]. Geographical Research.2004, 23(1):1-9.

[6] Yatsu A, Midorikawa S, Shimada T. et. al. Age and growth of the neon flying squid, *Ommastrephes batramii*, in the North Pacific Ocean [J]. Fish Res. 1997, 29:257-270.

[7] Chen X J. Study on the relationship between fishing ground of *Ommastrephes batramii* and SST in the Northwestern pacific [J]. Journal of Shanghai Fishery University, 1995, 4(3):181-185.

[8] Chen X J. The preliminary study on fishing ground of large-sized *Ommastrephes batramii* in North pacific waters between 150°E and 170°E[J]. Journal of Shanghai Fishery University, 1999, 8(3): 197-201.

[9] Gao C Y. The relationship between Chinese squid fishing ground and marine environment in the Japan Sea and Northwestern Pacific Ocean [J]. Distant-water Fisheries.1996, (3):11-17.

[10] Ding Y M. Study on the exploitation of *Ommastrephes batramii* in North Pacific Ocean [J]. Distant-water Fisheries.1998, (4):41-44.

[11] Shen W M. The report of sea condition in the squid fishing ground of North Pacific during June and December in 1999 [J]. Distant-water Fisheries.2000, (3):15-18.

[12] Sheng X Q, Fang W, Cui X S. Study on the relationship of fishing ground distribution of *Ommastrephes bartrami* and water temperature in the Northwest Pacific Ocean [J]. Marine Fisheries Research. 2004, 25(3): 10-14.

[13] Yatsu A. Distribution of flying squid, *Ommastrephes bartramii*, in the North Pacific based on a jigging survey, 1976~1983[R]. Bull. Natl. Res. Inst. Far Seas Fish. 1992, 29: 13-37.

[14] Mamoru M. The resources of marine pelagic species, *Ommastrephes Bartramii* [J]. Bull, 1989, (1):72-75.

[15] Wang W Y, Shao Q Q, Xue Y C, et al. On the Relationship Between the Resources of *Ommastrephes Bartramii* and Marine Environment in the Northwest Pacific Ocean Based on GIS [J]. Geo-information Science. 2003, (1): 39-44.

[16] http://iridl.ldeo.columbia.edu/SOURCES/.IGOSS/.data_products.html. 2005-02-16.

[17] Perry R I, Smith S J. Identifying habitat associations of the marine fishes using survey data: an application to the northwest Atlantic [J]. Can J Fish Aquat. Sci., 1994. 51:589-602.

[18] Yan Y Z. Business statistics [M].Taibei: Sanming Book Press. 1985,787.

[19] Wei J X. Basis of mathematical statistics and its application [M]. Chengdu: Sichuan University Press.1991, 184-185.

[20] Chen X J, Tian S Q. Analysis on the fishing ground of *Ommastrephes bartramii* in the Northwestern Pacific Ocean [J]. Fishery Modernization, 2001, 3: 3-6.

2004 年北太平洋柔鱼钓产量分析及作业渔场与表温的关系

陈新军，刘必林

（上海水产大学海洋学院，上海 200090）

摘 要：根据 2004 年 5 — 11 月我国鱿钓船在北太平洋生产数据，结合表温资料，按经纬度 1° ×1° 的格式，利用 Marine explorer 4.0 软件作图进行分析。结果表明，5 — 7 月在 160° E 以东海域作业，产量较低；8 — 10 月在 150° — 160° E 海域作业，为生产作业的产量高峰期，占总产量的 62.5%；11 月在 150° E 以西海域作业，产量也较低。在 150° E 以西海域 CPUE 最高，150° —160° E 中部海域次之，160° E 以东海域最低。作业渔场的适宜表温呈现出季节性变化。各月适宜表温分别为：5 月 12 ℃ ～ 14 ℃；6 月 15 ℃ ～ 16 ℃；7 月 14 ℃ ～ 16 ℃；8 月 18 ℃ ～ 19 ℃；9 月 16 ℃ ～ 17 ℃；10 月 15 ℃ ～ 16 ℃；11 月 12 ℃ ～ 13 ℃。K-S 检验表明，上述表温可作为寻找中心渔场的指标。

关键词：柔鱼；北太平洋；产量分布；表温；K-S 检验

Metabolites of Marine-derived Mangrove Endophytic Fungus #2492 from the South China Sea

ZHU Feng (朱峰)[1,2], LIN Yongcheng (林永成)[2], Wang Jun (王军)[3], ZHOU Shining (周世宁)[3], VRIJMOED L L P[4]

1. *Department of Chemistry & Chemical Engineering, Foshan University, Foshan* 528000, *Guangdong, China;*

2. *School of Chemistry & Chemical Engineering, Zhongshan University, Guangzhou* 510275, *Guangdong, China;*

3. *School of Pharmaceutical Science, Zhongshan University, Guangzhou* 510080, *Guangdong, China*

4. *Department of Biology & Chemistry, City University of Hong Kong, Hong Kong, China*

Abstract: Two metabolites (A and B) were isolated from the mycelium of mangrove endophytic fungus Stysanus like sp. (#2492) from the South China Sea. Their structures were identified by spectral data as N-(2-hydroxytetracosyl)-2-amino-1,3,4-trihydroxyoctadecane (A) and γ -stearolactone (B). It is the first report that γ -stearolactone (B) is isolated from marine fungus as natural product.

Keywords: marine fungus; metabolites; N-(2-hydroxytetracosyl)-2-amino-1,3,4-trihydroxy –octadecane; γ -stearolactone

Mangrove forest coast is a kind of biological coasts. Mangrove is generally known as a kind of arbor trees and shrubs living in the tidal zones. Mangroves' species are in great numbers. The diversities of species gradually change simple because of the differences of latitudes and mangroves also gradually change into low and slight shrubs from tall and big arbor trees. The parasitic fungi are in great numbers because of abundant nutrition in the mangrove forest. It was reported that most described marine fungi could be found from mangroves.

The fungal strain No.2492 was isolated from a sample collected from a mangrove plant *Phragmites austrli* in Hong Kong, and the species was identified as *Stysanus* like sp. Wang et al. [1] had obtained several biogenic amines, such as hypoxylins A and B, from the fermentation liquids of this strain. The chemical constituents of the mycelium of this strain were studied in this paper, and two metabolites were obtained and determined by spectral data as N-(2-hydroxytetracosyl)-2-amino-1,3,4-trihydroxyoctadecane (A) and γ -stearolactone (B), respectively.

Received on March 3, 2006

1 Experimental section

1.1 Instruments and reagents

The following instruments were used: an Inova-500 NMR spectrometer, a VG ZAB-HS mass spectrometer, a Bruker Vector 22 FT-IR spectrophotometer, and a Beijing X4 melting determined instrument.

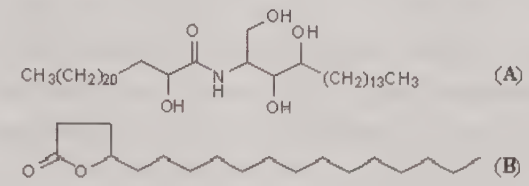

Fig. 1 Structures of compounds A and B

The following reagents were used: glucose(CR), peptone(BR), yeast extracts(BR), crude sea salts(used for culturing microbial), and the others were purchased as AR.

1.2 Fungal strain

A strain of fungus *Stysanus* like sp. (#2492) was isolated from a sample of the mangrove plant *Phragmites austrli* in Hong Kong, and stored in Zhongshan University and the City University of Hong Kong.

1.3 Culture conditions

Starter cultures were maintained on cornmeal seawater agar. Plus of agar supporting mycelial growth were cut and transferred aseptically to a 500 mL Erlenmeyer flask containing 200 mL of liquid medium (glucose 5.0 g/L, peptone 1.0 g/L, yeast extracts 0.5 g/L, beef extracts 0.5 g/L, natural sea water 50 mL/L). The flask was incubated at 30 ℃ on a rotary shaker for 5-7 days. The mycelium was aseptically transferred to a 500 mL Erlenmeyer flasks containing 200 mL culture liquid. The flasks were incubated at 30 ℃ for 45 days.

1.4 Extraction and isolation

The cultures (120 L) were filtered through cheesecloth. The wet mycelium was extracted three times with 5 L cold ethanol, and then extracted three times with 5 L hot ethanol. The combined ethanol was condensed and extracted six times by shaking with an equal volume of ethyl acetate. The combined extracts (about 10 g) were chromatographed on silical gel using a gradient elution from petroleum to ethyl acetate, to obtain A (30 mg) and B (1.5 g).

1.5 Experimental data for compounds

Compound A: white pellets, mp 143 – 144 ℃, FABMS (*m/e*): 685 $[M + 2H]^+$, 427, 385, 368, 317, 235; IR (KBr) ν: 3422, 3245, 2920, 2849, 1620, 1551, 1468, 1073, 722 cm^{-1}; ^1H NMR (500MHz, $CDCl_3$) δ: 7.17 (d, 7.0 Hz, 1H), 4.14 (m, 2H), 3.95 (m, 1H), 3.80 (m, 1H), 3.63 (m, 2H), 1.83 - 1.14 (m, 68H), 0.88 (t, 6.75 Hz, 6H); ^{13}C NMR (500MHz, DMSO-d_6) δ: 173.1 (s), 74.4 (d), 70.9 (d, 2CH), 60.3 (t), 51.2 (d), 34.1 - 21.7 (t, 34CH_2), 13.5 (q, 2 CH_3).

Compound B: colorless crystal, mp 67 - 69 ℃, FABMS (*m/e*): 283 $[M+H]^+$, 265, 205, 124, 97; IR (KBr) ν: 2918, 2850, 1703, 1468, 1433, 1298, 1222, 943, 724, 687, 548 cm^{-1}; ^1H NMR (500MHz, $CDCl_3$) δ: 3.65 (m, 1H), 2.27 (t, 7.5 Hz, 2H), 1.57 (dt, 18.5, 7.0, 7.5 Hz, 2H), 1.25 - 1.15 (m, 26H), 0.82 (t, 7.0 Hz, 3H); ^{13}C NMR (500MHz, $CDCl_3$) δ: 179.0 (s), 72.1 (d), 37.5 (t), 37.4 (t), 33.9 (t), 31.9 (t), 29.7 (t), 29.6 (t, 2CH_2), 29.3 (t), 29.2 (t), 29.1 (t), 29.0 (t), 25.6 (t), 25.5 (t), 24.6 (t), 22.6 (t), 14.1 (q).

2 Results and discussion

Compound A has the molecular formula of $C_{42}H_{85}NO_5$ determined by FABMS (*m/e*) 685 $[M+2H]^+$, ^1H NMR and ^{13}C NMR spectra. The molecular formula suggested the presence of one unsaturated degree.

The IR absorptions of compound A at ν 3422 and 3245 cm^{-1} showed the presence of NH and OH functionalities, and especially the strong absorption at 1620 cm^{-1} suggested the presence of the carbonyl functionality of amide. The presence of amide functionality was confirmed by the typical signal at δ_H 7.17 (d, 7.0 Hz, 1H) in ^1H NMR spectra for the compound A. The signals at δ_H 4.14 (m,2H), 3.95 (m, 1H), 3.80 (m, 1H) and 3.63 (m, 2H) are resonances typical of the protons of methene and methenyl bound to oxygen or nitrogen atoms. The signals at δ_C 74.4 (d), 70.9 (d, 2CH) and 60.3 (t) in ^{13}C NMR and DEPT spectra suggested the presence of three methenyl and one methene bound to oxygen. The signal at δ_C 51.2 (d) is the resonance typical of methenyl bound to nitrogen. There were no other resonance signals except the signal of amide functionality in the ^{13}C NMR spectra for the compound A. It suggested that the compound A is a saturated compound. In addition, the duplicate signals of two methyl at δ_H 0.88 (t, 6.75 Hz, 6H) and δ_C 13.5 (q, 2 CH_3) indicated the presence of two long aliphatic chains in the compound A. According to the above information, the compound A was identified as a saturated four hydroxylceramide.

The binding pattern of compound A was elucidated in Figure 2 by the ion peaks in FABMS. Finally, the structure of compound A was established as *N*-(2-hydroxytetracosyl)-2-amino-1,3,4-trihydroxyoctadecane (see in Figure 1 (A)) by comparison with references[2,3].

Ceramides are noticeable for the function of inhibitory activity against protein kinase C, and are the base backbones forming glycoshpinglipids. The total synthesis of these compounds was studied extensively. But the steps are usually long for the duplicate structures, thus resulting in the low yielding. Especially the reagents are expensive for the specialities [4]. Thus, it is of momentous significance to find that marine fungi could produce abundant sphingolipids.

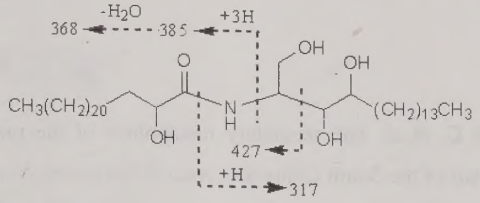

Fig. 2 Main break mode of FABMS of compound A

Compound B has the molecular formula of $C_{18}H_{22}O_2$ determined by the FABMS (*m/e*) 283 $[M+H]^+$ combined with NMR spectra. The molecular formula suggested the presence of two unsaturated degrees. The IR absorption of compound B at 1 703 cm^{-1} showed the presence of carbonyl functionality, and was confirmed by the signal at δ_C 179.0 (s). Thus, one unsaturated degree was explained. There were no signals of unsaturated proton and unsaturated carbon in ^1H NMR and ^{13}C NMR spectra, thus another unsaturated degree was explained as the presence of one ring.

The signals in NMR spectra of compound B suggested the presence of one methenyl bound to oxygen (δ_C 72.1 (d) and δ_H 3.65 (m, 1H)) , two methenes deviation to the high magnetic field (δ_C 37.5 (t) and 37.4 (t)) and the other 14 methenes at the low magnetic field. According to the above information, the compound B was identified as γ -stearolactone. In 1986, Phelan et al [5] detected the presence of γ -stearolactone in the pheromone of male wing *Ephestia elutella* by GC-MS, and found that it could elicit a female response.

It is the first report that γ -stearolactone (B) is isolated from marine fungus as natural product. In the primary bioassay, the compound B did not exhibit inhibitory activity to hTOP isomerase type Ⅰ (hTOP Ⅰ) with the value of IC_{50}>100 μ g/mL, and also had no inhibitory activity against Bel-7402 and NCIH-460 tumor cell lines.

Butenolides are a kind of pheromones, and could elicit and mediate the secondary metabolites production. Signal-transduction mediated by butenolide derivatives have been described as a key factor for the control of the secondary metabolism and other biochemical processes of several microorganisms. Recently, it has been demonstrated that butenolides derivatives are the key signaling factors for the control of bacterial aggregation. Therefore, if the production of these butenolides derivatives could be mediated artificially, then it could enhance the yielding of some economically important natural products and control the bacterial aggregation.

Acknowledgements

This paper was supported by the National "863" Project of China (No. 2001AA624010), the project of GDNSF of China (No. 04300674) and the project of GDSTW of China (No. 2004B30101017).

References

[1] Wang J, She Z G, Jiang G C, et al. The secondary metabolites of the marine fungus No. 2492 from the mangrove *Phragmites australi* of the South China Sea. *Acta Scientiarum. Naturalium Universitatis Sunyatseni*, 2005, 44(2): 132-134.

[2] Huang Q, Tezuka Y, Hatanaka Y, et al. Studies on metabolites of mycoparasitic fungi. Ⅲ. New sesquiterpene alcohol from *Trichoderma koningii*. *Chem. Pharm. Bull.*, 1995, 43(6): 1 035-1 038.

[3] Gao J M, Dong Z J, Yang X, et al. Chemical constituents of *Lepista nuda*. *Chin. Trad. & Herb. Drugs.*, 2002, 35(50): 398-401.

[4] Zhu F, Wu X Y, Lin Y C. Advances in the synthesis of glycosphingolipids. *Chin. J. Org. Chem.*, 2002, 22(11): 817-826.

[5] Phelan P L, Silk P J, Northcott C J, et al. Chemical identification and behavioral characterization of male wing pheromone of *Ephestia elutella* (Pyralidae). *J. Chem. Ecol.*, 1986, 12(1): 135-146.

[6] Zhu F. Charpter 6 Metabolites of marine actinomycetes. In Lin Y C ed., *Marine microorganism and their metabolites*, Beijing: Chemical Industry press, 2003, p169-223.

南海红树内生海洋真菌#2492 代谢产物的研究

朱峰[1,2], 林永成[2], 王军[3], 周世宁[3], Vrijmoed L L P[4]

(1. 佛山科学技术学院化学与化工系，广东 佛山 528000；2. 中山大学化学与化学工程学院，广东 广州 510275；
3. 中山大学药学院，广东 广州 510080；4. 香港城市大学生物学与化学系，中国 香港)

摘 要：研究了分离自中国南海的红树内生海洋真菌 *Stysanus like* sp.（#2492）菌丝体的代谢产物，从该菌菌丝体分离得到 2 个化合物，经现代波谱技术分别鉴定为 N-(2-羟基二十四碳酰基)-1, 3, 4-三羟基-2-氨基十八烷（A）和 γ-硬脂酸内酯（B）。其中 γ-硬脂酸内酯（B）是首次以天然产物的形式从海洋真菌中分离得到。

关键词：海洋真菌；代谢产物；N-(2-羟基二十四碳酰基)-1, 3, 4-三羟基-2-氨基十八烷；γ-硬脂酸内酯

海 洋 通 报（英文版）

HAIYANG TONGBAO

2006 年 10 月　第 8 卷　第 2 期

目次

胶南近岸海域海流实测资料分析及数值模拟计算 …… 刘伟峰 等 (11)

赤道西太平洋 1° 45′ S,156° E 海区的半日内潮波特性 …… 鲍献文 等 (20)

基于模糊影响图的海洋结构风险分析方法研究 …… 康海贵 等 (30)

南沙群岛珊瑚砂物理力学性质研究 …… 于红兵 等 (39)

冲绳海槽天然气水合物稳定带特征和资源量评价 …… 唐　勇 等 (48)

营养盐硅和水温影响浮游植物的机制 …… 杨东方 等 (59)

利用水文、气象要素因子的变化趋势预测南海区赤潮的发生 …… 张俊峰 等 (74)

几个典型台风路径的同化试验 …… 蔡其发 等 (82)

2004 年北太平洋柔鱼钓产量分析及作业渔场与表温的关系 …… 陈新军 等 (91)

南海红树内生海洋真菌#2492 代谢产物的研究 …… 朱　峰 等 (96)

Marine Science Bulletin

Marine Science Bulletin publishes papers on marine science and technology including physical oceanography, chemical oceanography, marine biology, marine geology, environmental oceanography, estuarine & coastal sciences, marine technology, digital ocean, coastal zone management, ocean engineering, marine economics, etc., and aims to promote international academic exchange.

Editor-in-Chief: LIN Shaohua (林绍花)

Associate Editor-in-Chief: HE Guangshun (何广顺) YANG Ying (杨 鹰)

Executive Editor: LIN Baofa (林宝法) HE Xuewu (何学武) ZHANG Deshan (张德山)
ZHANG Xiaoxian (张潇娴) WANG Zhankun (王占坤)
CHENG Xiuchun (程秀春)

Marine Science Bulletin (Vol. 8 No. 2 Oct. 2006)

Responsible Institution:
State Oceanic Administration of China
Edited and Published Semi-annually by:
National Marine Data and Information Service
Address: 93 Liuwei Road, Hedong District, Tianjin 300171, China
E-mail: msb@mail.nmdis.gov.cn

ISSN1000-9620
CN12-1271/N